Thesis

submitted to

UNIVERSITY PIERRE ET MARIE CURIE

by

Juan Camilo ACOSTA MEJÍA

to obtain the degree of:

Doctor of Philosophy of the UNIVERSITY PIERRE ET MARIE CURIE

Specialization: Robotics

Atomic Force Microscopy Based Micro/Nanomanipulation

Defense expected the 16 December 2011

JURY

M.	S. FATIKOW	Professor at University of Oldenburg	Reviewer
M.	M. GAUTHIER	Researcher (HDR) FEMTO-ST	Reviewer
M.	L. CHASSAGNE	Professor at Université de Versailles	Examinator
M.	R. MARCHIANO	Professor at University Pierre et Marie Curie	Examinator
M.	J. POLESEL-MARIS	Researcher at Commissariat à l'Energie Atomique	Examinator
M.	S. REGNIER	PhD advisor Professor at University Pierre et Marie Curie	Examinator

Contents

List of Figures

Notations

This section gathers the main notations used in this manuscript. Unless specified, they are valid for the entire manuscript.

f_0	Resonant frequency of the sensor
Δf	Frequency shift of the sensor
ω_{phase}	Resonant frequency of the sensor when the two prongs are oscillating in phase
$\omega_{anti-phase}$	Resonant frequency of the sensor when the two prongs are oscillating in anti-phase. It is f_0
k	Stiffness of a single prong of the tuning fork
Δk	Stiffness shift. Equivalent to measured stiffness by the sensor
k_c	Coupling stiffness between the two prong of the tuning fork
$k_{TIPlong}$	Longitudinal stiffness of the tip attached to the quartz sensor
k_{TIPlat}	Lateral stiffness of the tip attached to the quartz sensor

k_{SPL}	Sample stiffness in perpendicular direction to the substrate
k_{CSTR}	Constraint stiffness of the sample in parallel direction to the substrate
k_{TFeff}	Tuning fork effective stiffness
$k_{TFcontact}$	Vertical stiffness of the tuning fork and tip at the contact point.
k_{HNB}	Helical nanobel stiffness
m	Tuning fork prong mass
m_{tip}	Total mass added to one prong of the tuning fork by tip and glue.
m_{SPL}	Sample mass
m_{TFeff}	Tuning fork effective mass
α	Angle between the tip and the tuning fork prong
τ	Settling time of the sensor
t_m	Manipulation time by an AFM tip
t_s	AFM image acquisition time

General introduction

At nanoscale, a scientific fundamental problem is the manipulation of nanoobjects in ambient conditions. This difficulty is a mayor barrier for applications like nanotransistors, nanosystems or future NEMS (Nano Electro-Mechanical Systems). These emerging devices are in consequence, slowed in their experimental development. One of the devices that attempt to address those issues is the AFM (Atomic Force Microscope). It is the most commonly used device for nanomanipulation in the air as of today and is a device with positioning devices and sensor with a resolution suitable for the nanoscale environment. This approach is slow for the robotic manipulation task due to the imaging and force sensing speed. The lack of dexterity combined with the high speed dynamics of the nanoscale make the robotics with an AFM in the air, a mayor challenge.

This thesis focus on the original use of robotics techniques for manipulation in the air with an AFM. Force sensing is a key factor for a repeatable positioning of the manipulation system. Our work is based on multifeedback cooperation for improving the manipulation capabilities, like passing from 2D to 3D micro/nanomanipulation. Additionally, this thesis aims to define original methods for compensation of undesired effects like noise, and strategies for manipulation at that scale. The passage from static force sensing to dynamic force sensing based manipulation is in the scope for increasing the throughput of the system, and so, the potential application on automation and nanoassembly.

Different steps are done in this work in order to improve atomic force microscopy based nanomanipulation. In chapter 1, a deep review of mayor works in AFM manipulation has been done. The chapter start by explaining the classic operation of an AFM. After, the different modes of imaging based on AFM are explained and a comparison with other imaging methods in nanoscale is made in order to know how it stands next to the others. Then, the micro/nanomanipulation applications and challenges in the air are presented followed by the efficiency of such manipulation process. We will see that one of the main challenges in AFM based manipulation is pick-and-place. After, parallel imaging and manipulation with a two tip AFM is presented. Being limited by the speed of imaging, high speed AFM works are shown in order to find possible solutions to the last problem. In the second section of the chapter, force sensing with an AFM is presented. It is the most important feature of the AFM for manipulation. First the static force sensors are presented followed by the dynamic force sensors. Dynamic force sensors appear as a possible solution toward fast non-invasive imaging and force sensing with embedded sensor. Still, this impose a new challenge, the calibration of the sensor for quantitative force measurement. A walkthrough the different models of the dynamic sensor is shown after. The third section of the chapter represents the works done and the challenges for the characterization of nanostructures. a properly calibrated dynamic force sensor appears as a possible solution for mechanical characterization of nanostructures. In the final section of the chapter, the objectives and proposed solution is presented.

Chapter 2 aims to make a first step towards 3D micro/nanomanipulation. For that, a two tip AFM has been developed. A microgripper is formed with the protrudent tips of two AFM cantilevers. The key of this proposed solution, is a method for obtaining real time force feedback during the entire process. Two application of the system are presented in this chapter. In the first part, two layer 3D micropyramids are build with microspheres of diameters of 3 μm $\sim$ 4 μm. A protocol has been developed for the cooperative manipulation with two tips, using visual feedback from optical microscope for coarse position and AFM scanning for grasping point location. In the second part, nanocrosses are build with SiNW (Silicon NanoWires) with diameters in average of 150 nm. This process relied only on the visual feedback for AFM imaging. The speed of the last one, in addition with the dexterity of the arm are the mayor limitants of the system,

High speed force sensing techniques are studied as well as dynamic force sensors with embedded measuring in chapter 3. The study focuses on the classical dynamic force sensor, the quartz tuning fork. Mechanical characterization of ultraflexible nanostructures are picked as an application example of these force feedback techniques. In the first part of the chapter, the modeling of the sensor when tip attached

is done, for quantitative force measurement, followed by the validation of the dynamic force sensing capabilities. For that, we aim to develop a 3D nanomechanical property characterization system with large range and high resolution force sensing. The 3D characterization based on the developed sensor is achieved with an SEM for an accurate visual detection and a nanomanipulation system with 3 degrees of freedom and nanometer positioning resolution. The large range and dynamic force sensing of the proposed system is proved by a full range tensile elongation study of HNB. In this case, the tuning fork is fixed. Finally, the dexterity of the sensor is proven by the surface characterization of membranes with a moving sensor.

In the last chapter of this dissertation, an integration of the dynamic force sensor with the two tip AFM system is donde, resulting in a new robotic system for faster parallel imaging and manipulation. In the first part of this chapter, a complete analysis of the system depicted in chapter 2 in terms of speed is made. After that, the different kinematical configurations of the system are compared followed by the proposed force sensor and, software and hardware modifications. A new quartz sensor with higher resonant frequencies than the tuning fork is proposed to increase the imaging and force sensing speed. The sets of experiments to validate the system are divided in three parts. First, imaging test are done with a known hard surface to validate the calibration and speed of the complete system. The second set of test consist in the image acquisition of a hard surface with loose objects like gold nanospheres with the objective of showing the non-invasive capabilities of the system. Finally, a manipulation task with two cooperative arms of the new system is done to show the potential application of the system with nanomanipulation.

This work is a first step toward a fully automated system for real time parallel imaging and manipulation. Force feedback was the key of increasing the manipulation capabilities of the AFM, passing from 2D to 3D. Additionally, dynamic force sensing methods appears as a promising technique for understanding the mechanical properties on the nano structures. Furthermore, their integration in a two tip AFM setup resulted in a system in some cases, fifty times faster. The perspectives presented in this work show the importance of the role of high speed dynamic force sensing for automation and dynamic characterization of nanostructures.

Chapter 1

Force microscopy based nanorobotic systems

Contents

Due to the developments in nanotechnology and biotechnology in the last two decades, handling nanometer scale entities has become a critical issue. Since the human sensing, precision and size are not sufficient to interact with such nanoscale entities directly, nanorobotics has emerged as a new robotics field to extend our manipulation capabilities to nanometer scale [Sit07] [Req03]. This, however, is not an easy task. Even if classical robotics has reach a maturity as it is fifty years older,

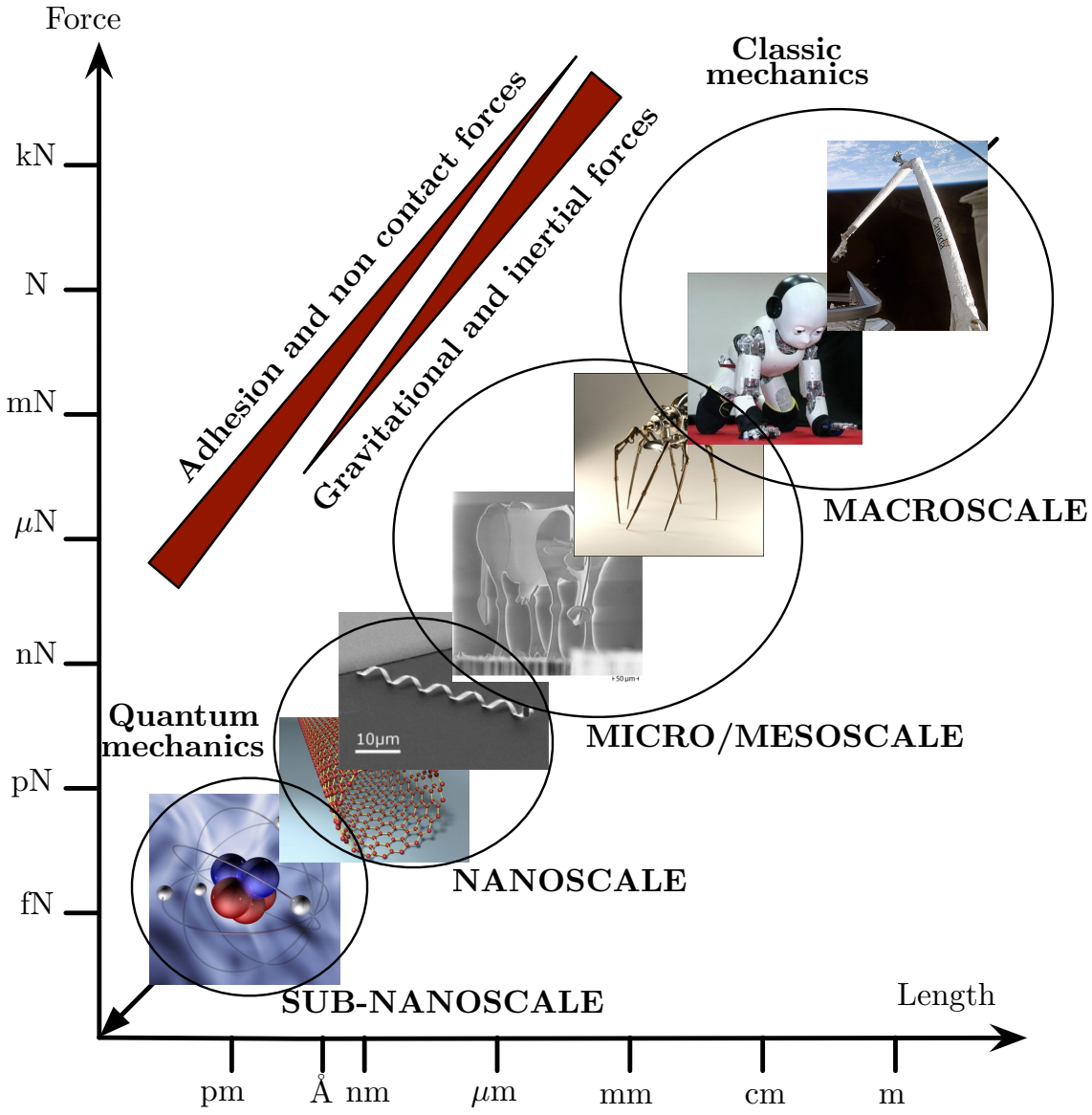

Figure 1.1 - *Multiscale mechanics multiparadigm*

there is no straightforward transition to nanorobotics because the physics change thus classical models are no longer valid (Fig. 1.1). At macroscale, the predominant forces are derived from the mass of the robot, being mainly the gravitational and inertial. As the scale is reduced these forces are less dominant and adhesion and non contact forces becomes more important. These forces are for example Van der Waals and electrostatic. Additionally, at micro-nanoscale, meniscus formed from humidity as well as water layers become big compared to the object to manipulate. A analogy with the macroworld would be "manipulating objects at micro/nanoscale is like manipulating objects at macroscale in an environment full of heavy mud". Furthermore, at the nanoscale, the objects can change position and even size/shape due to temperature changes. The thermal drift is considered noise and to date has not been well characterized. Still a work for statistical compensation has been done in Oldenburg [KOSF09]. Another option to avoid influence from the drift, is a fast manipulation. This is however, a challenge in the air. Furthermore, nanorobotics means literally the study of robots that are nanoscale in typical size, i.e. nanorobots, which have yet to be realized. Generally, nanorobots are macroscale robots capable of manipulation of nanoscale objects. In consequence, the dynamics of the nanorobots are very slow compared to the dynamics of the nanoworld. Speeding the manipulation process done by the nanorobots remains one of the biggest challenges.

A typical manipulation task at the macroscale requires generally a manipulation tool to interact with the object and a feedback to monitor the manipulation process. The nanomanipulation task is conceptually, the same:

- A positioning device with nanometer/subnanometer resolution is needed to manipulate the object;
- A very sharp tip compared to the size of the object (typically of less than 100nm of diameter) is needed to overcome forces derived from surface effects;
- An imaging tool with nanoscale resolution is needed to obtain the position of the objects to manipulate, and the nanoworld surrounding them;
- A force sensor is essential for quantifying the interaction between the tip and the object. The tip is generally mounted on the force sensor;
- Ideally, the manipulation process should be as fast as possible. First to avoid disturbances from thermal drift and second, for automation to increase the

throughput of the system.

The only nanomanipulator that has all the properties depicted before except the last is the AFM (Atomic Force Microscope) still, 3D nanomanipulation with force feedback is still a challenge in the air. This work is focused on modifications of the AFM in order to improve the manipulation process with force feedback. This chapter is focused on the state of art on manipulation with an atomic force microscope.

In the first section of this chapter, nanorobotics based on the AFM is presented. At the beginning, an overview of the AFM is made, followed by the operation mode of a classical AFM for imaging. Then, the micro/nanomanipulation applications and challenges in the air are presented followed by the efficiency of such manipulation process. After, parallel imaging and manipulation with a two tip AFM is presented, At the end of the section high speed AFM works are shown.

In the second section, force sensing with an AFM is presented. In this section, first the static force sensors are presented followed by the dynamic force sensors. Then, one of the biggest challenges of a dynamic force sensor is presented, the calibration.

The third section of the chapter represents the works done and the challenges for the characterization of nanostructures. The last mainly limited by the use of adequate force sensor. In that last section, the dynamic force sensing for mechanical characterization appears as a possible solution.

The last section of the chapter presents the objectives and proposed solution for this dissertation.

1.1 Nanorobotics with atomic force microscopy

1.1.1 Overview

The AFM was initially created for imaging purposes as the name implies, by G. Binnig, F. Quate from Stanford University and Ch. Gerber from IBM [BQG86]. In

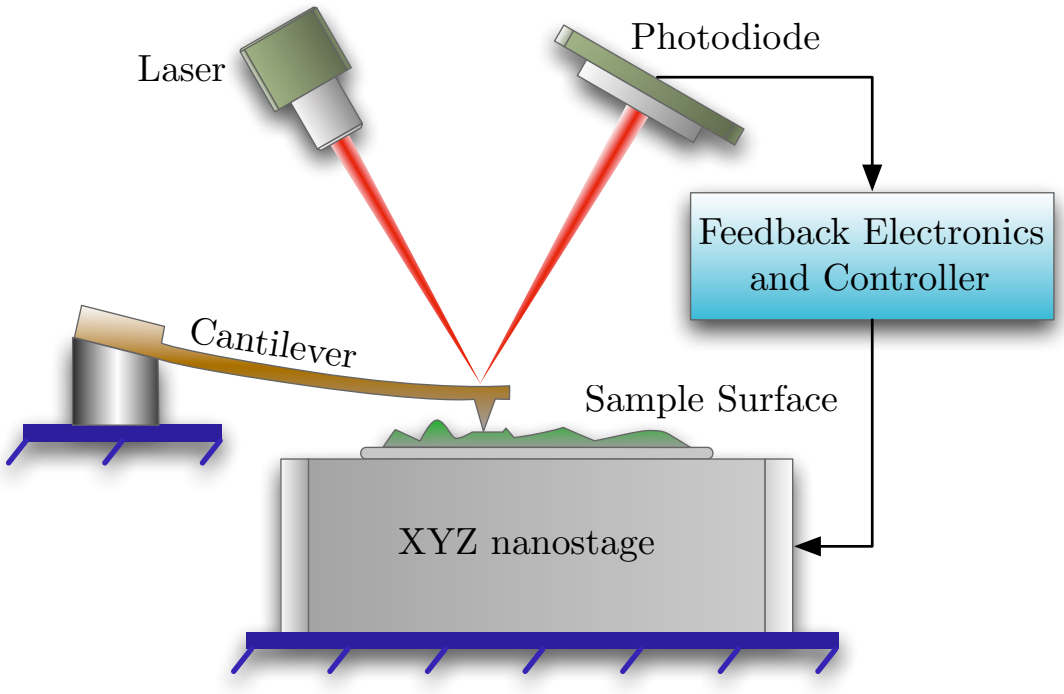

Figure 1.2 - *Atomic force microscope base diagram. The laser beam is reflected on the cantilever surface to the photodiode. This way, the deflection of the cantilever can be obtained. The substrate is on top of a piezostage for scanning the surface.*

its more basic form, it is composed of a single cantilever with a tip and a device for sensing the deflection of the cantilever. The mechanical model of the cantilever is known, in consequence, the force can be obtained. Initially a Scanning tunnelling microscope was used for detecting the deformation of the cantilever, it was later replaced by a laser and photodiode (The base diagram of an AFM can be seen in Fig. 1.2). Usually, the cantilever tip is fixed and the substrate is mounted on top of an X-Y-Z piezostage with subnanometer resolution. With this stage, an area of the substrate is scanned for imaging purposes.

1.1.2 Imaging

The classic mode of operation for AFM imaging is the contact mode (Fig. 1.3.(a)), where the cantilever tip remains in contact with the sample. For this mode, the deflection of the cantilever obtained with the photodiode can be fixed by controlling the position in Z-axis of the piezostage, and so, the force between the tip and substrate can be maintained constant during the scan. The image can be constructed

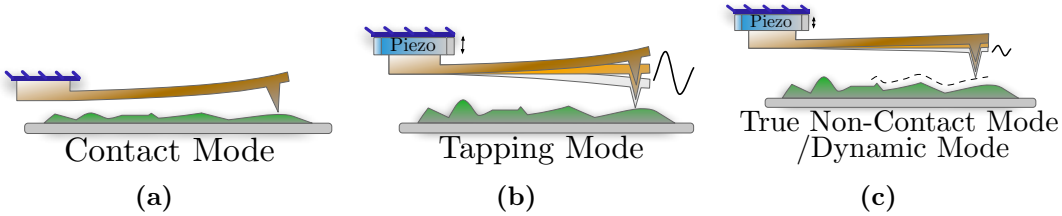

Figure 1.3 - *Comparison of the three different imaging modes in atomic force microscopy. (a) Contact mode, in this mode, the tip is always in contact with the substrate. (b) Tapping mode, where the tip has an intermittent contact with the substrate and (c) true non-contact mode or dynamic mode, where the tip never touches the substrate, oscillates at smaller amplitudes than tapping mode, and is always in the range of non-contact forces*

from the position of the piezostage for the surface scan. In an opposite way, the Z-axis position of the stage can be fixed, and the deflection of the cantilever readout with the photodiode are used for the generation of the image. This technique avoids the control in Z-axis but result in a scan with non constant force and limited range in Z-axis increasing the probability of the tip wear and the surface modification. Additionally the cantilever can be mounted on a piezo actuator for dynamic measures. The piezo is used to make the cantilever oscillate at its first mode resonant frequency. While the cantilever its oscillating, two different techniques can be used, "tapping mode" and "True non-contact mode". In taping mode, the cantilever is oscillating near its resonant frequency and its tapping the surface (Fig. 1.3.(b)). Its is often referred as non-contact mode because most of the time the tip is in non-contact. The change in the amplitude of oscillation due to the contact with the surface will be used for making the AFM image. This method is very aggressive with the tip of the cantilever. The tip will wear very fast due to the intermittent impacts with the surface. The second mode used while the sensor is oscillating, is called "true non-contact mode". In this case, non-contact forces are used for imaging (Fig. 1.3.(c)). For this, the amplitude of oscillation of the sensor should be under the range of non-contact forces (a few nanometers) to avoid impact. For the non-contact mode, two techniques are used, amplitude modulation and frequency modulation. For the first, the amplitude of oscillation is monitored from point to point and is a technique using the force between the tip and the substrate as feedback for the oscillation. The second technique is frequency modulation, where phase and amplitude are controlled to obtain the frequency shift. With the shift, AFM images are made. It is a technique where the gradient of the force is used. Further details on how to obtain the force with these techniques can be seen in section 1.2 of chapter 1. In the following, a comparison between AFM imaging and other techniques used for visual feedback for micro and nanomanipulation is shown.

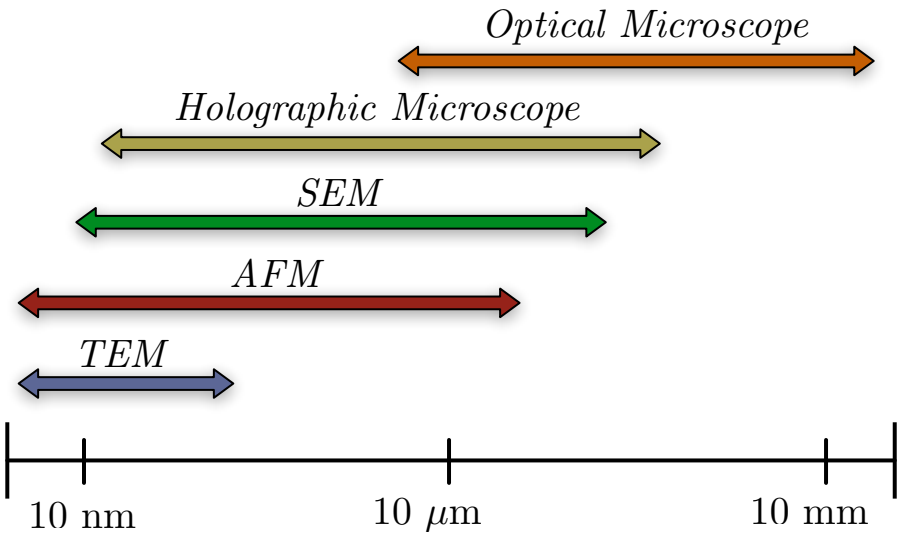

Figure 1.4 - *Comparison of the imaging range of often-used imaging instruments.*

The visual feedback for the nanomanipulation task can be obtained in very different ways, however, four types of microscopies are generally considered, including AFM, transmission electron microscope (TEM), Scanning Electron Microscope (SEM) and recently the digital holographic microscope (DHM). Fig. 1.4 shows a comparison between the imaging range capabilities of these systems. The SEM obtains 2D images by scanning the sample with a high-energy beam of electrons in a raster scan pattern. It is fast compared to classical AFM, the main drawbacks are that it works only in vacuum conditions restricting the variety of samples and that it cannot estimate the height of the samples due to the 2D images. The TEM is the oldest of all, introduced in 1931 by Max Knoll and Ernst Ruska, it is an imaging technique whereby a beam o electrons is transmitted through an ultra thin specimen, interacting with the specimen as it passes through. In consequence it requires very thin sample. Unlike SEM (Fig. 1.5.(b)) and TEM (Fig. 1.5.(c)), the AFM can obtain 3D images (Fig. 1.5.(a)), a surface height profile is obtained by scanning it mechanically with an XYZ piezoscanner. In general, it is the most flexible tool of all because it can work in the three different environments, vacuum air and liquid, and it does not requires special samples. Additionally, it has the best horizontal and vertical resolution (Table 1.1). The main drawback of the AFM is the image acquisition speed, normally higher than 4 minutes, however, this can be compensated with a faster sample preparation. Recently, a new type of microscope has appeared, the digital holographic microscope (DHM) (Fig. 1.5.(d)). It is the fastest, still, it lacks the horizontal resolution of the others limiting the potential applications for

micromanipulation tasks.

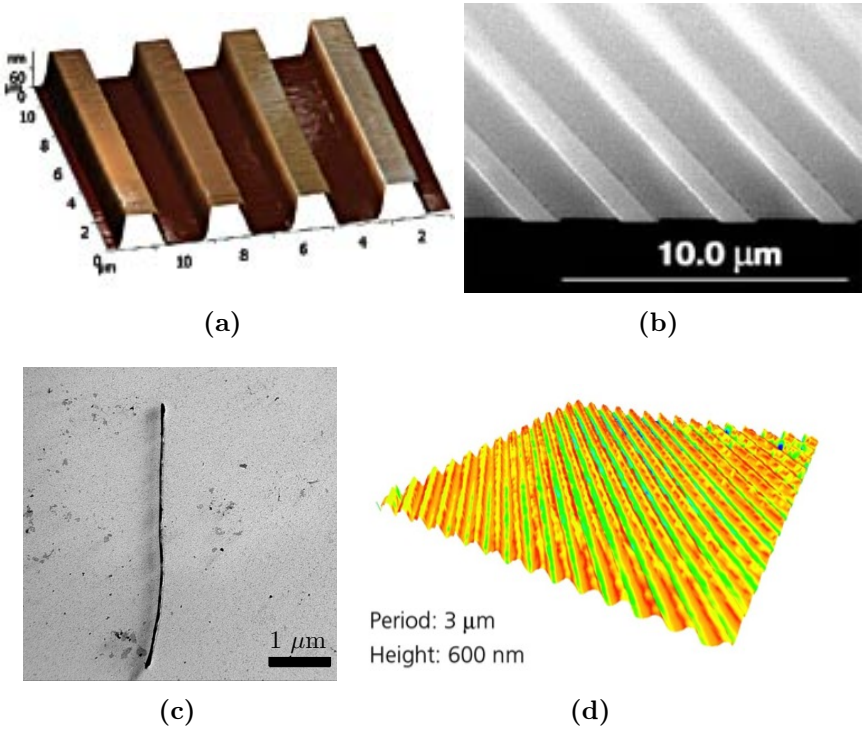

(a) (b)

(c) (d)

Figure 1.5 - *Nanoworld imaging. (a) AFM 3D image of a calibration grating specimen TGZ100 from µmash, (b) SEM image from same specimen, (c) TEM image of CdTe nanowire from LVEM, USA and (d) DHM 3D image of 600nm gratings from Lyncée tec.*

1.1.3 Nanomanipulation tasks

Two dimensional manipulation with force microscopy became a reality by chance. AFM were initially created for imaging, the modification of the substrate due to the surface tip interaction while imaging showed the potential use as a nanomanipulator. Still, it was an undesired effect, and still is for imaging purposes. They were created to work in air conditions, later, attempts were made to integrate it with an SEM, but do to the space available inside the vacuum chamber and the nature of the canon beam, the AFM were simplified by replacing the optics with piezoresistive cantilevers, decreasing the resolution [MWF10]. The AFM, as of today, is the base device for nanomanipulation with force feedback in the air.

Table 1.1 - *Comparisons between AFM, TEM/SEM and DHM*

Descriptions	AFM	TEM/SEM	DHM
Samples	Any	Conductive	Reflective
Environement	Vacuum/Air/Liquid	Vacuum	Air/Liquid
Horizontal Resolution	0.2 nm	0.2 nm/5 nm	0.3 μm
Vertical Resolution	0.05 nm	n/a	0.1 nm
Field of view	100 μm	100 nm/1 mm	5.5 mm
Time for image	1$\sim$5 min	0.1 s$\sim$1 min	>3.3 μs

As a nanomanipulator, it has been mainly used for pushing, pulling, scratching or cutting, either with the tip of the cantilever or the cantilever itself. These manipulation tasks can be divided in three main blocks:

- Two-dimensional lateral pushing or pulling, including contact and noncontact modes;
- Three-dimensional pick and place nanomanipulation with a single nanotip with the help force field usually;
- Three-dimensional pick-and-place nanomanipulation with a multi-tip nanotweezer.

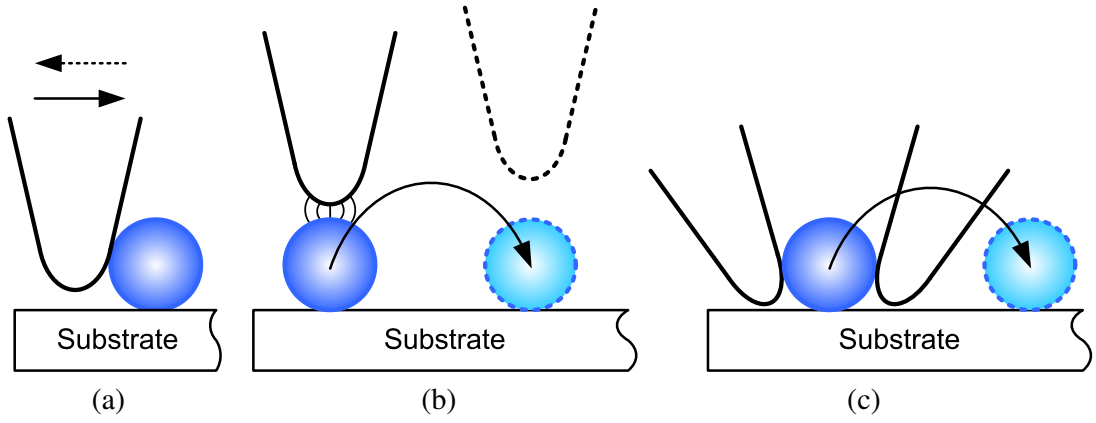

Figure 1.6 - *Fundamental nanomanipulation strategies with the AFM. (a) Lateral contact nanomanipulation with pushing/pulling strategies. (b) Pick-and-place with a single AFM probe. (c) Pick-and- place with a dual-probe nanotweezer.*

AFM pushing or pulling nanoobjects on a surface are typical lateral nanomanipulation methods, as shown in Fig. 1.6(a). A amount of research work have been

carried out with these methods for making two-dimensional patterns ([MRH+98], [SH00], [RLM+00], [AL07], [TBCD07]) (Fig. 1.7), characterizing nanofriction by sliding or rolling nanoparticles, bending nanotubes or nanowires ([Sit04], [PB08], [DMJ+07], [CGR+08]), exploring nanophysical phenomena ([XT03], [GRM+06], [MGR+08], [WMT+06]), and material testing by bending or breaking ([LGMC03], [BRC+07], [WHB05], [NL06]). Recently, pick- and-place nanomanipulation tasks shown in Fig. 1.6(b) have been demonstrated by an coaxial atomic force microscope [BAW10] and electro-enhanced capillary forces [TG10] respectively.

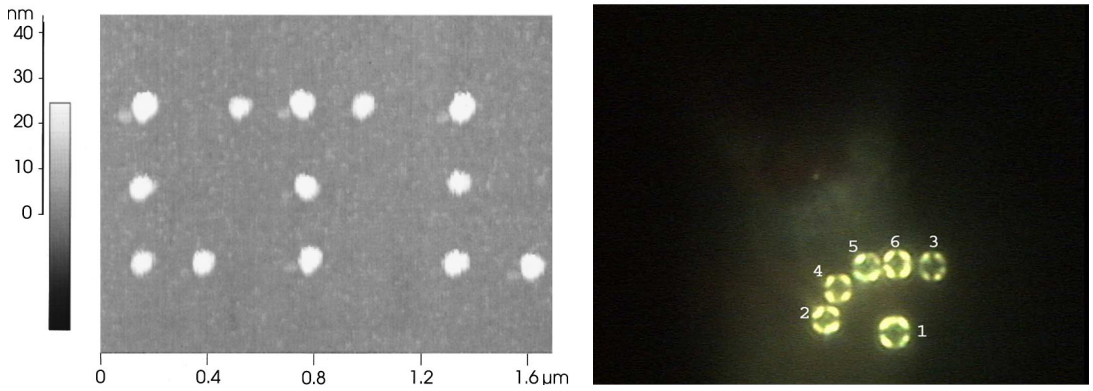

(a) (b)

Figure 1.7 - *Pushing spheres with an AFM. (a) Low temperature laboratory (LTL) written in block letters with 45 nm silver particles on top of silicon dioxide substrate. ([MRH+98]) (b) Arrangement made with 4.5 µm diameter PS particles ([OS07])*

It is well known that the pick-and-place is a significant manipulation technique on 3D microstructure fabrication since it is an indispensable step in the bottom-up building process. However, few literatures reported the mechanical pick-and-place manipulation of microobjects with feature sizes less than 10 μm, especially the manipulation confined in air. The main difficulties in sufficiently completing the pick- and-place micromanipulation at this scale are in fabricating such a sharp end-effectors that has a capability of smoothly releasing microobjects (Fig. 1.6(c)), simultaneously with an enough output of grasping force to overcome strong adhesion forces ([MEID04], [LR06], [Sit07]) as well as capabilities of sensing and control of interactions between the microobject and the tool or the substrate. Furthermore, compared with the larger microobjects, optical vision feedback on several microns suffers more from shorter depth-of-focus and narrower field-of-view using lenses with higher magnifications, although different schemes or algorithms have been introduced on the optical microscope for autofocusing ([XRS07], [LWS07]) and extension of the depth-of-focus [XRSC06]. In contrast with the vision-servoing

based 2D automated micromanipulation [OS07], automated 3D micromanipulation at the scale of several microns is still a great challenge in building 3D microstructures due to the lack of sufficient feedback information that is beyond the capability of the microscopic vision, such as the vertical contact detection along the optical axis or manipulation obstructed by opaque components. Thus, in order to facilitate the 3-D micromanipulation at the scale less than 10 μm, multi-feedback is of vital importance to achieve such an accurate and stable 3D micromanipulation.

Pick-and-place, is also a significant technique for nanomanipulation specially for 3D nanostructure fabrication since it is an indispensable step in the "bottom-up" building process. It is also a promising nanofabrication technique to combine advantages of the "bottom-up" and the "top-down" methods for complex 3D nanostructures building. Nanostructures have been manipulated, assembled and characterized by integrating nanomanipulators or nanogrippers into scanning electron microscopes (SEM) and transmission electron microscopes (TEM) ([FAD03], [DAF02], [DAF04], [MWKB06]). Both the SEM and the TEM provide a vacuum environment where the van der Waals force is the main force to be overcome during the manipulation. 3D manipulation could also be achieved with optical tweezers, because in this case the emergence of the liquid greatly reduces the often strong adhesion forces ([YCS04], [BABO08]). However, pick-and-place manipulation is still a great challenge in air due to the presence of strong adhesion forces [RRG99]. In this case, the main difficulties in completing a sufficient 3D manipulation in air are fabricating such sharp end-effectors with enough grasping forces as well as capabilities of sensing and control of strong interactions between the object and the tool or the substrate.

Compared with the SEMs and the TEMs, the AFM based nanomanipulation in the actual use has much more flexibility in applications to various nanoobjects in different environments-air, liquid and vacuum. However, conventional AFM based nanomanipulation strategies are restricted to push and pull nanoobjects on a single surface ([FTIH$^+$99], [BBK$^+$98], [RLM$^+$00], [SH00], [JYSAK$^+$07]). The pick-and-place manipulation of nanoobjects in air is still unresolved, although vertical pickup of atoms have be fulfilled by a electric field trapping [WSDC91], van der Waals forces [ES90] [Avo95], tunneling current induced heating and inelastic tunneling vibration [Avo95]. Grasping nanoobjects using two-tip carbon nanotube (CNT) tweezers has been demonstrated [KL99], but the alignment of the CNTs remains a challenge and capabilities of the CNT tweezer in overcoming great adhesion forces in air need to be validated. Therefore, a 3D nanomanipulation system is crucial in achieving the pick- and-place operation in the 3D nanostructures building. In the following, an analysis of the efficiency of the manipulation process of current AFM

is made in order to depict the challenges.

1.1.4 Efficiency

Although the AFM has been proved to be a powerful manipulating tool for understanding nanoscale physical and chemical phenomena as well as for performing fabrication of nanostructures or nanodevices, it is well known that AFM-based nanomanipulation is very insufficient and definitely influence its practical applications. Two aspects might contribute to the low efficiency of AFM based nanomanipulation and nanoassembly:

- Despite the AFM has been demonstrated to be a powerful tool in exploring the nanoworld, the approach itself is severely limited in imaging speed. A typical AFM image of a samples with 256 by 256 pixels takes often minutes, to scan. It is clear that mapping large areas of a surface can be particularly laborious. Therefore, low-speed image scanning involved make a AFM-based nanomanipulation task insufficient.

- Unlike nanomanipulation performed in a SEM or a TEM, AFM-based nanomanipulation another inherent limitation of AFM-based nanomanipulation is that the AFM acts as an imaging sensor as well as a manipulating tool simultaneously, and so cannot provide manipulation with real-time visual feedback, but rather an insufficient serial process of scanning-manipulating-scanning. As seen in Fig. 1.8, at least two image scans should be performed respectively for task planning and verification of manipulation results. Moreover, lack of real-time visual feedback makes the "blind" manipulation process very difficult to control and then local image scan are frequently required to relocate nanoobjects when manipulation lost. It is obvious that repeatedly image scans make the manipulation process fairly lengthy.

In order to conquer limitations above-mentioned on visual feedback and facilitate nanomanipulation, haptic devices and virtual reality interfaces have been introduced into AFM-based nanomanipulation systems [SH00], [RLM$^+$00], thereby enabling an operator to directly interact with the real nano-world. The virtual reality generally provide a user with a static nanoenvironment. In this case, the user is still "blind" since the changes in the nanoenvironment is unavailable. Although behaviour of

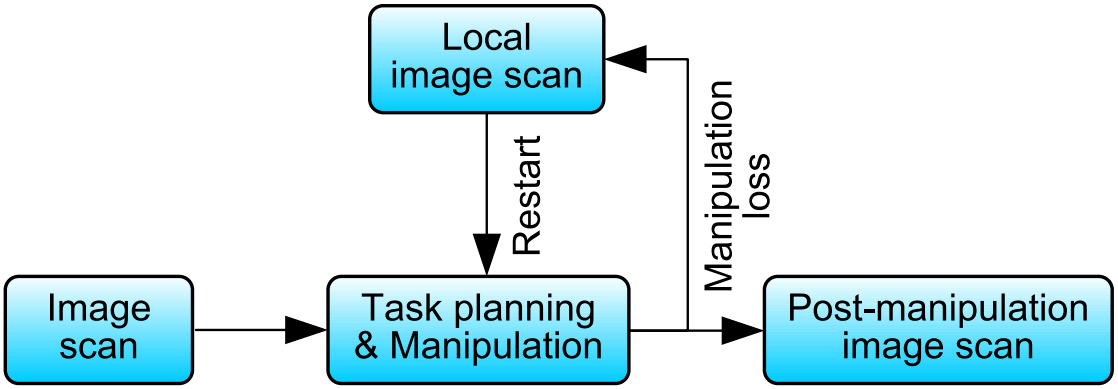

Figure 1.8 - *A serial procedure of conventional AFM based nanomanipulation.*

the AFM tip and nanoobjects being manipulated can be theoretically predicted by interactive models and real-time force feedback from the manipulation, many uncertainties, e.g. thermal drift, scanner hysteresis and creep, sticking phenomena between the tip and nanoobjects as well as some others unpredicted behaviours of nanoobjects, can not be accurately predicted and modelled. Thus, haptic devices and virtual reality interfaces can not provide perfect solutions on lack of visual feedback.

To overcome these issues, independent works have been done. In the following first the works to solve the problem of imaging speed of the AFM are presented followed by a work done in parallel imaging a manipulation to adress the second issue

1.1.5 Parallel imaging and manipulation

A two tip AFM has been developed at ISIR by Hui Xie [XHR09] for parallel imaging and manipulation. The piezoscanner is used for the faster imaging of the substrate and the nanostage is used for the manipulation as seen in Fig. 1.9. With this configuration, the imaging with the tip number I and the piezoscanner will not change the distance between the tip number II and the substrate. Additionally, the manipulation with the nanostage wont affect the distance between the two tips.

A key component of the system, is the special cantilever with a protrudent tip that makes interactions between cantilever I and cantilever II feasible. The protrudent

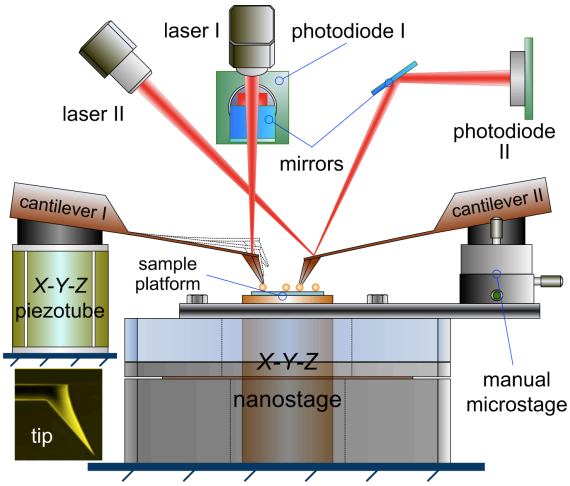

Figure 1.9 - *System diagram of the parallel imaging/manipulation force microscope. [XHR09]*

tip enables image scan on the tip of cantilever II (tip II) using cantilever I. By this means, the relative positions between nano-objects and tip II end can be obtained from the image scan that is indispensable for AFM-based manipulation. The tilted angle of the cantilever tip is approximately 62°-64° on the side view without a mounting angle. In the system, the cantilevers are mounted with an angle of 8°. An excellent image quality can be achieved even though the scan length on tip II is more than 300 nm, which is sufficient for tip positioning with a dynamic image display updated by real-time scanning data.

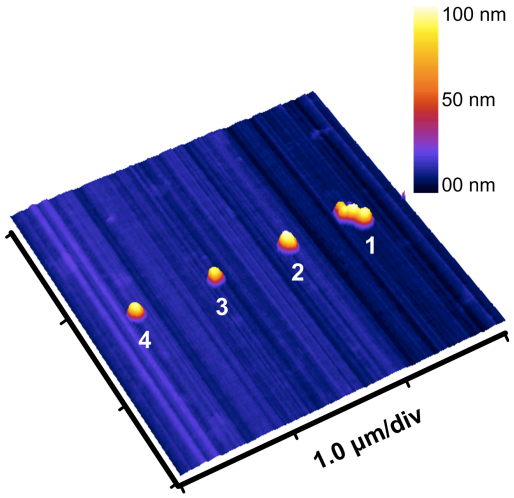

Figure 1.10 - *A parallel imaging/manipulation result with a normal-speed image scan of tip I. [XHR09].*

A parallel image/manipulation task was performed with a normal-speed image scan on the developed system. Manipulation results are shown in Fig. 1.10, in which four Ag nanoparticles with a diameter of 74 nm – 82 nm, emerged on dynamic image I to IV in sequence, were pushed onto the image midline during the image scan. In the experiment, the frame period was about ten minutes. In contrast, the total manipulation time of these four nanoparticles was less than one minute with a pushing velocity of about 300 nm/s.

This work sets a new way of efficient nanomanipulation. The system is however limited by two factors. First, the photodiodes and lasers don't move with the cantilevers limiting the dexterity of the arm. And more important, the process speed was highly limited by the speed of the AFM imaging. A consequent step for improving this system is solving this two issues.

1.1.6 High speed AFM

High-speed AFM might be a promising way to improve the efficiency of the AFM nanomanipulaion. High-speed AFM was originally developed to study and track dynamic behaviour of biology samples, e.g. protein molecules, cirrus. New developments of the high-speed AFM can provide users with a real video rate reaching to tens of frames that is sufficient for visual feedback [AUF08].

The image acquisition time of an AFM, and in fact any SPM, is limited by three factors [HMH05]:

- The measurement bandwidth of the local interaction between the tip and sample and a system capable of processing the data in real time;
- The rate at which the tip can scan the surface of the sample in an x, y plane;
- How quickly the tip can follow the contours of the sample.

Several physic groups have been working to address these issues. At the university of Stanford for example they used Tuning forks [Gie], and high speed tapping mode imaging with active Q control of micro cantilevers [SHA+00], to improve the first factor. Still, these approaches do not solve the four issues and are limited in

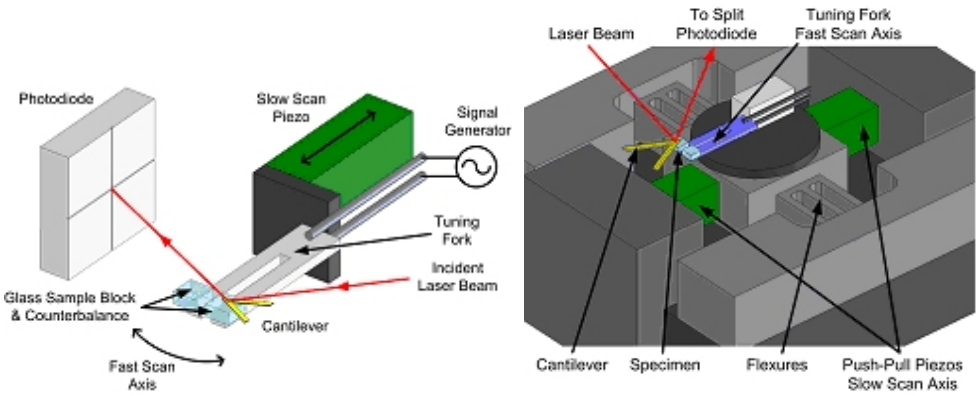

(a) **(b)**

Figure 1.11 - *High speed AFM setups from Bristol university. (a) Schematic of the resonant scanning high-speed AFM [HMH05], (b) Schematic of the ultra-high-speed AFM scan stage [PBU+07].*

resolution, area size or speed. Only one group has really achieved fast AFM, the group of nanophysics and soft matter at the university of Bristol (Fig. 1.11). To address the first issue, they used AFM cantilever with laser/photodiode. For the second, they used a tuning fork as motion generator for the fast scan axis and piezo or push-Pull piezo for the slow Scan axis. To follow the contours of the sample, they used contact mode AFM and avoid this way, control on z-axis. Due to the nature of the sensor, it is the substrate that moves and not the sensor.

Although high-speed AFMs have succeeded in raising the scanning efficiency, the excellent imaging potential of high-speed AFM will be greatly reduced if additionally to imaging, the system will be used for nanomanipulation. The high speed scan has to be the less invasive as possible with the substrate to avoid modification of the objects positions. Still, real non contact mode fast AFM has never been done, and these techniques have never been applied to parallel imaging and manipulation under AFM. Non-invasive fast AFM has not yet been attempted. In order to address those issues, atomic force sensing techniques need to be studied, spatially dynamic methods as they appear as a promising techniques for fast non-invasive imaging.

1.2 Atomic force microscope force sensing

The key of an atomic for microscope based manipulation resides in the ability to provide a force feedback for manipulation. Understanding the different ways of force

sensing is very important. In those techniques resides the potential ability of a 3D manipulation system conception and a fast imaging system.

Current force sensors can be mainly classified by their working mode. It refers to the capacity to work in static mode or dynamic/oscillating mode. In the following, they will be presented based on that classification.

1.2.1 Static force sensing

The most classical of sensors is the atomic force microscope cantilever (Fig. 1.12.(a)). A cantilever with a tip is used to contact the substrate. A laser is pointed to the flat surface of the cantilever and reflected to a photodiode to obtain its deflection. This deflection can be traduced into force with the stiffness of the cantilever:

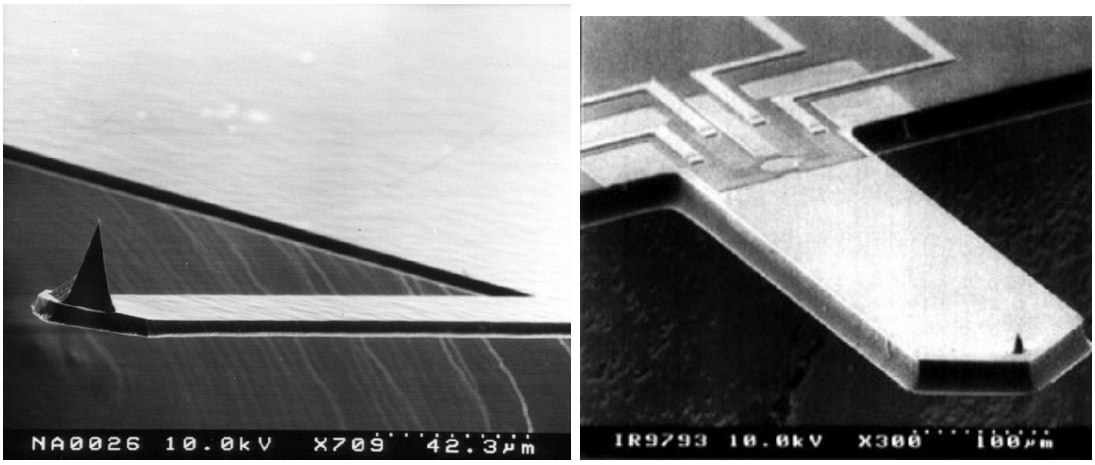

(a) *SEM image of a Typical AFM cantilever*

(b) *SEM image of a piezoresistive cantilever with integrated Wheatstone bridge*

Figure 1.12 - *Atomic force microscope cantilevers.*

$$F_n = k_{Cn} \cdot \delta_z \tag{1.1}$$

where F_n is the estimated normal force, k_{Cn} the normal stiffness of the cantilever and δ_z the deflection in Z-axis of the cantilever. For small displacements, this deflection can be obtained with a linear relationship with the photodiode. This type of force measurement is called static and needs an external sensor, it is depicted in

Fig. 1.2.

The external sensing of the cantilever poses several problems, first, the alignment of the laser and photodiodes, and second, the occupied space. These are big drawbacks for the dexterity of the arm holding the cantilever and the integration of the system inside an SEM chamber. To solve this issues, piezoresistive cantilevers are used(Fig. 1.12.b). They use generally a Wheatstone bridge to measure the change in resistivity in both axis which can be traduced in to force. Still, they lack the resolution of the normal cantilever with photodiode and are more expensive.

1.2.2 Dynamic force sensing

Dynamic force sensing makes reference to a sensor that is oscillating near its resonance frequency. To do this with an AFM cantilever, for example, it must be attached to a piezo actuator in order to make it oscillates. Still generally, the AFM cantilevers have a very low quality factor and stiffness. In consequence, signal to noise radio are high, thus, obtaining small amplitudes of oscillation is challenging, spatially in the air. The last ones are required for high resolution force sensing and for true non-contact mode imaging to avoid tapping the surface. Another type of sensors commonly used for dynamic force sensing are the tuning forks.

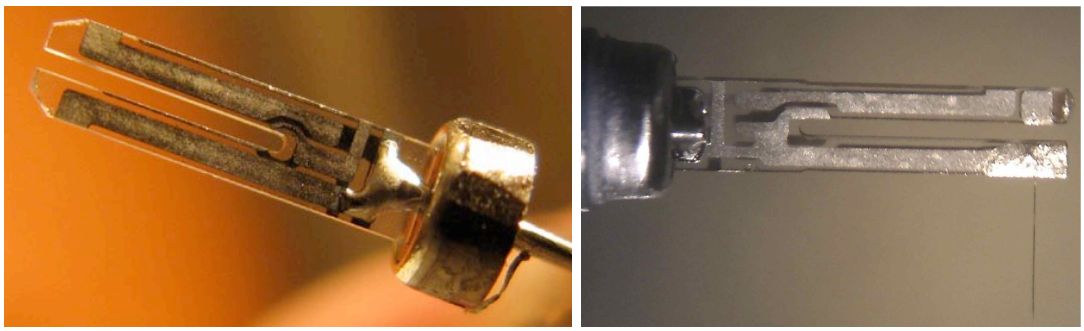

(a) *Tipless tuning fork.* **(b)** *Tuning fork with tip and mass compensation*

Figure 1.13 - *A Piezoelectric quartz sensors: the tuning fork .*

Since 1995, specific piezoelectric quartz forks known as tuning forks started to be used in SPM. They have been widely used in the watch industry. Recently,

they have also been used as force sensors, mainly for imaging and manipulating matter under a scanning probe microscope [KG95, Gie00, CAR09], and to function as force sensors inside SEM thanks to their simple read-out system by replacing laser optics [TS98]. The high quality factor makes them ideal for dynamic force feedback in the air. Additionally, the self sensing capabilities allows them to move freely without the need of recalibration.

Force measurement with a tuning fork is possible with standard AFM dynamic force sensing techniques, such as amplitude/phase modulation (AM/PM) and frequency modulation (FM). For the first, the sensor is oscillating at the resonant frequency. A lock-in amplifier can be used in order to separate amplitude and phase from the original signal. From these two signals, the force can be obtained through an analytical conversion formula [KvEO09, HR08]. For the second, an Automated Gain Controller (AGC) and a Phase-Locked Loop (PLL) controller are used to obtain the resonant frequency of the tuning fork. With the shift of the resonant frequency, the gradient of the force can be obtained [Gie97, SJ04].

Selecting AM or FM depends mainly on the required settling time τ of the tuning fork. For AM-AFM regulation, the reaction time $\tau = Q/(\pi f_0)$ (where f_0 is the resonant frequency and Q the quality factor) is highly dependent on the quality factor (Table 1.2). Furthermore, the quality factor is higher in the vacuum conditions of the SEM, and consequently, the bandwidth analysis will be limited. FM-AFM removes the time constant dependency [AGHR91] of the analysis, thus allowing wide bandwidth with a high quality factor. This, therefore, makes it the primary selection for this work.

Table 1.2 - *Amplitude modulation vs frequency modulation*

	AM/PM	**FM**
Electronic Sensing	Amplitude (V) / Phase($^\circ$)	Frequency shift (Δf)
$\rightarrow$ Physics Sensing	Force	Force gradient
Settling time	$\tau = Q/(\pi f_0)$	$\tau \simeq 1/f_0$

The main problem of the tuning fork is the proper calibration for quantitative force measurement. Classic calibration techniques based on AFM cantilever shouldn't be used due to the different geometry. In the following, the different models used for the quartz oscillator in the bibliography are presented. First the model of the sensor alone will be present and then the model of the sensor in contact.

1.2.2.1 Single prong/Qplus dynamic model

Initially, the tuning fork was modeled as a single prong with the cantilever dynamic model [SJ04]. Only the effective mass and stiffness of one prong was considered (Fig. 1.14):

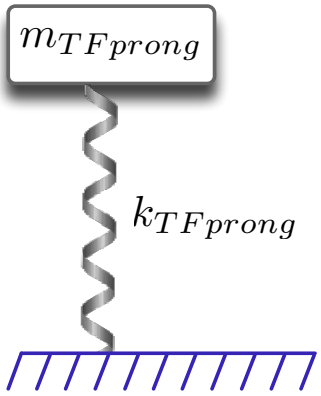

Figure 1.14 - *Schematic diagram of simple tuning fork model without contact*

$$\Omega^2 = \frac{k}{m} \tag{1.2}$$

were Ω is the angular frequency of the prong, k the stiffness of the prong, and m the effective mass of the prong. To be able to use this model, one of the prongs of the tuning fork needs to be blocked. This configuration is called Q-plus. However, this makes the quality factor of the sensor dramatically decrease. When the two prong are in oscillation, this model can led to an error higher than one hundred percent. In consequence, the two prongs need to be considered in the model as well as the coupling between the two.

1.2.2.2 Non-contact mass balanced model

Castellanos et al [CAR09] proposed a model where not only the two prongs are considered but a virtual spring between the two prong kc. (Fig. 1.15). This spring is actually the effect of the tuning fork body stiffness at the end of the prong. The dynamic equations of the system of Fig. 1.15.(a) can be written as:

$$\begin{cases} m\ddot{x}_1(t) + (k + k_c)x_1(t) - k_c x_2(t) = 0 \\ m\ddot{x}_2(t) + (k + k_c)x_2(t) - k_c x_1(t) = 0 \end{cases} \tag{1.3}$$

where x_1, x_2, $\ddot{x}_1$ and $\ddot{x}_2$ are the position and acceleration, m the mass and k, the stiffness of each of the prongs To obtain the eigenfrequencies of the system the following equation needs to be solved:

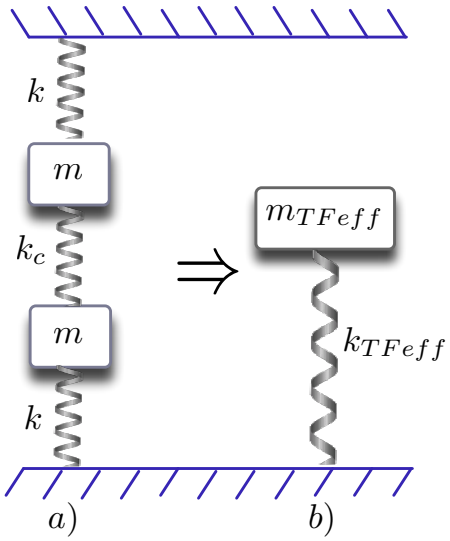

Figure 1.15 - *Schematic diagram of tuning fork coupled oscillators model with noncontact*

$$det \begin{vmatrix} k + k_c - \omega^2 m & -k_c \\ -k_c & k + k_c - \omega^2 m \end{vmatrix} = 0 \tag{1.4}$$

This leds to Eq. 1.5 where Eq. 1.6 is the solution of the system.

$$\omega^4 m^2 - \omega^2 m\,(2k + 2k_c) + k^2 + 2kk_c = 0 \tag{1.5}$$

$$\omega^2 = \frac{k + k_c \pm k_c}{m} \tag{1.6}$$

The 2 solutions of the previous system represent the 2 oscillation modes of the system. For the first, the two prongs are in phase and the distance between the two is kept constant thus not depending on k_c. The second mode, anti-phase, is the typical oscillation mode of the tuning forks due to the configuration of the electrodes:

$$\begin{cases} \omega^2_{phase} = \frac{k}{m} \\ \omega^2_{anti-phase} = \frac{k+2k_c}{m} \end{cases} \tag{1.7}$$

where $m_{TFeff} = 2m$ and $k_{TFeff} = 2(k + 2k_c)$ of anti-phase oscillation. This model allows the use of the tuning fork with the two prongs oscillating, avoiding a quality factor drop due to the blocking of one prong as in previous section.

1.2.2.3 Balanced tuning fork in contact

When there is a contact with a flexible structure, a stiffness Δk needs to be added in parallel to the stiffness of the prong in contact, the resulting schematic is Fig.

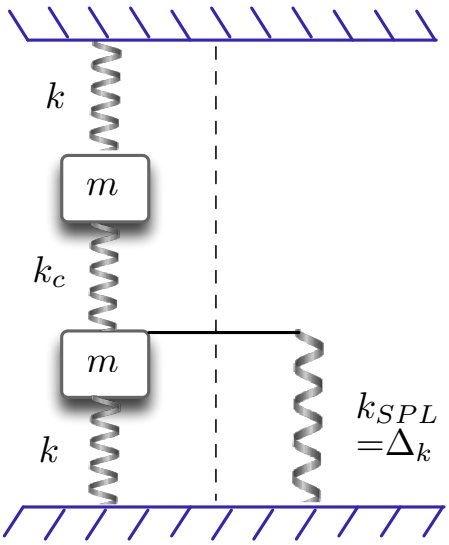

Figure 1.16 - *Schematic diagram of the tuning fork coupled oscillators with one in contact with a spring*

1.16 and resulting system Eq.1.8. It is this stiffness Δk what we want to know with the frequency shift of the sensor. It is the measured gradient of the force.

$$\begin{cases} m\ddot{x}_1(t) + (k + k_c + \Delta k)x_1(t) - k_c x_2(t) = 0 \\ m\ddot{x}_2(t) + (k + k_c)x_2(t) - k_c x_1(t) = 0 \end{cases} \tag{1.8}$$

Resulting in:

$$\omega^2 = \frac{2k + 2k_c + \Delta k \pm \sqrt{4k_c^2 + \Delta k^2}}{2m} \tag{1.9}$$

Using the general equation (Eq. 1.9) for anti-phase:

$$\frac{f_1 - f_0}{f_0} = \frac{\frac{1}{2\pi}\sqrt{\frac{2k+2k_c+\Delta k+\sqrt{4k_c^2+\Delta k^2}}{2m}}}{\frac{1}{2\pi}\sqrt{\frac{k+2k_c}{m}}} - 1 \tag{1.10}$$

$$\Delta k = \gamma - \frac{k_c^2}{\gamma} \tag{1.11}$$

where $\gamma = \left(\frac{\Delta f}{f_o} + 1\right)^2 (k + 2k_c) - k - k_c$, f_1 is the anti-phase resonant frequency of the tuning fork in contact from eq. 1.9 and f_0 the anti-phase resonant frequency of the tuning fork before contact from eq. 1.7.

Generally, $\Delta k << k$ and the previous equation can be simplified:

$$\begin{cases} \omega^2_{phase} = \frac{2k+\Delta k}{2m} \\ \omega^2_{anti-phase} = \frac{2k+4k_c+\Delta k}{2m} \end{cases} \tag{1.12}$$

and so:

$$\Delta k = \frac{4\left(k+2k_c\right)\Delta f}{f_0} \tag{1.13}$$

The three models can be summarized as:

$$\begin{cases} \Delta k = \frac{2k\Delta f}{f_0} & Singlecantilever \\ \Delta k = \frac{4(k+2k_c)\Delta f}{f_0} & Castellanos \\ \Delta k = \gamma - \frac{k_c^2}{\gamma} & Generalmodel \end{cases} \tag{1.14}$$

where, Δk is the stiffness of the measured object and Δf the frequency shift obtained with the AGC (Amplitude Gain Controller) and PLL (Phase Lock Loop) controller. None of these methods, however, includes neither the stiffness of the tip or the angle of attachment in the model. It is a challenge. Further details on this will be showed in the first section of chapter 3.

1.3 Nanocharacterization

Recently, many ultraflexible and elastic micro/nano structures have been synthesized as building blocks to create nanoelectromechanical systems (MEMS/NEMS) [SJ08, SSRN09]. Carbon NanoTubes (CNTs) [DHR$^+$96, HCOL01, LCD99, Iij91], NanoWires (NWs) [CL01], and nanohelixes [MKNI90, ZZB$^+$94, KW03, GDM$^+$05, BSZ$^+$06,BDN$^+$06] are the most widely synthesized and are considered as the promising elements for various NEMS and nanoelectronics. However these devices are principally limited to laboratory prototypes, and so, they have not yet been commercialized. This is mainly due to the manufacturing challenges and physical properties which remain little known. For both of these problems, precise knowledge of the mechanical properties of these nanostructures is imperative. For example, the precise mechanical properties of NWs and NTs can predict their device characteristics. It also contributes to their arrayed growth and assembly in controlled direction thus, the manufacture of devices such as field emitters can be achieved.

The mechanical properties of these one-dimensional (1-D) nanostructures could be studied using conventional Atomic Force Microscopy (AFM) thanks to their simple mechanics. However, recently fabricated three-dimensional (3-D) nanostructures

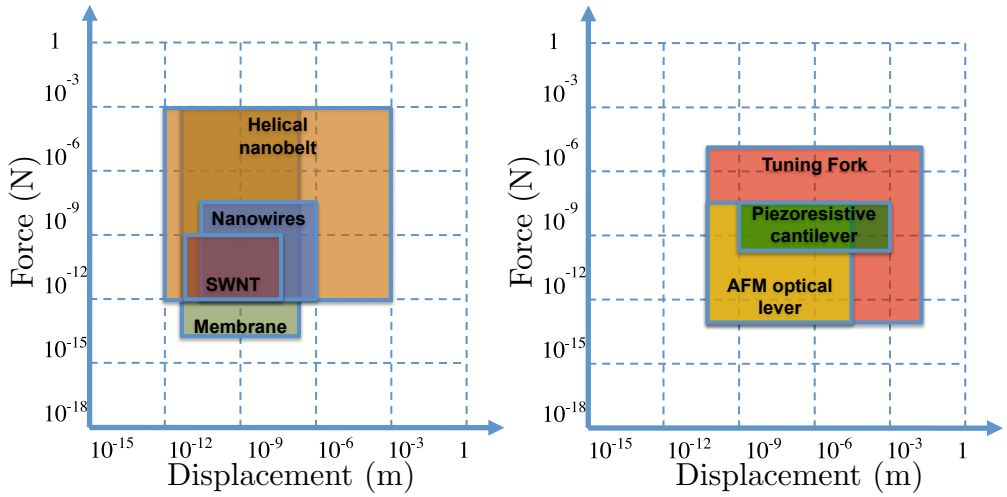

(a)Ultra flexible nanostructures (b)Force sensors

Figure 1.17 - *Force vs displacement diagram*

such as 3-D nanohelixes face their challenges to understand the complex mechanics. 3-D nanohelixes are inspired by nature and its complex mechanical properties. As examples, the mechanics of 3-D biological structures in nature such as deoxyribonucleic acid (DNA), proteins, cells, or tissues are complicated and being studied [VS06]. As inorganic nanohelixes, the electrical and mechanical properties of SiGe/Si/Cr and SiGe/Si Helical Nanobelts (HNBs) were recently characterized separately through experiments and simulations [BSZ+06]. The fabrication and mechanical characterization of InGaAs/GaAs HNBs have been also described [BDN+06]. Their excellent flexibility provides new avenues for fabrication of ultra-small force sensors with high resolution as depicted in Fig. 1.17.a. The displacement of these nanohelixes was detected by a recently developed visual recognition [KDZN10] or piezoresistive smart sensing mechanism [HH09]. However their mechanical properties were only studied in the limited upper displacement region mainly due to the lack of proper calibration tools for a full range mechanics study [BSZ+06, BDN+06] (Fig 1.18.b). A high resolution and long range mechanical calibration system is therefore necessary.

As conventional force calibration tools, AFM [MBE99], piezoresistive cantilever [PGP07], capacitive force sensor [BMN09] and other microelectromechanical systems (MEMS) [SN04] have mostly been used. However, their sensing resolution and range are also limited as depicted in Fig. 1.17.b. This means that they are insufficient to characterize the full range of nanostructure mechanics although it is essential to their device applications. For this reason, we need large range force sensing tools,

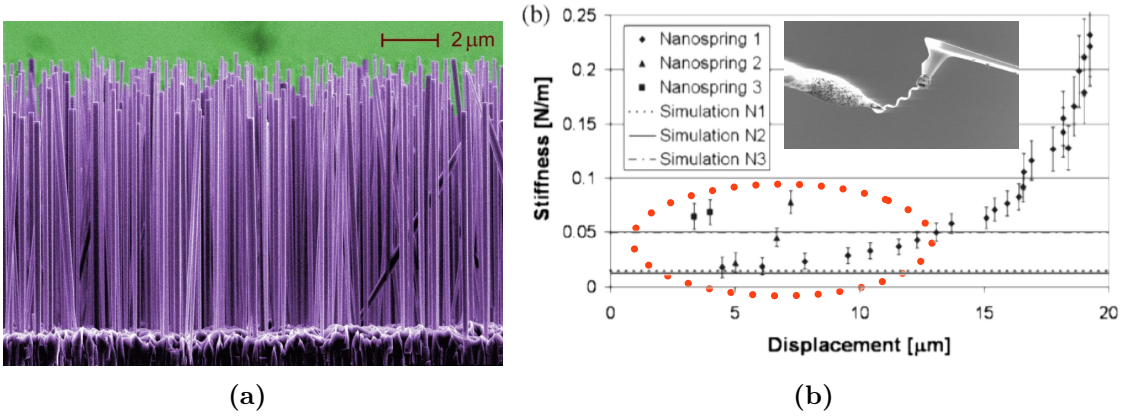

(a) (b)

Figure 1.18 - *Nanostructures examples (a) NIST array of SIlicon NWs (b) Helical Nanobelt Characterisation with an atomic force microscope cantilever. Note the red dot area where the characterization is imprecise ([BSZ+06]).*

One of the main ideas of this section is the interest in dynamic force sensing for large range force sensing, and take advantage of those techniques for further experiments on micro/nanomanipulation.

1.4 Objectives and proposed solution

In this chapter, the state of the art of nanorobotics based on atomic force microscopy was presented. Following the challenges presented for that, the objectives of this work are:

3D micromanipulation with force feedback. It is presented in chapter 2. The aim of this chapter is to show the capabilities of the two tip AFM system for 3D micromanipulation when force feedback is used. A nanotweezer is made with two AFM cantilevers with protrudent tips to be able to do pick and place. Two applications are presented. For the first, two layer micropyramids are made with nylon microspheres of 3 μm to 4 μm diameter. For the second, nanocrosses are made with silicon nanowires of diameters of 100nm. For this, the nanotweezer is used to pick one side of the nanowire and slide it on top of the other. It is an introductory chapter on the system that shows the potential applications with force feedback as well as the limitations of the system. The last, mainly being the speed of the scan for manipulation and the dexterity of the arm due to the cantilevers calibration.

Thus, the necessity of studying dynamic force sensor for a potential integration with the system.

A study on dynamic force sensors for nanocharacterization. This is presented in chapter 3. We want a dynamic force sensor that is able to solve issues in nanocharacterization and that could be easily integrated in the AFM of chapter 2. A tuning fork is used for mechanical characterization of ultra flexible nanostructures. Two sub-objectives are achieved in this chapter. Fist, **wide range mechanical characterization** with the gradient force feedback of the sensor. For this, an helical nanobelt is considered as an example of nanostructures due the wide range needed for the mechanical characterization as well as the fact that it was never achieved before due to the lack of wide range sensing tools. Second, show the **selfsensing capabilities of the dynamic oscillator for a mechanical characterization while the sensor is moving**. In this case the surface of micromembrane structure used for micro mirrorapplications is mechanically characterized.

Parallel imaging and manipulation with dynamic force sensors. The previous system AFM system composed of two AFM cantilevers is limited in speed and dexterity. A change to a dynamic force sensor is proposed to address those issues. This will be presented in chapter 4. Its is the final chapter a represents an integration of the two tip AFM presented in chapter 2 with the dynamic force sensors presented in chapter 3. Here, a new AFM system is presented with two tips. One the the tips, is an AFM cantilevers and is used for manipulation. The other tip is a fast quartz oscillator for fast AFM imaging in true non-contact mode. The system is validated trough a series of experiments. First, speed and piezo calibration is validated with hard surface imaging, then the non-invasive capabilities are shown with imaging of loose object on top of a hard substrate. Finally, a manipulation task with the two cooperative arms is presented were three gold colloids are pushed with the cantilever, and AFM images done with the dynamic force sensor.

Chapter 2

Two tips based micromanipulation with force microscopy

Contents

In chapter 1, the state of the art in micro and nanomanipulation based on AFM has been presented. One of the main challenges presented is the ability to manipulate microobjects in 3D in air conditions. In this chapter a new system based on a two tip AFM is made. The key of this system is how to take advantage of the force feedback of both arms to build a microgripper with grasping force feedback in order

to do 3D micromanipulation.

Two application of the system are presented in this chapter. First two layer 3D micropyramids are done with microspheres of diameters of 3 μm $\sim$ 4 μm. In the second part, nanocrosses are build with SiNW (Silicon NanoWires). The presentation of these applications in the following is divided into four parts. For each, the system is presented followed by the a manipulation protocol. Then the grasping force is estimated and the results are presented.

The works presented in this chapter have been conjoinctly done with Dr. Hui XIE.

2.1 Three dimensional micromanipulation of microspheres

In this section, in order to achieve the 3D manipulation of microobjects with feature sizes from submicron to 10 μm, an atomic force microscope (AFM) based 3D micromanipulation system with a nanotip gripper is developed. This system can be used to build 2D micropatterns by pushing and pulling microobjects on a single plane, and, more importantly, to achieve the pick-and-place micromanipulation with sufficient interaction force sensing. The system mainly consists of two collaborating AFM cantilevers with protrudent tips and two corresponding nanopositioning and optical levers. A nanotip gripper is constructed by these two tips to achieve a procedure of 3D micromanipulation with general steps of contact detecting, grasping, picking up, transporting and releasing. We have used the developed system to fabricate five micropyramids with two layers by manipulating microspheres with diameters of 3 μm $\sim$ 4 μm. Compared with other means of pick-and-place micromanipulation in air, the developed system is more controllable due to the real time interactive force sensing, and without obstacle on the microsphere releasing due to very sharp tips of the gripper.

2.1.1 System configuration

As shown in the bottom right inset of the Fig. 2.1, the proposed AFM is equipped with an optical microscope and two sets of similar devices commonly used in a conventional AFM, including two cantilevers (ATEC-FM) with corresponding nanopo-

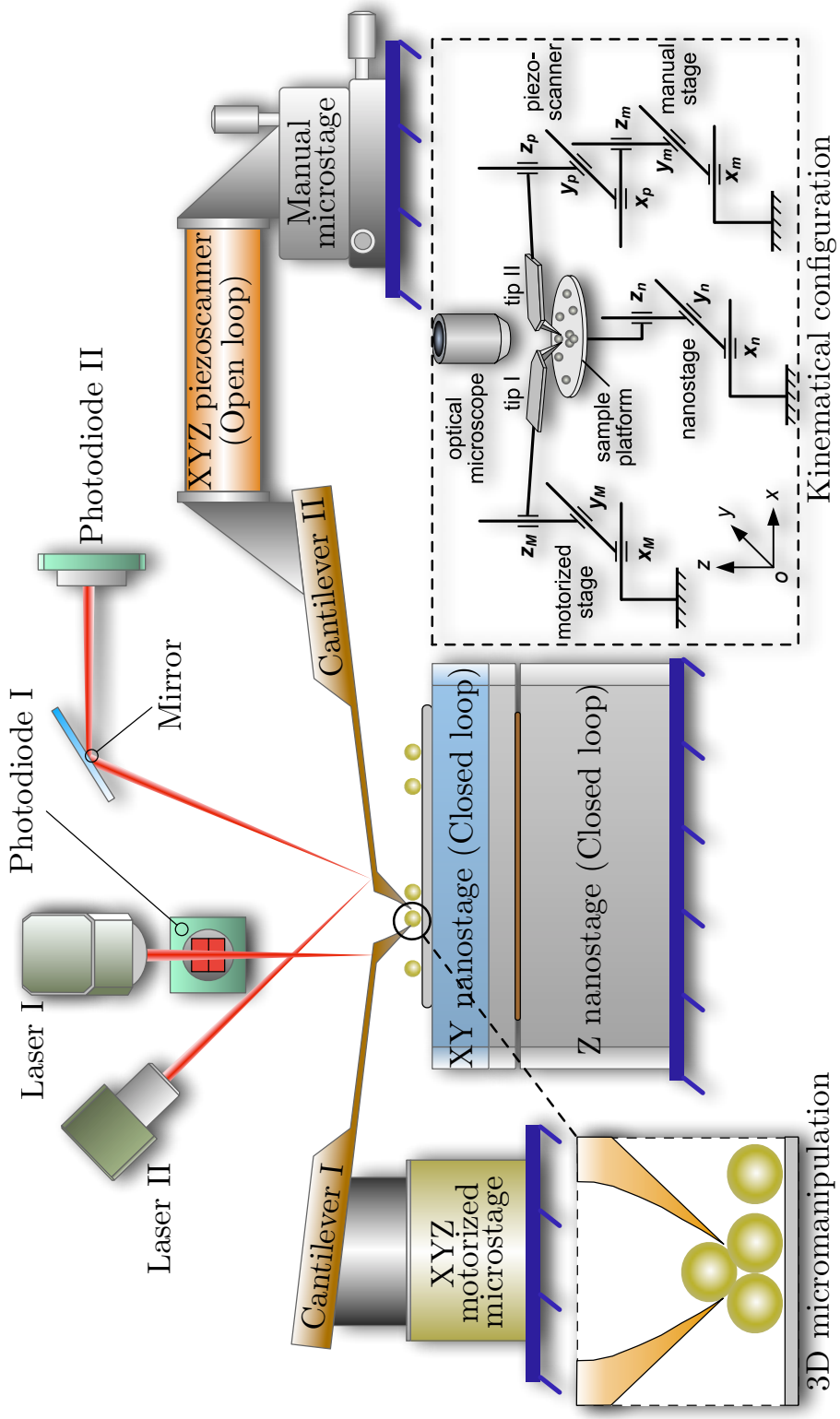

Figure 2.1 - *System configuration of the two tip AFM for 3D manipulation of microspheres. Bottom right inset represents the kinematical configuration of the system.*

sitioning devices and optical levers. The optical levers, typically composed of a laser and a quadrant photodiode, that are believed to be more sensitive and reliable detection device than other means [MA88], are arranged on two vertical planes and used to detect actions of both cantilevers, as seen in Fig. 2.1. The bottom left inset of Fig. 2.1 shows that the protrudent tip of each cantilever has an tilted angle about 70° on the side view. These tips are employed as end-effectors to build a nanotip gripper with a clamping angle of 40°. The nanotip gripper is used to pick up and place the microobject to its target position. The configuration of the system can be described as follows. The complete hardware configuration can be seen in Fig. 2.2.

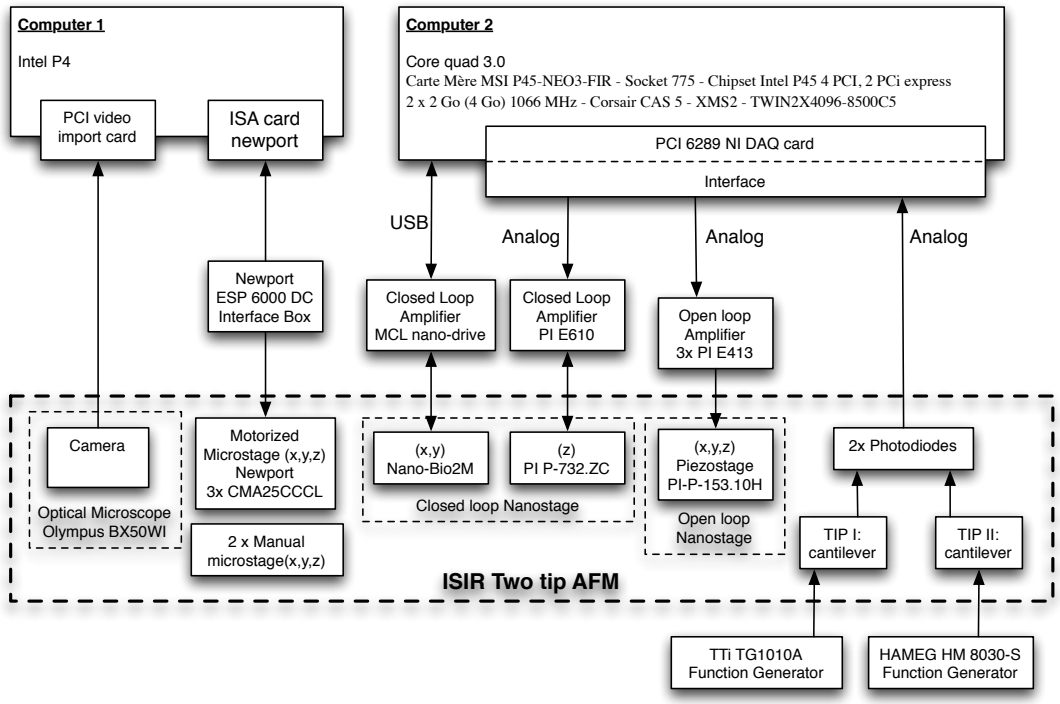

Figure 2.2 - *Hardware diagram of the two tip AFM setup.*

1. Cantilever I, which is immovable during the micromanipulation, is fixed on an XYZ micropositioning stage for coarse positioning. The normal stiffness of Cantilever I and the sensitivity of its optical lever are calibrated as 2.43 N/m and 0.65 nm/mV, respectively.

2. Cantilever II is actuated for grasping operations by an XYZ piezotube (PI P-153.10H) with a scan range of 10 μm and a resolution of subnanometer on each axis. The piezotube is well compensated by the Prandtl-Ishlinskii operator on its hysteresis [KK01] and mounted on an XYZ manual microstage. The normal

stiffness of Cantilever II and the sensitivity of its optical lever are calibrated as 2.48 N/m and 0.58 nm/mV, respectively.

3. An XYZ nanostage (MCL Nano-Bio2M on the XY axes, PI P-732. ZC on the Z-axis) with a maximum motion range of 50 μm x 50 μm x 10 μm and a closed-loop resolution of 0.1 nm is employed to support and transport samples.

4. A data acquisition card (NI6289) with a resolution of 18 bits in A/D transfer and a maximum sampling frequency of 750 kHz is used for data acquisition from the optical levers and actuate the XYZ piezotube by exporting voltage signals to three independent amplifiers.

2.1.2 Manipulation protocol

Microparticles and microspheres are being intensively investigated as significant experimental materials for micromanipulation. Thus, a protocol is made for a specific application of the microparticles or microsphere deposited on the substrate. However, applications of such a protocol can also be extended to the pick-and-place operation of other types of microobjects dispersed on the substrate. As shown in Fig. 2.3, a procedure of the pick-and-place mainly involves:

1. *System Initialization:* Set each axis of the nanostage and the piezotube on a proper position, providing the pick-and- place operation with enough displacement on each axis.

2. *Trajectory Planning:* Trajectory planning is started after the coarse positions of microspheres is detected with the optical microscope, providing a distribution of all the microspheres and subsequently, fine positioning of each microsphere will be fulfilled with amplitude or force feedback from the cantilevers.

3. *Contact with Tip I:* As seen in Fig. 2.3.(a), keeping a gap between the dithering Tip I and the substrate when it is approaching to the microsphere by moving the piezotube on the X-axis. An actual grasping point and contact on the microsphere can be detected by the amplitude feedback, **which will be discussed in next section.**

4. *Contact with Tip II:* As Tip I is in contact with the microsphere, contact between Tip II and the microsphere is also achieved in Fig. 2.3 (b) by following the process in the last step, building a nanotip gripper in Fig. 2.3.(c).

5. *Pick up, Transport and Place:* Once the grasping is ready, as shown in Fig. 2.3.(d), the microsphere is picked up, transported and placed by moving nanostage on each axis with proper displacements that depend on the location of

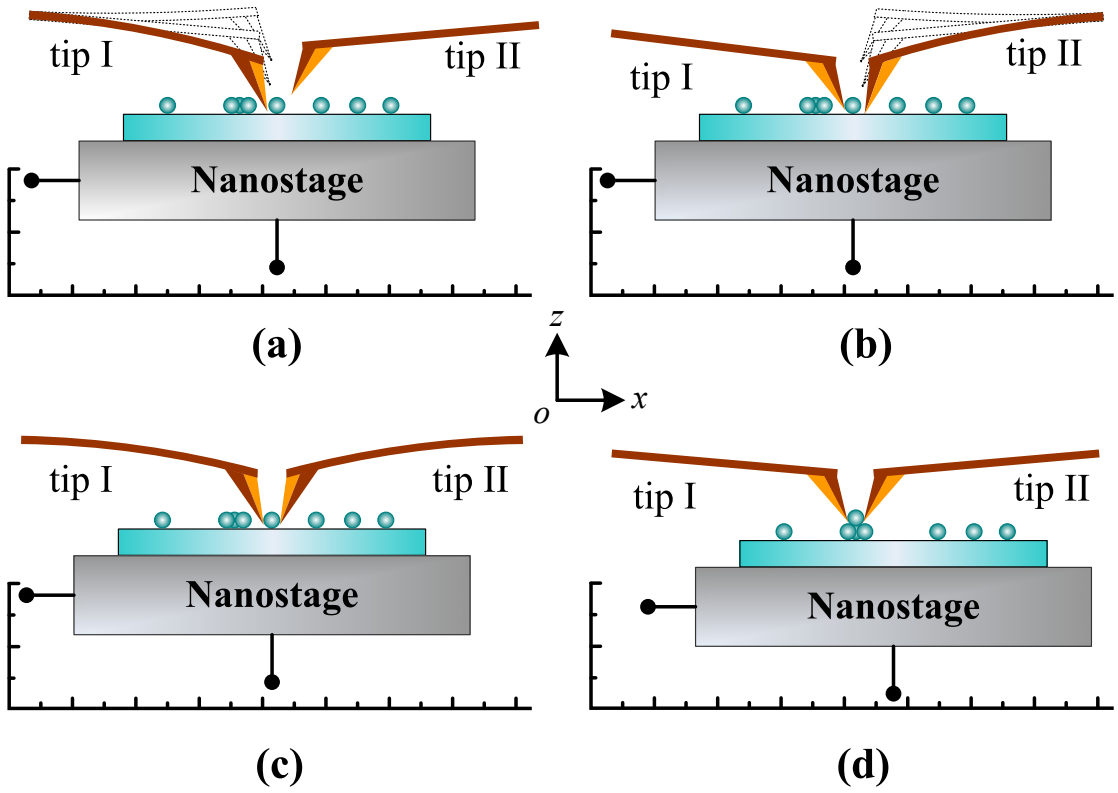

Figure 2.3 - *Protocol of the pick-and-place operation of microspheres. Four main steps are involved. The dithering Tip I is used to locate the grasping point by local scanning with amplitude feedback (a). In the step (b), the grasping point between Tip II and the microsphere is detected with the dithering Tip II. The grasping operation is ready for pickup as both tips contact with the microsphere. The pick up manipulation is achieved in step (c) by moving the nanostage on the Z-axis. (d) A micropyramid is fabricated as the microsphere is placed on the first microsphere layer.*

the destination and the size of the microsphere. The whole procedure of the 3D micromanipulation is monitored by the real time force sensing.

2.1.3 Grasping point searching and contact detection

As shown in Fig. 2.4.(a), the dithering cantilever with the first mode of oscillation is utilized to search grasping points on the diameter of the contact circle of the microsphere and detect the contact using real time amplitude feedback. As shown in the insert I of Fig. 2.4.(a), the dithering cantilever sweeps on the Y-axis with distance about half of the microsphere diameter when it is approaching the microsphere with

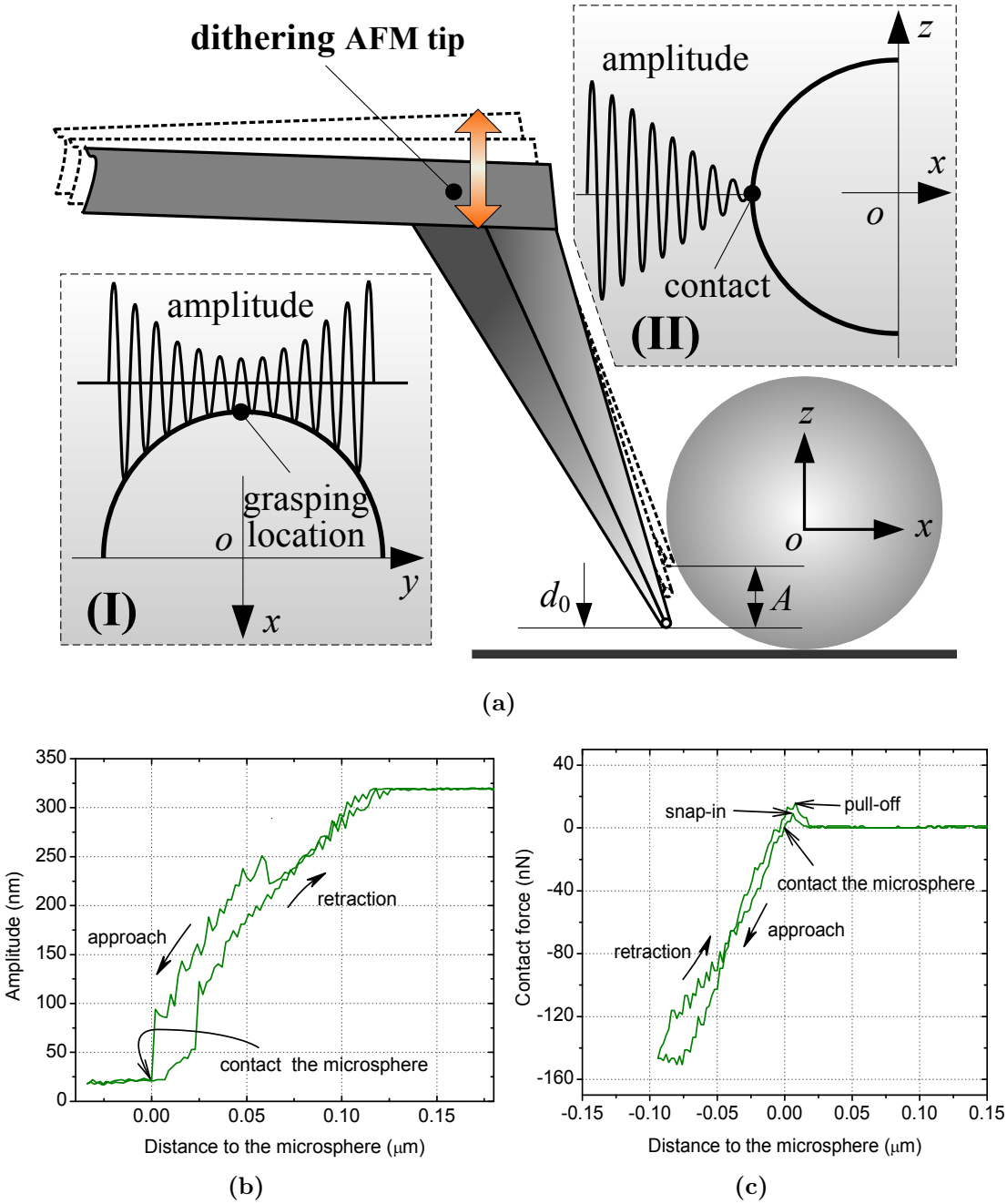

Figure 2.4 - *Schemes and experimental results of grasping point searching and contact detection on a microsphere. (a) Schematic of grasping points locating (insert I) and contact detection (insert II) using the amplitude feedback. A is the amplitude and d_0 is the distance between the tip and the substrate. (b) Amplitude responses of the cantilever when it is approaching the contact point on the microsphere. (c) Normal force responses could also be employed for the contact detection.*

a gap of 500 nm to the substrate. When the tip laterally taps on the microsphere, the grasping point can be accurately located by searching for the minimum amplitude response. The grasping point is well located with an accuracy of ± 10 nm that is in much excess of the resolution the optical microscope. As the scheme depicted in insert II of Fig. 2.4.(a), amplitude feedback is also used for contact detection. As seen in Fig. 2.4.(b), contact between the tip and the microsphere is achieved as the amplitude reduces to a steady value near zero. When the dithering tip returns to its natural amplitude, a hysteresis loop is induced from the transitions between adhesive and repulsive forces between the tip and the microsphere [GP02].

In addition, contact can be also detected by the normal force response from the cantilever. As shown in Fig. 2.4.(c), a full normal force response in an approach-retraction loop can be recognized by steps of snap-in, contact and pull-off, which is usually in the presence of the tip-substrate contact. In our experiments, as the contact between Tip I and the microsphere is ready, Tip I retraces 5-10 nm in order to keep a tiny gap between Tip I and the microsphere. This gap enables a smart recognition of grasping state as Tip II contact with the microsphere with a slightly further push. Compare with operations under the optical microscope, the amplitude detecting method has two obvious advantages: 1) Grasping point and contact can be detected below the opaque components, more importantly, with accuracy that is far beyond the capability of the microscope. 2) Benefiting from the accurate force and amplitude measuring of the optical lever, the grasping points and contact can be accurately detected with very weak interactions at the scale of nano-Newton, protecting the fragile tips and microobjects from damage.

2.1.4 Force sensing during pick-and-place

In order to measure the interactive forces between the tips and the microsphere during the procedure of the pick-and- place, as shown in Fig. 2.5, the interactive forces on Tip I can be measured as a normal signal from the well-calibrated photodiode by the following equations:

$$\begin{cases} F_{z1} = F_{f1} \cdot cos\,(\theta/2) + F_{r1} \cdot sin\,(\theta/2) \\ F_{x1} = F_{r1} \cdot cos\,(\theta/2) - F_{f1} \cdot sin\,(\theta/2) \end{cases} \tag{2.1}$$

where F_{z1} and F_{x1} are the bending forces applied respectively on the Z-axis and the X-axis, F_{r1} is a repulsive force and F_{f1} is a friction force between Tip I and the microobjects. In the actual use, a clamping angle 40° and a normal $\mu = 0.3$ are used. Thus, from Eq. 2.1, F_{z1} and F_{x1} can be solved as $F_{z1} = 0.623 \cdot F_{r1}$ and $F_{x1} = 0.837 \cdot F_{r1}$. The bending angular deformation ϕ associated with a torque M

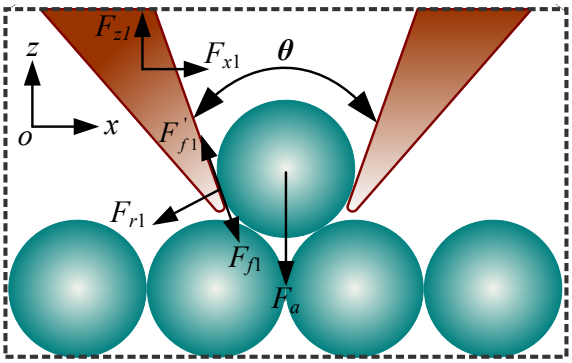

Figure 2.5 - *Diagram of nanogripper while grasping a microsphere*

applied on the end of the cantilever can be calculated as:

$$\phi = \frac{M \cdot L}{2 \cdot E \cdot I} \tag{2.2}$$

where L is the beam length of the AFM cantilever, E is Young's modulus of the cantilever and I is the moment of inertia on the cantilever's cross-section area. A torque M_1 generated from the F_{z1} with a long turning lever of the cantilever length $L = 225\mu m$. In contrast, the torque M_2 generated from the F_{p1} is just with turning lever of the tip length 10 μm. From Eq. 2.2, the cantilever moments associated with the normal signal output of the photodiode can be estimated as $M2 \leq 0.06 \cdot M_1$. Thus, the contribution of from the F_{x1} can be neglected. Therefore, the F_{p1} can be simplified estimated as $F_{z1} = \beta_1 \cdot \Delta V_1$, where $\beta 1$ is the normal force sensitivity of the optical lever on Tip I, ΔV_1 is the voltage response of the photodiode due to the force load. A similar result can be deduced on TipII. Once the F_{z1} and F_{z2} are known, the adhesion force on the nanoobject F_a can be estimated as:

$$F_a = F_{z1} + F_{z2} = \beta_1 \Delta V_1 + \beta_2 \Delta V_2 \tag{2.3}$$

where β_2 and ΔV_2 are the normal sensitivity and the voltage output on Tip II, respectively.

Fig. 2.6 shows a full force spectroscopy curve during the pick-and-place operation of a microsphere deposited on the glass slide with an environmental temperature of 20° C and relative humidity of 38%. The force spectroscopy curve is synthesized from force responses on both tips. The curve starts from contact state between the microsphere and the substrate. During the pickup, when the nanostage position reaches -170 nm in Z-axis, the gripper-microsphere pulls off the substrate with a pull- off force of 746 nN. After this, the force curve returns to -220 nN other than the initial force due to the contribution of friction forces between the gripper and the

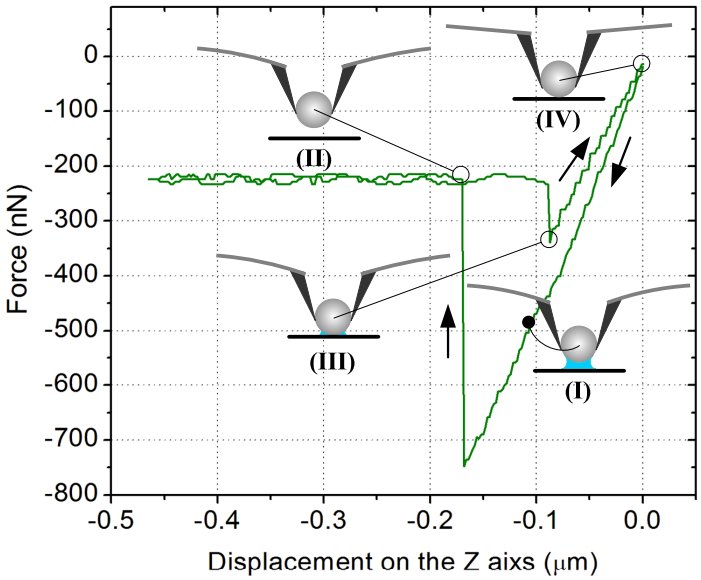

Figure 2.6 - *Synthesized normal force responses on both microcantilevers during the pick-and-place manipulation of a microsphere. (I) pick-up. (II) Pull-off. (III) Snap-in. (IV) Contact on the retraction branch.*

microsphere. The insert I shows that the microsphere relatively slides down from the gripper during the pick-up operation, which leads to a bending deformations kept by the frictions on the nanotips (insert II). During the retracting branch, an earlier snap-in occurs with a distance of about 50 nm to the starting point, indicating that the microsphere slides with the same distance during the pick-up operation (insert III). Further retraction leads to a continue increase with a higher slope than that of the pick-up until both the nanostage position and the magnitude of the normal force get back to the initial grasping state (insert IV). Once such a force spectroscopy curve occurs during the pick-and-place manipulation, a stable grasping as well as a successful releasing operation could be validated.

2.1.5 Experimental results and discussion

Fig. 2.7 shows the 3D micromanipulation process of the micropyramids. Fig. 2.7 (a) and (b) are captured when the first layer of the pyramid II and VI are assembled, respectively. The image in Fig. 2.7 (c) is captured as the first layer of the five pyramids has been completed, in which twenty microspheres have been placed on the reference positions with pick-and-place operation. Once the first layer is ready, the remaining five microspheres are sequentially picked up and placed on each reference positions on the second layer. Fig. 2.7 (d) and (e) describe the transporting process

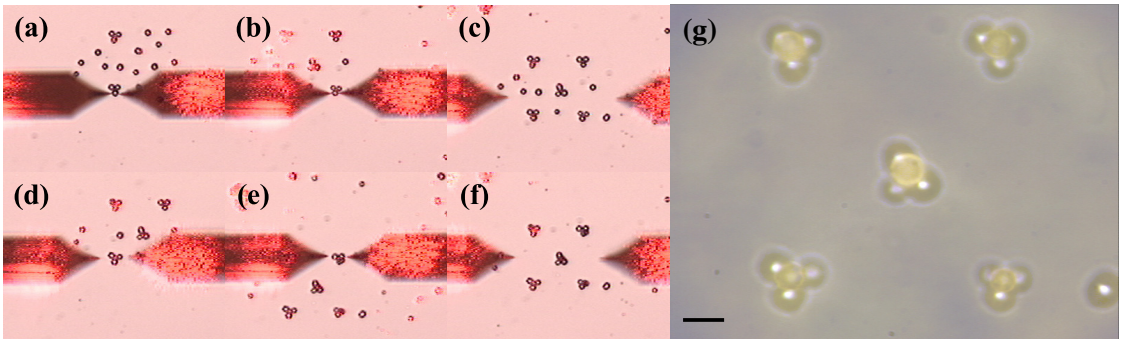

Figure 2.7 - *Assembly results. (a)-(c) show three images intercepted from assembly process of the first layer of the micropyramids. (d)-(f) depict assembly process of the second layer of the micropyramids. The images (a)-(f) are captured under magnification of 20x. (g) The 3D microassembly results under magnification of 100x, in which the scale bar represents 5 μm.*

of the twenty-first and the last microsphere, respectively. The ultimate result is shown in Fig. 2.7 (f). In addition, the assembly result is displayed more distinctly under the microscope with a 100x objective, as seen in Fig. 2.7 (g). Concerning about more details, several aspects of the microassembly should be explained as follows.

As the AFM tip radius is about 10 nm, with respect to the microsphere-substrate contact, the microsphere-tip contact area is much smaller, which leads to tiny adhesion forces between the gripper and microsphere. However, in order to achieve smoothly releasing operation, firstly, it is should make certain the tip-microsphere contact with only the tips of the AFM cantilevers by reserving a proper distance between the gripper tip and the substrate in grasping. Moreover, it is of significant importance to ensure a full microsphere-substrate contact by waiting for several seconds before opening the nanotip gripper for the releasing. In addition, the tips should keep dithering in its natural resonance during the whole procedure of pick-and-place manipulation, especially in the process of releasing, for a purpose of reducing adhesion forces between the gripper and the microsphere due to great inertial forces applied to the microsphere [DVRB05]. By applying schemes or strategies mentioned above, obstacle of sticking is estimated in our pick-and-place experiments with microspheres less than 4 μm in diameter. In addition, note that several interrupts occurred with user's intervenes for the nanotip gripper relocation during the whole microassembly of the five micropyramids due to the constraint of the limited motion range 50 μm x 50 μm of the nanostage, which is less than the manipulation range of 56 μm x 56 μm. The gripper relocating is completed by moving the microstage and the manual stage that are used to support Tip I and Tip II,

respectively.

2.2 Nanocrosses fabrication by manipulation of silicon nanowires

In this section, the previous AFM based manipulation system, is modified for manipulation SiNWs. Like the system used for micromanipulation, two collaborative cantilevers with protrudent tips and correspondingly two sets of nanopositioning devices and optical lever are useds. In order to locate tips and the nanoobjects, one of these two tips is employed to fulfill a topography scan on another tip and the nanoobjects, obtaining position information of nanoobjects and the tips before manipulation. Due to the size of the objects, visual feedback from optical microscope cannot be used. Once the image scanning is ready, a nanotweezer is constructed by these two tips to achieve a procedure of 3D nanomanipulation with steps of contact detecting, grasping, picking up, transporting and releasing.

We have used the system to build nanowire crosses by manipulating two types of cone-shaped SiNWs with diameters of 15 nm (top) $\sim$ 70 nm (root) and 25 nm (top) $\sim$ 200 nm (root). Compared with other means of pick-and-place nanomanipulation achieved in the SEM and the TEM, 3D manipulation process using the developed system is more controllable due to the real time interactive force sensing and with much more flexibility in different manipulation environment for various nanoobjects.

2.2.1 System configuration

The hardware used for this experiment is exactly the same as the one used for the previous experiment. The kinematical configuration as well as the role of each of the tips is however, different. The configuration could be described in detail as follows:

1. Cantilever I, employed as an imaging tip before manipulation and then a manipulating end-effector, is fixed on an XYZ micropositioning stage (Fig. 2.8) as the previous system. On the other hand, Cantilever II, as a manipulating end-effector supported by an XYZ manual microstage for coarse positioning, is mounted on the XYZ nanostage. In concecuence, mooving the nanostage will not affect the distance between the Tip II and the substrate compared to previous experiment, and so Tip I is used for AFM imaging.

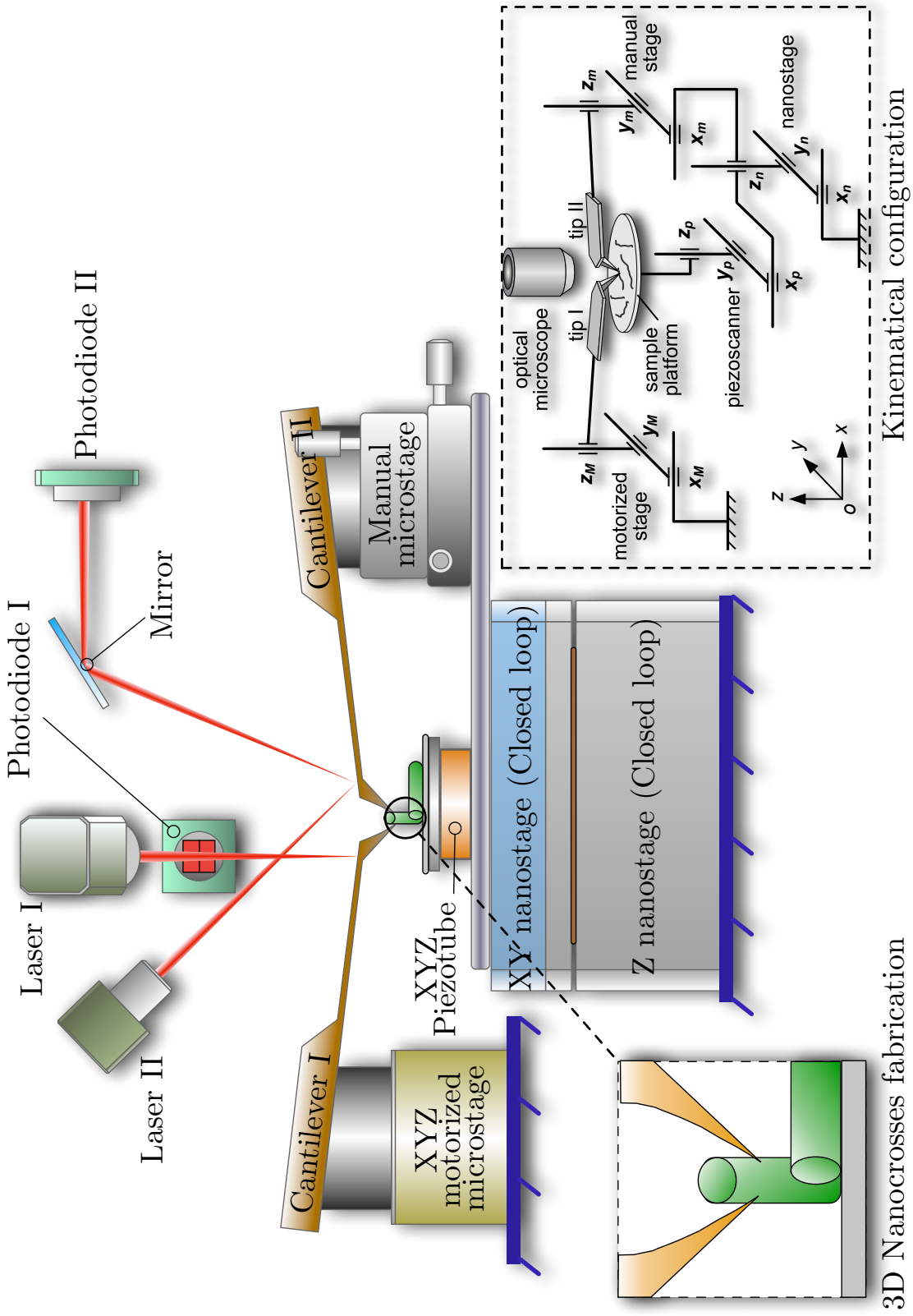

Figure 2.8 - *System configuration of the system for SiNW manipulation*

2. The XYZ piezotube, fixed on the XYZ nanostage, is used to support and transport samples.

3. A typical pick-and-place nanomanipulation scheme made, in which a "nanotweezer" with a clamping angle of $32° - 44°$, constructed from the cantilever I and the cantilever II and each with mounting angle of $6° - 12°$, is utilized to pick up and place the nanoobject to its target position.

2.2.2 Manipulation protocol

Nanowires and nanotubes are being intensively investigated as the promising nanomaterials for applications in nanooptics, nanoelectronics and nanostructures in NEMS. Thus, a manipulation protocol is made for a specific application of the nanowires or the nanotubes deposited on the substrate. However, applications of the protocol also can be extended to the pick-and-place operations on, for example nanoparticles dispersed on the substrate. As seen in Fig. 2.9 (a), a pick-and-place procedure mainly involves:

1. *System Initialization:* Set each axis of the nanostage and the piezotube on a proper position. This setting will provide enough displacement for the nanoobjects manipulation within an image scanning area. Then locate Tip II (on the right) by local scanning using Tip I after a coarse positioning under the optical microscope .

2. *Image Scanning Using Tip I:* Once the locating on Tip II is ready, Tip I (on the left) is employed to fully scan the area of interest, obtaining a topographic image which contains nanoobjects to be manipulated and Tip II. The scanning area on Tip II is determined by the height of the nanoobjects, which should has a comparative maximum image height with the nanoobjects. This step is depicted in Fig. 2.9 (a)-I, in which the nanostage is used track the topography during the image scanning. The scanning image contains two nanowires and the end of Tip II, as shown in Fig. 2.9 (b).

3. *Relocate Tip II:* If the nanomanipulation is performed in an uncontrolled environment, the thermal drift is a notice- able cause of the positioning errors. Therefore, after a long- playing image scanning, relocating Tip II is quite necessary to succeed in constructing of the "nanotweezer".

4. *Approach Tip II to One Nanowire:* Keep a tiny gap (typically 5 nm $\sim$ 20 nm) between Tip II and the substrate, then approach Tip II to one nanowire by moving the piezo- tube on the X axis. An actual contact with the nanoobject

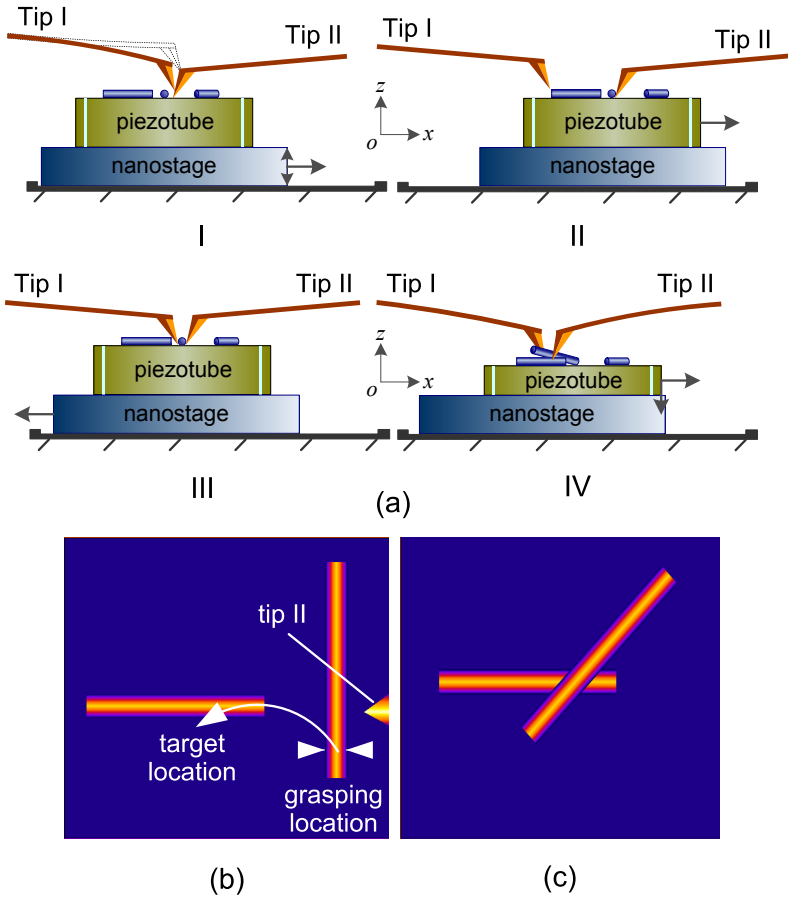

Figure 2.9 - *Protocol of pick-and-place of nanowires. (a) Four steps from step I to IV are involved. (b) Locations of nanowires and Tip II are recorded by a simulated pre-image scan. (c) A nanowire nanocross is built.*

can be predicted by a tiny force load on Tip II. This step is depicted in Fig. 2.9 (a)-II.

5. *Approach Tip I to Tip II:* Similarly, approach Tip I to Tip II to form a "nanotweezer" by moving the nanostage on the X axis until an actual contact with the nanoobject estimated by a tiny force load on Tip I. This step is depicted in Fig. 2.9 (a)-III.

6. *Pick up, Transport and Place:* Once the "nanotweezer" is constructed on the step 5), the nanowire is picked up, transported and placed by moving piezotube on the X, Y or Z axes with proper distances depending on dimensions of the nanowire and the location of the destination.

2.2.3 Force sensing during manipulation

In order to measure the interactive forces between the tips and the nanoobjects, as shown in Fig. 2.10.(b), the 3D interactive forces on Tip I in the defined frame can be determined by normal signals from the photodiode by:

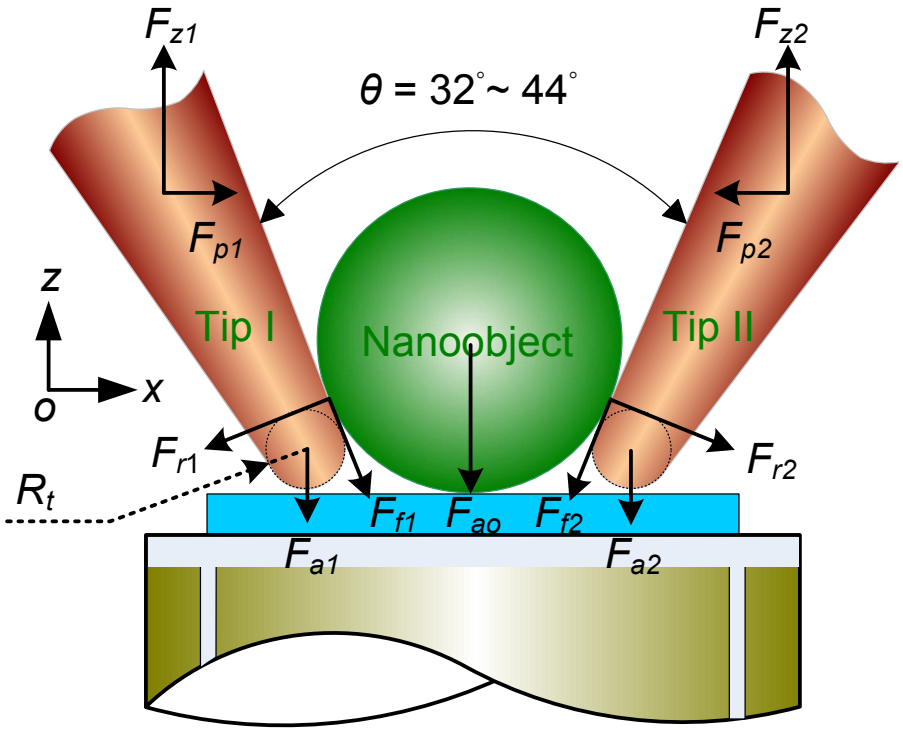

Figure 2.10 - *Force simulation using the nonparallel two-tip gripper*

$$\begin{cases} F_{z1} = F_{f1} \cdot cos\,(\theta/2) + F_{r1} \cdot sin\,(\theta/2) + F_{a1} \\ F_{p1} = F_{r1} \cdot cos\,(\theta/2) - F_{f1} \cdot sin\,(\theta/2) \end{cases} \tag{2.4}$$

where F_{z1} and F_{p1} are the bending forces applied respectively on the Z-axis and the X-axis, F_{a1} is the adhesive force between Tip I and the substrate, F_{r1} is a repulsive force and F_{f1} is a friction force between Tip I and the nanoobjects. The force is obtained in the same way of section 2.1.3, the main difference is the adhesion force F_{a1}. For the micro manipulation application, this force exist but is very small compared to the others because the diameter of the tip is very small compared to the size of the object to manipulate. For nanomanipulatio, it is not the case, and the adhesion force needs to be considered. The F_{f1} includes friction μF_{r1} contributed from the repulsive force and the shear force F_s. These two parts can be simplified as $\mu' F_{r1}$, here μ' is a friction coefficient. In the actual use, a clamping angle 40°

and a normal $\mu' = 0.3$ are used [VEH03]. The resultant adhesion force or grasping force can be obtained as follows:

$$F_{ao} = F_{z1} + F_{z2} = (\beta_1 \cdot \Delta V_1 + \beta_2 \cdot \Delta V_2) - (F_{a1} + F_{a2}) \tag{2.5}$$

where β_2 and ΔV_2 are respectively the normal force sensitivity and the voltage response of the photodiode on Tip II, F_{a1} and F_{a2} are typically the pull-off forces on each tip.

2.2.4 Pick-and-place of silicon nanowires

2.2.4.1 Task description

In experiments, silicon nanowires (SiNWs) were deposited on a freshly cleaned silicon wafer coated with 300 nm silicon dioxide. A pre-scanned image (8 μm x 8 μm) is shown in Fig. 2.11, which includes the topographic image of SiNWs, and the local image of tip II (see the zoomed inset). A grasping location on the left SiNW is marked A-A, where the SiNW has a height of 153 nm. The left SiNW will be transported to the target position and released onto the right SiNW to build a nano crossbar.

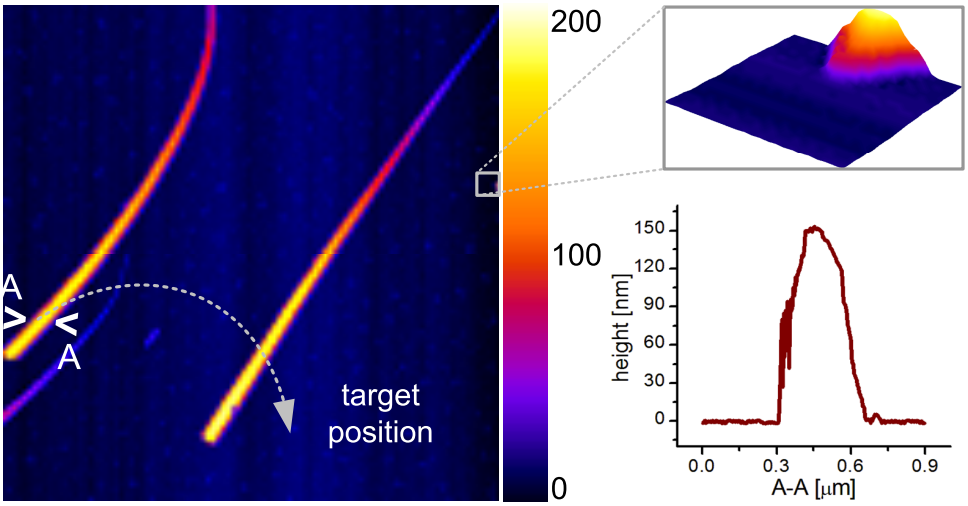

Figure 2.11 - *Pre-scanned image of the SiNW. Insets show a 3D topographic image of the tip II and the nanowire at location A-A.*

2.2.4.2 Contact detection

Fig. 2.12 shows an example of contact detection with tip II: Seen as icons in the graph, the tip starts to dig into the root of the SiNW as the tip makes contact with the SiNW. Further movement leads to pushing the SiNW without any obvious change in the voltage output. During retraction, after contact with the substrate breaks, the bending force sharply reaches a positive peak with a similar response to that of the approach. Eventually, the tip pulls off the SiNW and reaches zero. When the tip digs into the SiNW, the cantilever produces a pre-grasping force $\Delta F = 28nN$ with a voltage difference of about 20 mV. The corresponding preload on the tip II is estimated as $F_{p2} \approx 26nN$ using Eq. 2.4.

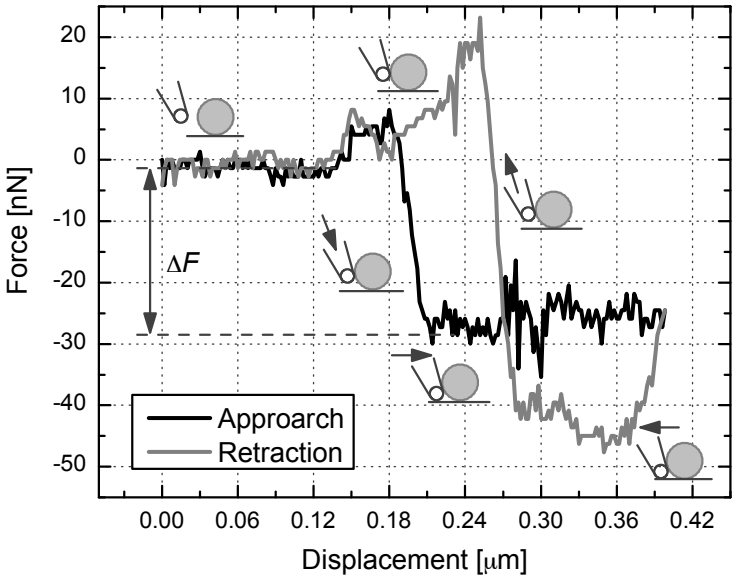

Figure 2.12 - *Contact detection by normal force sensing on Tip II*

2.2.4.3 Pick-and-place force sensing

Fig. 2.13 shows the curve of the peeling force spectroscopy on Tip II during the pick-and-place manipulation of the same SiNW. The curve starts from contact state between the nanotweezer, the SiNW and the substrate. As the gripper is moved up to pick up the SiNW, the cantilever is bent downwards creating negative forces until the cantilever pulls off the substrate with a voltage difference of 75 mV indicating a pull-off force $\Delta F_1 = 102nN$. As the gripper is moved up further, the force magnitude gradually keeps increasing with the SiNW peeling force responses. Retraction

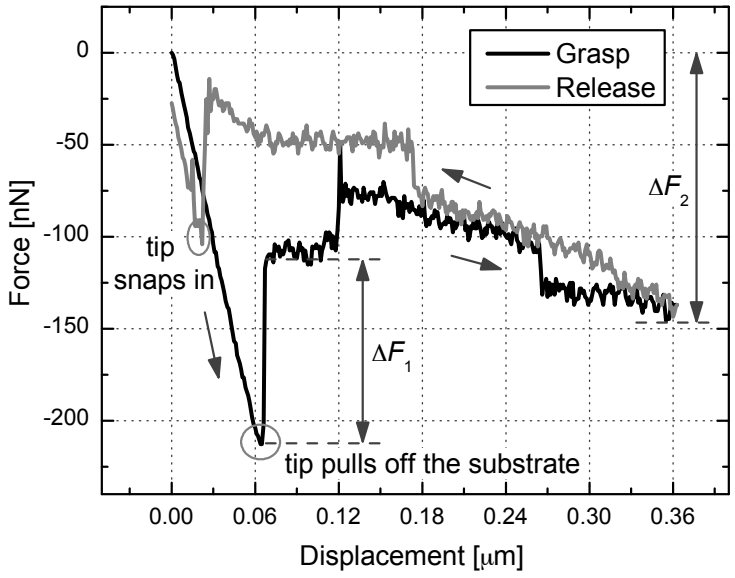

Figure 2.13 - *Force detection on Tip II during the grasp and release operation*

leads to a continuous decrease except for a weak fluctuation at 178 nm. Snap-in occurs at 25 nm after a mild force decrease. With even further retraction, the magnitude of the normal force of Tip II approaches the prior state before grasping.

During pickup, the maximum SiNW peeling force occurs at retraction start, where the voltage is about -105 mV indicating a grasping force of $\Delta F_2 = 144nN$. At this point, from calculation, $F_f \approx 31nN$ that is much smaller than the SiNW-substrate adhesion force, and $F \approx 218nN$ that generates a maximum contact stress $p_0 = 7.1Gpa$ with $R \approx 19.5nm$ at the contact location of 55 nm from the tip end. Fortunately, this contact stress is still below the yield stress of the silicon at the nanoscale (around $12 \sim 13$ GPa at the nanoscale) due to size effects on the hardness.

2.2.4.4 Build a nanowire crossbar

The post-manipulation image in Fig. 2.14 verifies that the SiNW has been successfully transported and piled on another SiNW, building a nanocross-bar with a maximum height about 500 nm. During the pick- and-place manipulation, once the SiNW was reliably grasped, the gripper moved up 800 nm at a velocity of 80 nm/s, then the SiNW was transported a distance of 4.05 μm on the X-axis at a velocity of 150 nm/s and 1.95 μm on the Y-axis at a velocity of 72 nm/s.

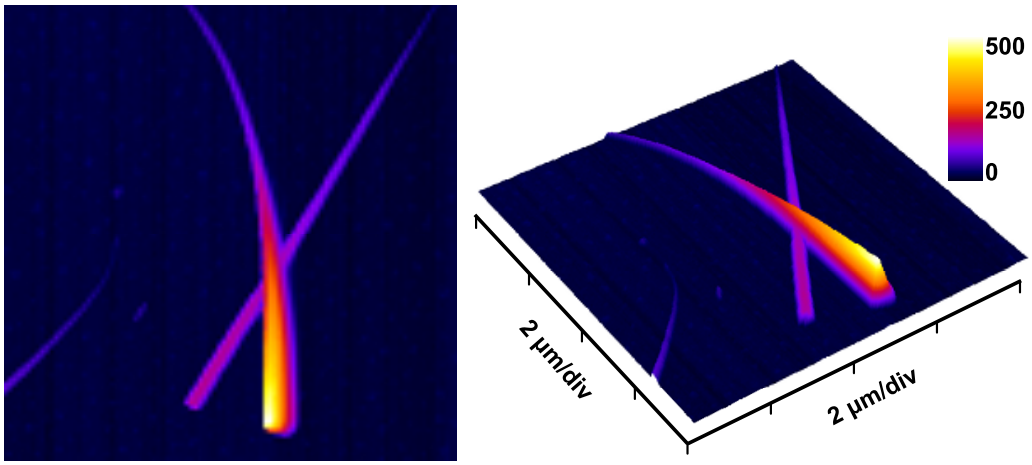

(a) (b)

Figure 2.14 - *Pick-and-place manipulation results for the SiNWs. (a) A post-manipulation image verifies that the manipulated SiNW is piled on another SiNW. (b) 3D topographic image of the manipulation result.*

2.3 Conclusions

It is well known that the pick-and-place micromanipulation is a great challenge for microobjects with feature sizes less than 10 μm, especially for the manipulation confined in air. Fortunately, the system has achieved this type of pick-and-place micromanipulation with a nanotip gripper constructed by two AFM cantilevers. In order to validate the manipulation ability of the system, microspheres with diameter less than 4 μm were manipulated and as a result, five micropyramids have been built. The system has made the 3D micromanipulation and microassembly at several micrometers in air feasible.

Additionally, the system has been used for nanomanipulation. Modifications on the kinematical configuration of the system allowed to make nanocrosses with SiNWs. With the built nanotweezer of the system, one side of the nanowire where the diameter was 153 nm was picked and placed on top of another nanowire. The main limitations of this system are however , the speed of the scanning as well as the dexterity of the arm. In fact when the cantilever moves, the laser and photodiode remains fixed uncalibrating the system, thus reducing the displacement of the arm to a small range.

To improve the system, the replacement of one of the cantilevers of the system

by a dynamic force sensor has been decided. In the following, a study on dynamic oscillators is made. An application on nanocharacterisation is done in order to allow better understanding of the sensor working mode.

Chapter 3

Dynamic force self sensing: the tuning fork

Contents

In the chapter 2, a two tip atomic force microscope has been developed. Initially, it was used for pick and place micromanipulation with force feedback. In this case, two layer micropyramids were made by pick and place of nylon microspheres of 3 μm $\sim$ 4 μm diameter. For raw position of the microspheres, the optical microscope was used. For grasping point localization, local AFM scanning with tapping mode was used. Then a microgripper was formed with the two tips for pick and place with force feedback. For this application, the dexterity of the arms was a problem, constant recalibration of the photodiodes was necessary, slowing the manipulation process and reducing the precision, this, because the photodiode and laser didn't moved with the cantilever. After, an application of the system for SiNW nanocrosses fabrication was presented. They were made with SiNW of diameters as low as 80nm. At this scale, optical imaging is not possible, and so, the entire manipulation process relied on the AFM images. These images were done with a classical cantilever working in tapping mode. This technique is invasive with the substrate, and will cause damage to the tip over time. In consequence, a new type of force sensor needs to be used to address, the dexterity of the arm, the speed of force sensing, and the level of interaction with the substrate.

In order to solve these issues, the high speed force sensing techniques need to be studied as well as dynamic force sensors with embedded measuring. This chapter represents a study of a classical dynamic force sensor, the quartz tuning fork. An application of these force feedback techniques on mechanical characterization of ultraflexible nanostructures is presented.

This chapter is divided into three parts. First, a study of the influence of the tip attached to the sensor for quantitative force measurement is presented. Then, in the second part, to validate the dynamic force sensing capabilities, we aim to develop a 3D nanomechanical property characterization system with large range and high resolution force sensing. The 3D characterization based on the developed sensor is achieved with an SEM for an accurate visual detection and a nanomanipulation system with 3 degrees of freedom and nanometer positioning resolution. The large range and dynamic force sensing of the proposed system is proved by a full range tensile elongation study of HNB. In this case, the tuning fork is fixed. Finally, the dexterity of the sensor is proven by the surface characterization of membranes with a moving sensor.

3.1 Quantitative force mesurement

3.1.1 Model Comparison

The aim of this section is to analyze the differences between the three different models from chapter 1 (Eq. 1.14). When the dynamic sensor is used in frequency modulation, the measured variable is the frequency shift. With these models it can be transformed into stiffness for force gradient sensing:

$$\begin{cases} \Delta k = \frac{2k\Delta f}{f_0} & Singlecantilever \\ \Delta k = \frac{4(k+2k_c)\Delta f}{f_0} & Castellanos \\ \Delta k = \gamma - \frac{k_c^2}{\gamma} & Generalmodel \end{cases}$$

where $\gamma = \left(\frac{\Delta f}{f_o} + 1\right)^2 (k + 2k_c) - k - k_c,\ f_1.$

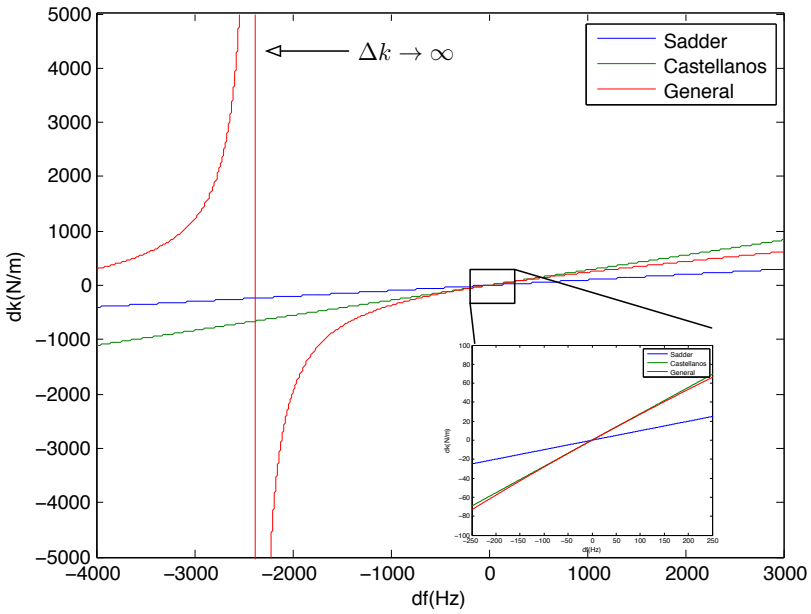

Figure 3.1 - *Tuning fork frequency modulation models plot for comparison . $k = 1634N/m$, $k_c = 318N/m$ and $f_0 = 32766Hz$*

To see the differences between the three models, a plot of Δk versus the frequency shift for the 32 kHz tuning fork used by Castellanos in [CAR09] is done for a wide range frequency shifts (Fig. 3.1). This shows that the model of a simple cantilever (Sadder in plot) can never be used on a tuning fork with two free prongs.

The general model shows a highly non linear behavior with a discontinuity. At this point $\Delta k \to \infty$. From mechanical point of view this means that the prong is blocked from movement. However, this model is based on the assumption that the tuning fork is mass balanced witch means that this is valid for non-contact gradient forces or contact forces with a low mass change compared to the stiffness:

$$\frac{\Delta m}{m} < \frac{\Delta k}{k} \tag{3.1}$$

Even if Castellanos model supposes $\Delta k << k$, it is still valid for frequency shifts smaller than 200 Hz or stiffness shift of less than 80 N/m. In summary:

- The single cantilever based on Sadders equation should only be used if the tuning fork has one of the two prongs blocked. This configuration is called Qplus.
- The two prong model with a coupling stiffness of Castellanos should be used only for small range.
- For full range, the general equation of previous model can be used if the mass of the sensor is not changing.

3.1.2 Tip influence on force measurement

The adhesion of a tip to one of the prongs of the tuning fork poses several problems. The first of them is the unbalancing of the masses of the tuning decreasing the quality factor. This can be easily fixed by adding/removing mass to the other prong of the tuning fork for mass compensation till the highest quality factor is obtained. The main problem however for quantitative force measurement is the stiffness of the tip. In the bibliography, the last subject has not been taking into account. In this section, a model of the tuning fork with tip is presented as well as an analysis of the influence of the value in the overall measurement.

3.1.2.1 Tip attached perpendicular to the tuning fork

When the tip is attached perpendicular to the prong of the tuning fork (Fig. 3.2.(b)), only the longitudinal stiffness of the tip needs to be considered (Fig. 3.2.(a)).

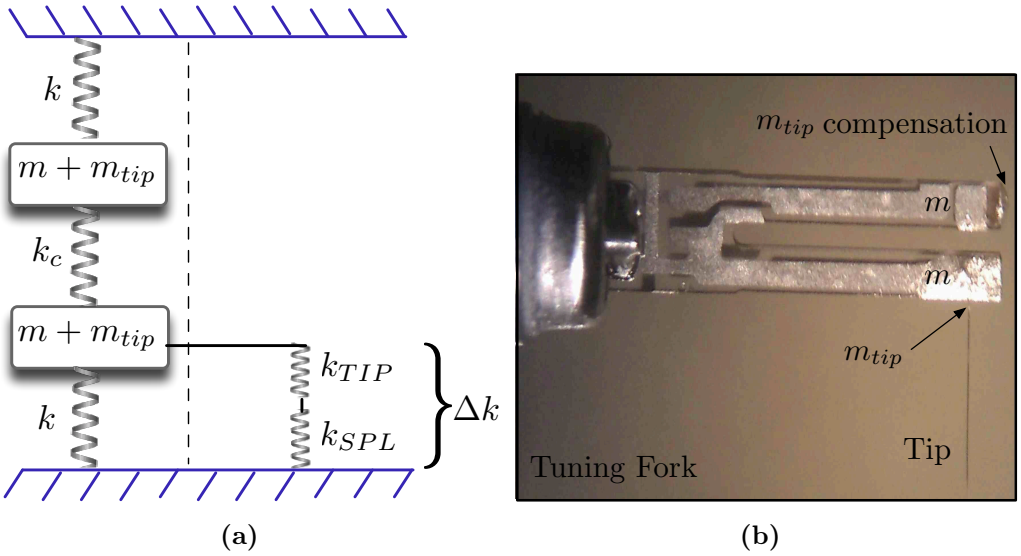

Figure 3.2 - *Tuning fork with tip. (a) Schematic diagram of tuning fork coupled oscillators with tip in contact with a spring. To avoid mass unbalancing of the tuning fork, a mass is added to the other prong. (b) Photo of a tuning fork with a tip attached perpendicular to the prong.*

The measured stiffness Δk will be a composition of the stiffness of the sample k_{SPL} and the stiffness k_{TIP} of the tip:

$$\Delta_k = \frac{1}{\frac{1}{k_{SPL}} + \frac{1}{k_{TIP}}} \tag{3.2}$$

From last equation, the smallest of k_{SPL} and k_{tip} will be predominant for the resultant Δk. In consequence, if $k_{tip} >> k_{SPL}$, the stiffness of the tuning fork tip will not influence the frequency shift of the tuning fork an thus the gradient force measurement. Still, the measured stiffness can be high enough to consider the stiffness of the tip. Or, the stiffness of the tip can be very low due to its length and angle with respect to the tuning fork prong, due the necessity of measuring it. Furthermore, for biological samples, it is very important to know the contact stiffness of the tuning fork to avoid sample damage:

$$k_{TFcontact} = \frac{1}{\frac{1}{k_{TFeff}} + \frac{1}{k_{tip}}} \tag{3.3}$$

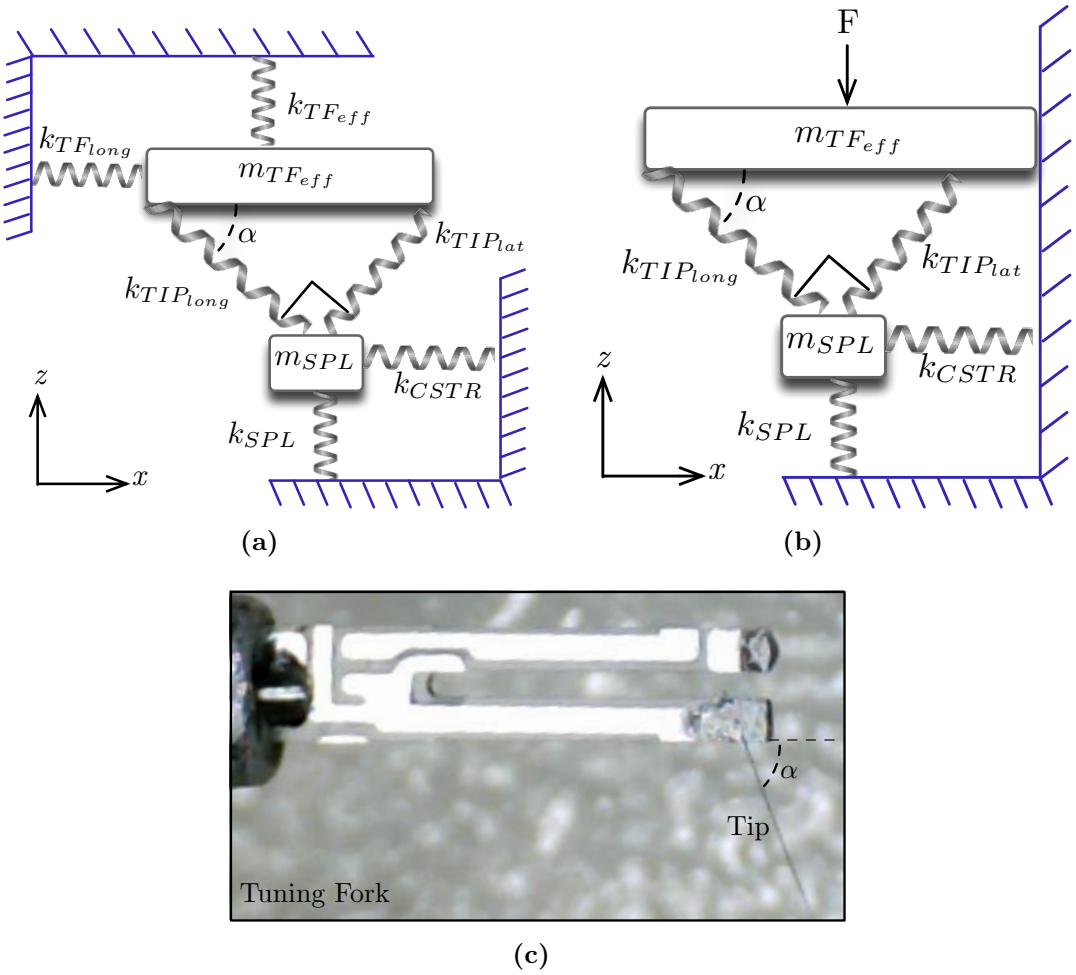

Figure 3.3 - *Two dimensional mechanical model of TF with tip. (a) Initial diagram. (b) Diagram after simplification. (c) Photo of the TF with a tip attached with an angle.*

3.1.2.2 Tip attached with an angle

Sometimes a tip needs to be attached to the tuning fork with an angle α to be able to see it from an optical microscope. If it is the case, a two dimensional analysis of the spring system need to be done (Fig. 3.3.a) were the tip lateral stiffness $k_{TIP_{lat}}$ and the lateral constraint stiffness of the contact point k_{CSTR} are considered. The longitudinal stiffness of the tuning fork prong $k_{TF_{long}}$ being very high, can be neglected, in consequence, the movement of the prong in the x axis is assumed zero. The resulting model is Fig. 3.3.b. For this model, the displacement of the tuning fork in z axis is dz_{TF} and the displacements of the sample in z and x axis are dz_{SPL} and dx_{SPL}.

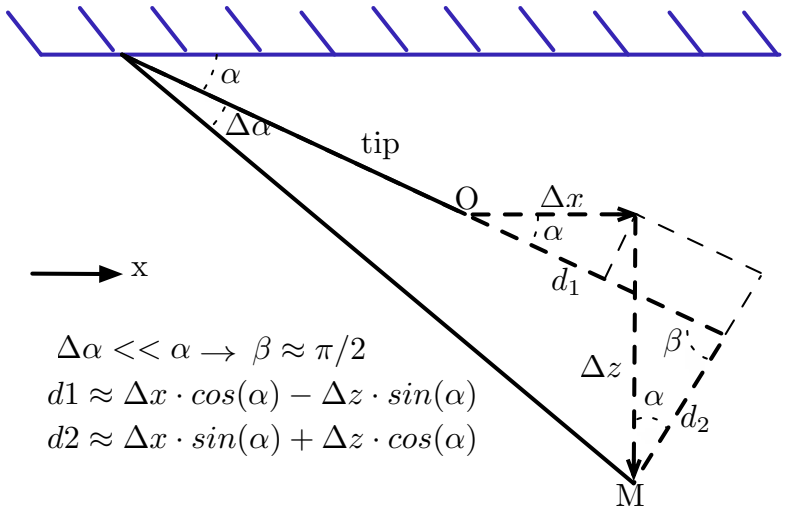

Figure 3.4 - *Diagram of the 2D displacement of the tip with an angle*

The elastic potential energy of the system U is obtained:

$$U = U_{TIP_{long}} + U_{TIP_{lat}} + U_{SPL} + U_{CSTR} \tag{3.4}$$

It is a composition of the elastic potential energy of the longitudinal and lateral spring of the tip $U_{TIP_{long}}$ and $U_{TIP_{lat}}$, of the spring of the sample U_{SPL} and the horizontal constraint spring U_{CSTR} due to tip sample contact. Each of these energies can be estimated as follow with Fig. 3.4 :

$$\begin{cases} U_{TIP_{long}} = \frac{1}{2} \cdot k_{TIP_{long}} \cdot (cos(\alpha) \cdot dx_{SPL} - sin(\alpha) \cdot (dz_{TF} - dz_{SPL}))^2 \\ U_{TIP_{lat}} = \frac{1}{2} \cdot k_{TIP_{lat}} \cdot (sin(\alpha) \cdot dx_{SPL} + cos(\alpha) \cdot (dz_{TF} - dz_{SPL}))^2 \\ U_{SPL} = \frac{1}{2} \cdot k_{SPL} \cdot (dz_{SPL})^2 \\ U_{CSTR} = \frac{1}{2} \cdot k_{CSTR} \cdot (dx_{SPL})^2 \end{cases} \tag{3.5}$$

Solving Lagrange equations for the previous system:

$$\begin{bmatrix} c & a & -a \\ a & b + k_{SPL} & -b \\ -a & -b & b \end{bmatrix} \cdot \begin{bmatrix} dx_{SPL} \\ dz_{SPL} \\ dz_{TF} \end{bmatrix} = \begin{bmatrix} 0 \\ 0 \\ F \end{bmatrix} \tag{3.6}$$

where:

$$\begin{cases} a = (k_{TIP_{lat}} - k_{TIP_{long}}) \cdot cos(\alpha) \cdot sin(\alpha) \\ b = k_{TIP_{long}} \cdot sin(alpha)^2 + k_{TIP_{lat}} \cdot cos(alpha)^2 \\ c = k_{TIP_{long}} \cdot cos(alpha)^2 + k_{TIP_{lat}} \cdot sin(alpha)^2 + k_{CSTR} \end{cases} \tag{3.7}$$

Several things can be seen from the system solution. No mater what the tip angle, the tip lateral stiffness, or the sample constraint value are, the force applied to the substrate in z-axis, is the same force applied to the tuning fork in the Z-axis: $F = k_{SPL} \cdot dz_{SPL}$. Additionally, the stiffness in z-axis between the prong and the ground is different from k_{SPL} and highly dependent on α, $k_{TIP_{lat}}$ and k_{CSTR}.

For quantitative force gradient measurement with frequency modulation there are two options. For the first, α, $k_{TIP_{lat}}$ and k_{CSTR} need to be measured with precision. A geometric model could be used to estimate $k_{TIP_{lat}}$ or measure it with another tuning fork. However, to measure k_{CSTR} with precision is almost impossible as it depends on the contact. The other option consist in driving $(dz_{TF} - dz_{SPL})$ near zero. For this, only the order of magnitude of $k_{TIP_{lat}}$ and k_{CSTR} are needed and should be as high as possible compared to k_{SPL}, this way $\Delta k \approx k_{SPL}$.

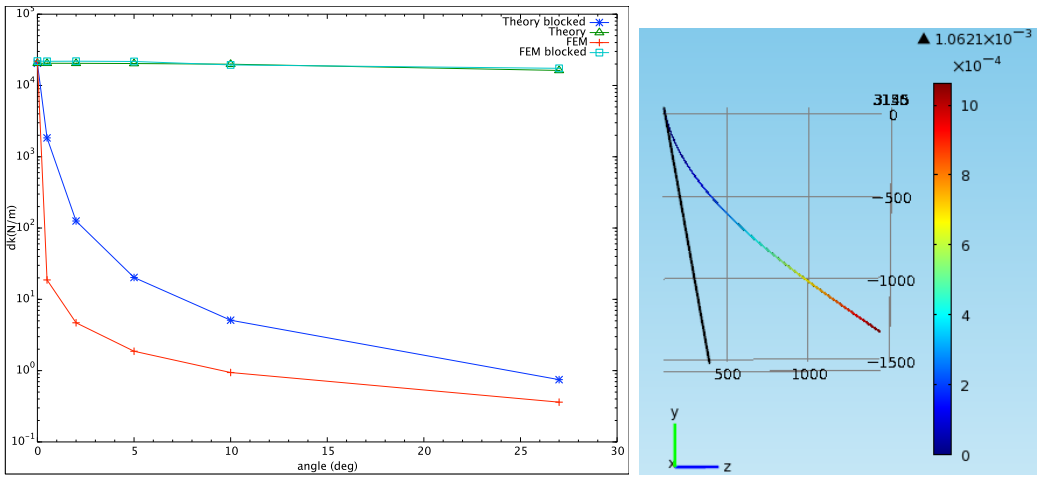

(a) **(b)**

Figure 3.5 - *Influence of the angle of the tip attached to the TF. (a) Angle effect on the stiffness on Z-axis for a 10 µm diameter and 1.576mm length tungsten tip, theory is compared to FEM (b) FEM simulation for non-blocked tip with a 10 deg angle*

As an example for illustrating the influence of each of these parameters, FEM (finite elements simulations) were done (Fig. 3.5.(b)). For these simulations, a force was applied to a tip of 10μm of diameter in z axis. Two sets of simulations were done, for the first, the constraint stiffness k_{CTSR} was imposed to the system with a very high value. For the second, this value was driven to zero. In all the cases, the angle α was changed several times and the stiffness in z-axis of the tip $k_{TF_{eff}}$ is deduced from the displacement and applied force Results are gathered in Fig. 3.5.(a)

with the theoretical results from Eq. 1.14 . The same tendency is observed for both theory and FEM. When tip is blocked in x-axis with a high constraint stiffness, the angle does not affect the measurement. However, on the opposite case, the vertical stiffness $k_{TF_{eff}}$ is highly dependent on the angle of the tip. For quantitative gradient force measurement, the stiffness of the sample should be under the curve.

In the following, an application of quantitative force measurement with dynamic force sensors is presented. A robotic manipulation setup under SEM based on tuning forks is developed for mechanical characterization of nanostructures.

3.2 Dynamic force sensing with fixed tuning fork

3.2.1 System overview

An in situ SEM tuning fork mechanical property characterization system is presented. An OC4-Station from SPECS-Nanonis is used for the oscillation control of

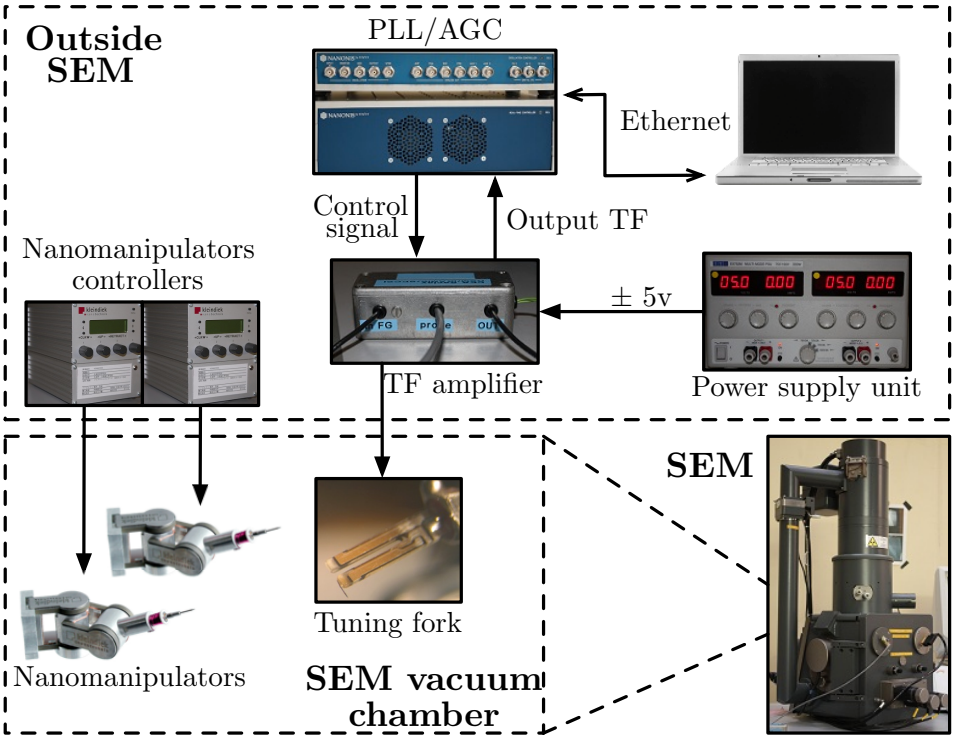

Figure 3.6 - *System configuration of used hardware inside and outside the SEM.*

the tuning fork and data acquisition. The advantages of this station are namely that it has a lock-in amplifier, a PLL, an AGC, a data acquisition hardware and software, and a real time operating system. The electronic preamplifier for the tuning fork was specially designed for use in SEM imaging conditions. The electronics were provided and patented by Jérôme Polesel Maris of the CEA SACLAY, DSM/IRAMIS/SPCSI [Jé]. A TT*i* EX752M multi-mode power supply unit was used with fixed +/-5v for the tuning fork electronic preamplifier. The detailed experimental setup is shown in Fig. 3.6. The main advantage of this system is that all the electronics for the tuning fork and the manipulators are outside the SEM chamber, thus avoiding any influences from the electron beam and space occupation.

For vacuum environment and visual feedback, an SEM (Leica stereoscan 260 cambridge instruments) is used. Two nanomanipulators (MM3A-EM, Kleindiek) are used to manipulate the nanostructures. Further details on the role of the manipulators and the manipulation procedure are described in section 3.2.4. Each nanomanipulator has 3 degrees of freedom and respectively 5nm, 3.5nm and 0.25nm resolution at the tip in X, Y and Z axis. Each axis is actuated with piezo stick-slip principle and is controlled via an open loop piezo controller. Configuration of the manipulators and the tuning fork inside the SEM chamber can be seen in Fig. 3.7.

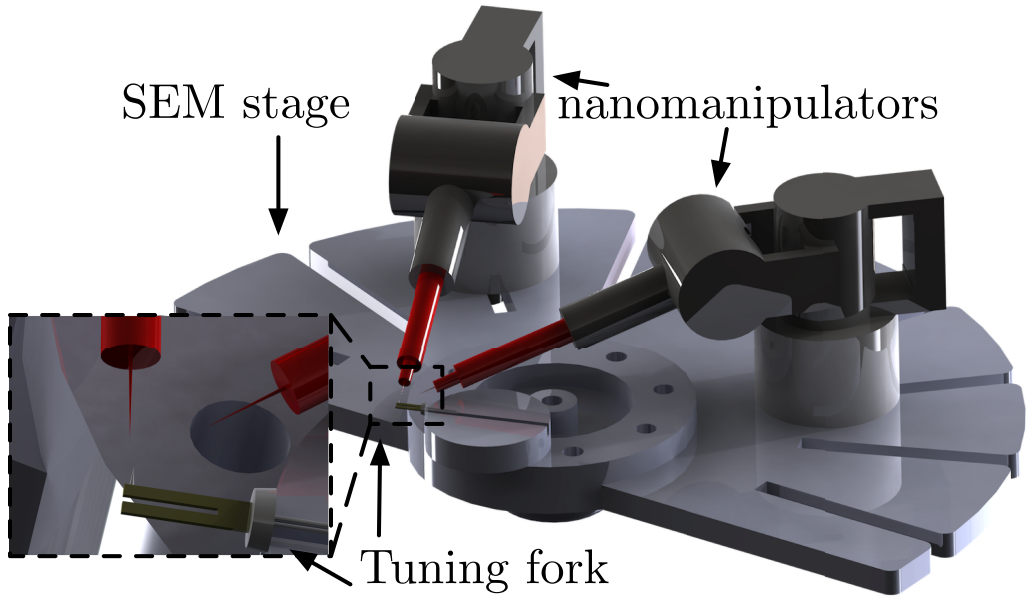

Figure 3.7 - *3D CAD model of experimental setup of nanomanipulators and tuning fork inside SEM chamber.*

The tuning forks were manufactured by Citizen America - CFS206 32.768KDZB-UB. A tip is attached to the tuning fork in order to fix it to the nanostructure. Picoprobes, tungsten tips (T-4-10-1 mm, tip radius: 100 nm, GGB industries) and tips made with platinum iridium Pt90/ir10 wires are used for the nanomanipulator and the tuning fork respectively.

3.2.2 Tuning fork probe preparation

Several factors have to be considered before adding the tip. The quality factor of the tuning fork should remain as high as possible in order to obtain the highest sensitivity. It is based on balancing the weight between the two prongs. Any weight added to one of the prongs should be compensated by the other one so as to avoid decreasing the quality factor [CAR09]. As shown in Fig 3.8, for grounding with the prong of the tuning fork, electrically conductive silver epoxy EPO-TEK H21D (Epoxy Technology) is used to fix the tip, thus avoiding electrostatic charging by electron beam inside the SEM. Glue also needs to be added for weight compensation on the other prong of the tuning fork; this can be done with either conductive or non conductive glue. As the electron beam is mainly focused and zoomed on the tip of the probe, the other prong of the tuning fork has little risk of charging.

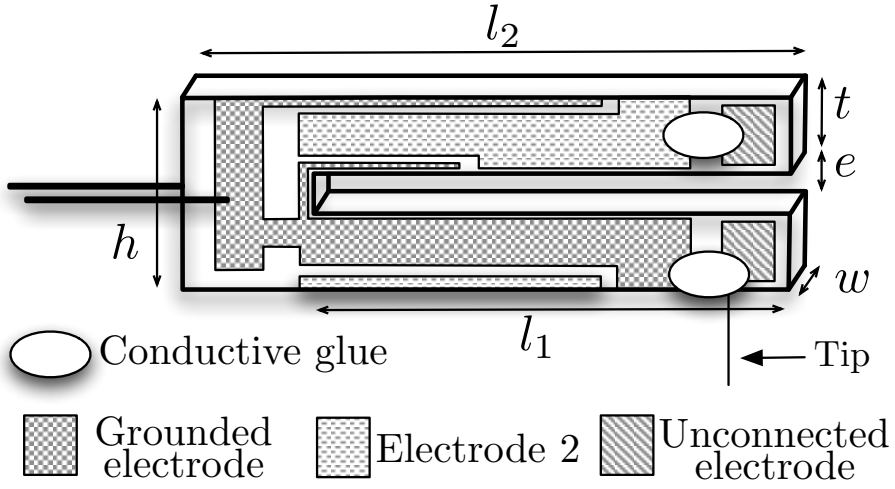

Figure 3.8 - *Schematic of Tuning Fork electrodes with glued probe.*

3.2.3 Data flow

The data flow of the entire experiment (Fig. 3.9) can be divided into 3 different and independent flows. The first is the nanomanipulator flow. It is composed of both manipulators and their respective controllers for the piezoactuators. They are manually operated and are not connected to the rest of the setup. The second data flow represents all the hardware and software used for controlling the tuning fork. A PLL and an amplitude controller are needed to obtain the frequency shift. This frequency is acquired with labview based acquisition software and after the experiment is finished, it is transformed into the stiffness (under the assumption of the constant stiffness of the tuning fork [CAR09]) and the constraint force of the measured object is obtained applying Hooke's law to Eq. 1.14. The last block represents the SEM based visual feedback. Analog video signal from the SEM is imported with a data acquisition card and recorded. Once the experiment is finished, the visual detection is used to estimate the nanostructure elongation. Hence, the elongation measurement and the stiffness estimation of the nanostructure gives the applied force of the nanostructure.

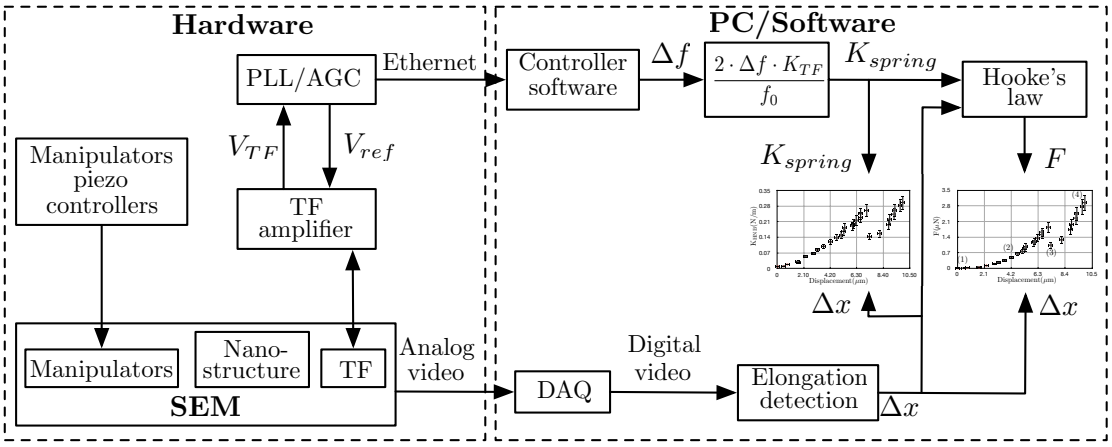

Figure 3.9 - *Experiment's data flow for plot generation. The tuning fork frequency shift obtained thanks to the PLL and AGC turned on, is then transformed to stiffness with Eq. 1.14, which is transformed to force with Hooke's law. SEM video feedback is imported to a computer with a data acquisition card. The elongation of the nanostructure is measured from video acquisition.*

3.2.4 Manipulation protocol

3.2.4.1 Assembly of nanostructure with manipulation setup

The tuning fork probe was fixed to the top of the SEM stage to avoid mechanical disturbances. In order to pick up the nanostructure, the free end of the nanostructure is attached to the tip of the manipulator. For this purpose, the probe of the manipulator is dipped into Nanopoxy glue (Fig. 3.10.(a), then it is brought closer to make contact with the end of the nanostructure (Fig. 3.10.(b). The SEM electron beam is focused onto the glue to solidify it.

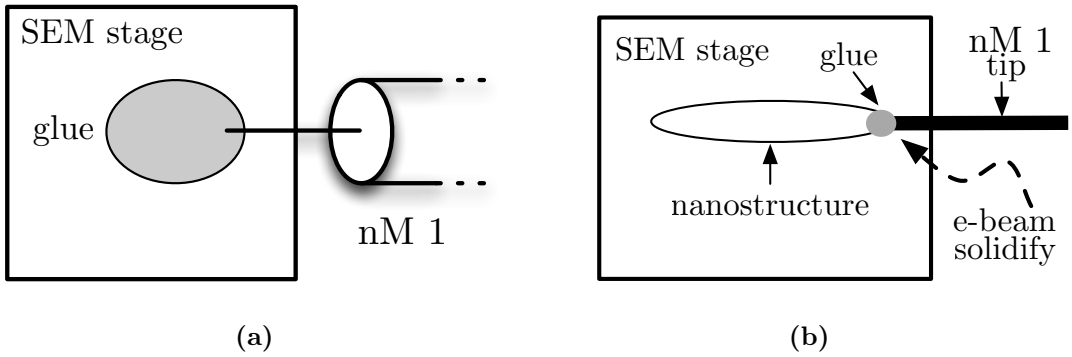

Figure 3.10 - *Protocol for picking the nanostructure with manipulator tip. (a) Adding glue to the probe of the nanomanipulator. (b) Picking nanostructure from subtract with the nanomanipulator probe and soldering with e-beam. nM stands for nanomanipulator*

Two different attachments to the tip of the tuning fork and the nanostructure can be made. The first technique involves fixing the nanostructure with glue to the tip of the tuning fork. For this, glue is added to the tip of the tuning fork with the second nanomanipulator (Fig. 3.11).(a). The nanostructure is then brought closer to nanomanipulator 1 to make contact with the tip of the tuning fork. The SEM electron beam is used to solidify the glue (Fig. 3.11.(b). This technique allows full range characterization of the nanostructure, however, the nanostructure has to be destroyed eventually in order to disconnect the system. For the second experiment, electrostatic and van der Waals forces are used to maintain the nanostructure attached to the probe of the tuning fork. This is basically the same configuration except for the absence of applying chemical glue between the tuning fork probe and the nanostructure. What is more, it is a non destructive technique and can be repeated several times.

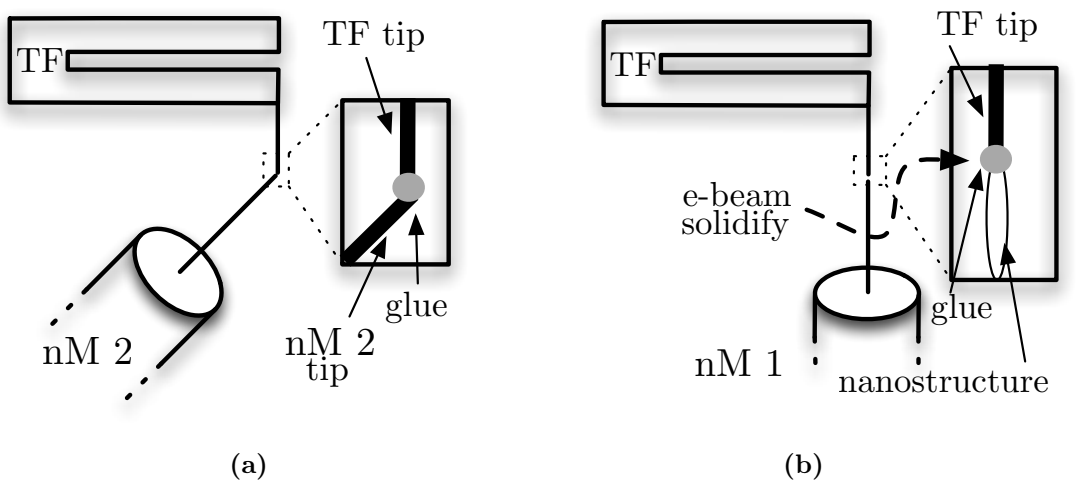

Figure 3.11 - *Attachment with glue of the nanostructure to the tuning fork tip. (a) Adding glue to tip end of the tuning fork probe (b) Attaching the nanostructure to the tuning fork tip and soldering with the electron beam.*

3.2.4.2 Experiment protocol

Usually, the lateral stiffnesses of ultra flexible nanostructures like CNTs and HNBs are smaller than longitudinal ones by at least one order of magnitude. As a result,

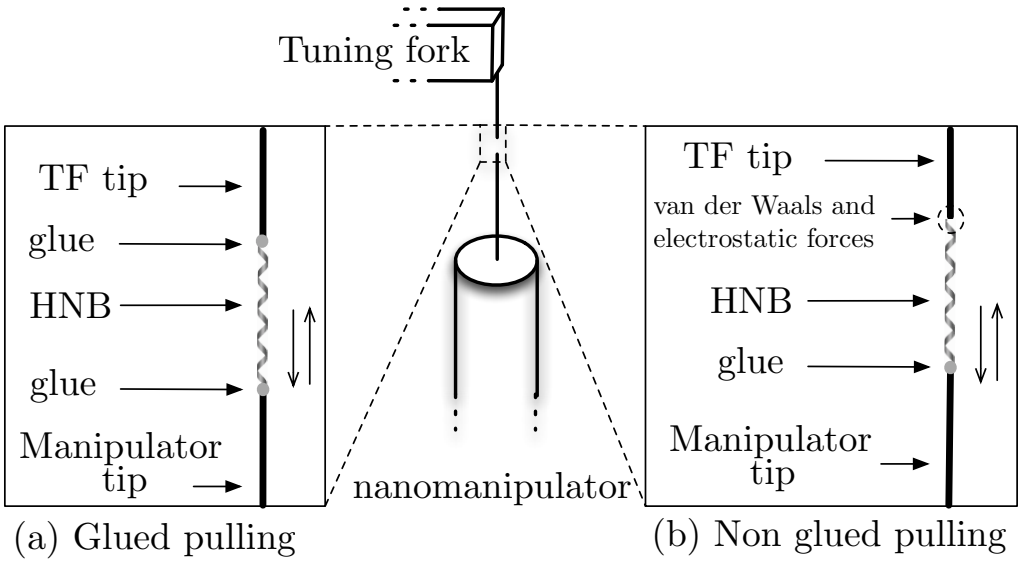

Figure 3.12 - *Experimental protocol and configurations for longitudinal pulling. (a) nanostructure glued to the tip of tuning fork (b) nanostructure partially attached to the tip of tuning fork using adhesion forces.*

compressing the structure is very challenging; it might bend instead of compress. For this reason, the experimental protocol is focused on elongation of the nanostructure.

For the attachment with glue (Fig. 3.12.a), the bond with glue is stronger than the mechanical resistance of the nanostructure. This guarantees that the nanostructure will break before the glue, and so full range characterization, can be achieved. For the second type of elongation (Fig. 3.12.b), adhesion forces are used to maintain the bond between the nanostructure and the tip of the tuning fork. This bond depends mainly on the electrostatic force and depending on the dimensions and conductivity of the nanostructure, it could be higher or lower. Furthermore, this force can be increased by the SEM electron beam voltage and focusing it on the structure. At certain points during the elongation, the structure can be detached and the experiment can be repeated again.

3.2.5 Helical nanobelt characterization

InGaAs/GaAs bilayer HNBs were used for the experiments. The HNBs were fabricated by the process described in [HH09]. Finite element method (FEM) simulation is used to estimate the deflection by the applied force onto HNBs, thus, obtaining the rest (at no elongation) stiffness. Longitudinal stiffness is estimated to be 0.009 N/m for HNB 1 and 0.011 N/m for HNB 2 as summarized in Table 3.1.

Table 3.1 - *HNB specifications*

	HNB 1	HNB 2
Thickness of InGaAs/GaAs (nm)	11.6/15.6	11.6/15.6
Length (μm)	25.4	53.4
Pitch (μm)	3.9	8.9
Number of turns	6.5	6
Stripe width (μm)	1.5	2.5
Diameter (μm)	2	2.5
Longitudinal Stiffness (FEM)(N/m)	0.009	0.011

This simulation demonstrates the rest position stiffness of the HNB. Nevertheless, non-constant behavior of the stiffness for upper elongation range was demonstrated by previous experimental works [BDN$^+$06] with an AFM cantilever under SEM. However, in previous works, full range measurement was not attempted due to the lack of wide range force sensing.

Two tuning fork probes were used for the experiments. The geometry information and the estimated stiffness of the two tuning forks are summarized in Table 3.2.

Table 3.2 - *Tuning forks specifications with glued tip at the end of the prong*

	TF 1	TF 2
Resonant frequency $f_0(Hz)$	28325.5	30895.2
Stiffness $k_{TF}(N/m)$	7936	7936
Quality factor	11145	19800
Prong length $l_1(\mu m)$	3204	3204
Prong height $t(\mu m)$	382	382
Prong width $w(\mu m)$	238	238

3.2.5.1 Full range mechanical characterization of HNB

For this experiment, the HNB 1 was attached between the tuning fork tip and manipulator tip with glue for full range characterization. With the method described in section 3.2.3, frequency shift (Fig. 3.13.a), the elongation of the HNB (Fig. 3.13.b)), the HNB stiffness Fig. 3.13.c) and the constraint force of the HNB Fig. 3.13.d) were obtained. The frequency shift noise (estimated at $5mHz$) is much lower than the frequency shift steps due to the elongation of the HNB. As the manipulators have no position feedback, the displacements are estimated from the SEM recorded video at 33 Hz frame rate with a resolution of $0.2\mu m$ for each measurement. Details on error estimation for frequency shift and force are summarized in appendix A.

During the motion of the nanomanipulator, different geometrical configurations of the HNB stand out: these are compiled in Fig. 3.13.e. At the beginning of the experiment, the HNB is in rest position and the pitch looks homogeneous (Fig. 3.13.e.1). The stiffness of the HNB for this position was obtained with finite element simulation. To obtain the experimental stiffness of the HNB for the rest position, the difference between the tuning fork resonant frequency before and after the HNB attachment to the tuning fork tip needs to be obtained. However, one of the main problems for this measurement was that the vacuum condition of the SEM improved over time, thus making the resonant frequency increase continuously. The order of magnitude of the frequency shift due to this is in a similar range to the frequency shift due to HNB attachment. In consequence, the initial stiffness could not be

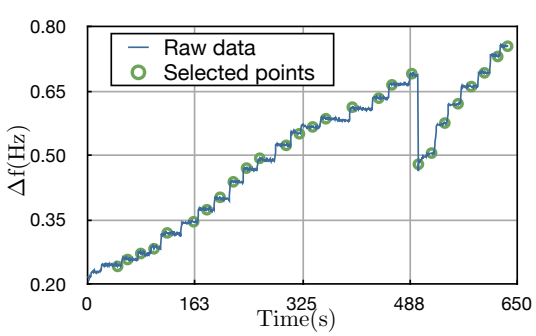

(a) *Frequency shift from PLL and amplitude controller*

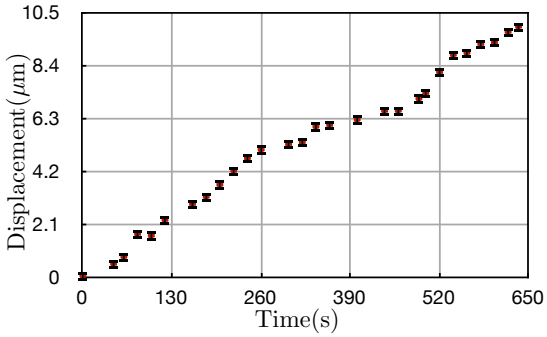

(b) *Displacement from SEM visual feedback*

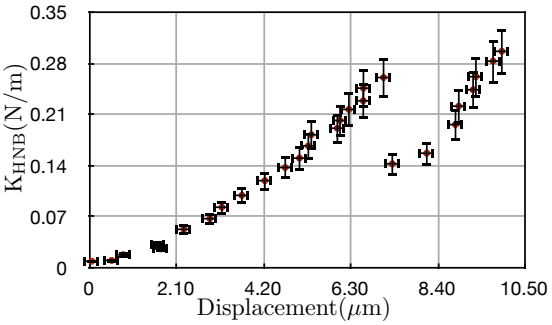

(c) *HNB longitudinal stiffness.*

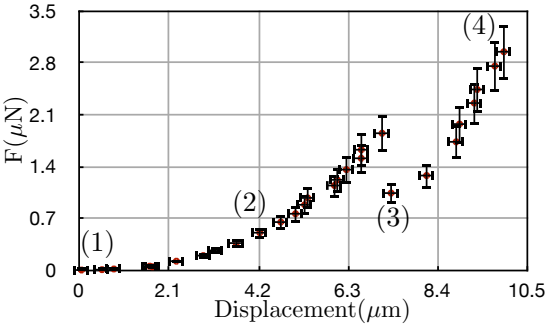

(d) *Force.*

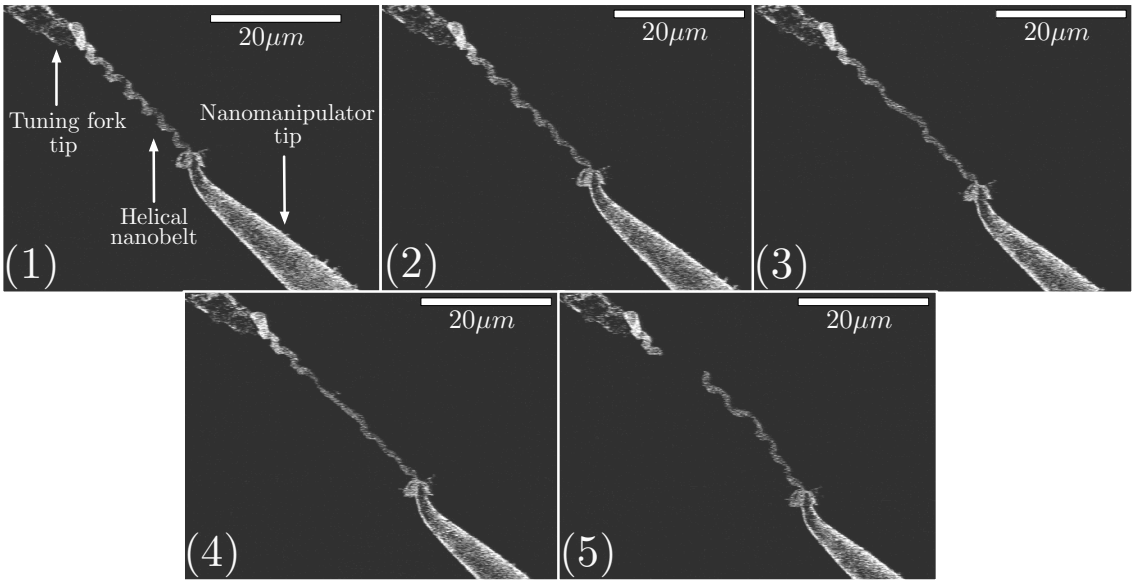

(e) *Captures from SEM video*

Figure 3.13 - *Full range longitudinal pulling. (1) HNB prior to pulling, (2) HNB during pulling, (3) HNB unrolling, (4) HNB before break, (5) HNB after break. Details on error estimation are gathered in appendix A*

measured and so, it was estimated by FEM. It should be noted that the initial stiffness model by FEM for rest stiffness was confirmed by experiments [BDN+06].

With elongation (Fig. 3.13.e.2), the HNB shows a non homogeneous pitch. This is due to the rotation constraint imposed by attaching glue to both sides. Further elongation increases the pitch differences in the HNB untill one part of the HNB unrolls at $7.3\mu m$ displacement at 500 seconds (Fig. 3.13.e.3). Subsequently, there is a release of the strain in the HNB that is reflected in a drop of the frequency shift, stiffness and force (Fig. 3.13.a, c and d). At this point, one section of the HNB is unrolled and damaged.

Finally, the HNB is elongated until it is almost completely unrolled and damaged just before breaking (Fig. 3.13.e.4). The HNB then breaks (Fig. 3.13.e.5). The contact between the tips and the HNB remains after breaking to ensure the attachment process.

These results confirm the non-constant stiffness behavior of HNBs in full range elongation. In previous works [BDN+06] where AFM cantilevers were inside the SEM, this behavior was not clearly measured for displacement of less than $10\mu m$. Furthermore, the non-homogeneous pitch of this HNB has been revealed with the non linear behavior of the stiffness and SEM visual feedback. The resulting elongation force therefore shows a highly non linear behavior which goes from 14.5nN for the smallest step made, to 2.95μN before breaking. This shows the wide range sensing of the system.

3.2.5.2 Non destructive characterization

The previous experiment had three principal limitations, which we aim to solve in this second experiment. First, the vacuum conditions disturbed the resonant frequency of the tuning fork with an increasing offset as time went on. Second, it is a destructive method whereby the HNB is destroyed after the experiment, and the tips of the tuning fork and manipulator can become contaminated with glue and remaining parts of the HNB. In addition to this, attaching the HNB by both ends prevents its rotation during tensile elongation, and so eventually damaging it. Finally, the SEM video is manually analyzed. This means that for every frame of interest, the elongation of the HNB is estimated with manually placed points in the video.

In order to solve the first problem, vacuum characterization is done prior to the experiment to identify the saturation time after pumping where the variation of vacuum conditions will not affect the experiment. For this purpose, frequency shift

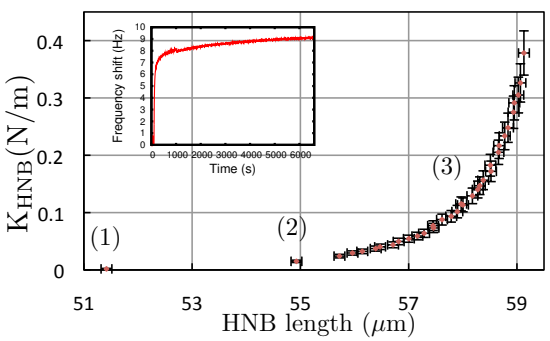

(a) *HNB longitudinal stiffness. Inset: Frequency shift recorded during pumping of the SEM chamber*

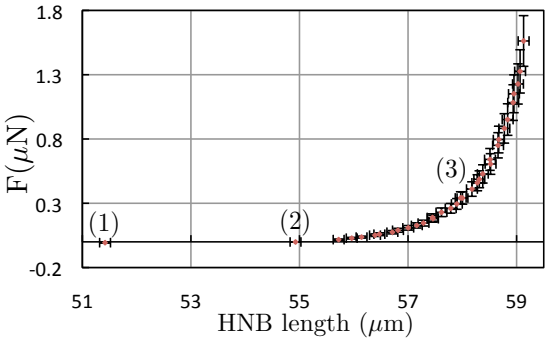

(b) *Force*

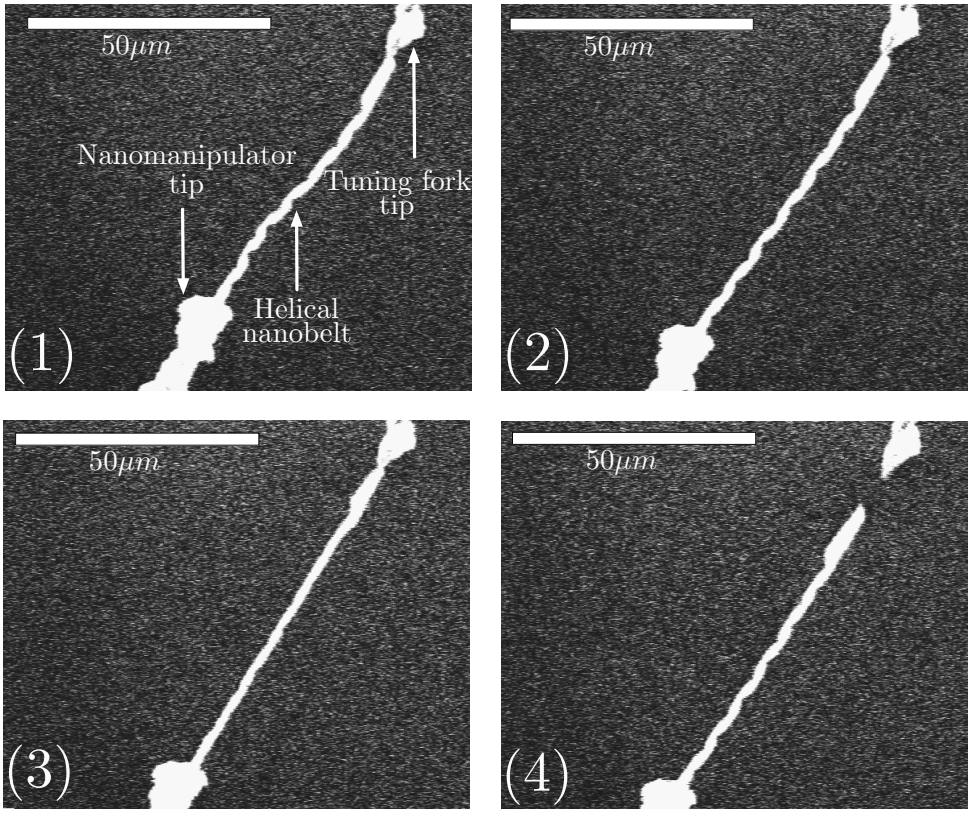

(c) *Captures from SEM video.*

Figure 3.14 - *Non destructive longitudinal pulling. (1) HNB pushing (2) HNB rest elongation, (3) HNB pulling, (4) HNB after detachment. Details on error estimation are gathered in appendix A*

is recorded during the pumping process (Inset Fig. 3.14.a). After ninety minutes, the frequency shift drift due to vacuum conditions is small enough for a ten minute experiment.

To overcome the second problem, as explained in section 3.2.4, electrostatic and van der Waals forces are used to maintain the HNB attached to the tip end of the tuning fork. Frequency shift noise decreased from $5mHz$ to $1mHz$ due to the higher quality factor of the tuning fork. For the elongation of the HNB, offline visual tracking software [Kin] is used. This, in addition to the high contrast used in the SEM, makes the error decrease from $0.2\mu m$ to $0.1\mu m$ even though the scale passed from $20\mu m$ to $50\mu m$.

The stiffness and force applied to the HNB are obtained in the same manner as previous experiments (Fig. 3.14.a and 3.14.b). Four different moments of the experiment are highlighted. First (Fig. 3.14.c(1)), the HNB is pushed and has a light "s-like" shape. This is mainly due to a much lower lateral stiffness than longitudinal stiffness of the HNB. Consequently, the stiffness measured is composed of both lateral and longitudinal and its absolute value is lower than the longitudinal rest position stiffness. The elongation, being negative, results in a negative force vector. After, the HNB is elongated to the rest position (Fig. 3.14.c(2)). and then, elongated further(Fig. 3.14.c(3)) untill it detaches from the probe of the tuning fork (Fig. 3.14.c(4)).

Table 3.3 - *Summary of experiments results. Exp stands for experiment.*

	Exp 1	Exp 2
Degrees of freedom of the manipulators	3	
Manipulators resolution in x/y/z (nm)	5/3.5/0.25	
Frequency shift resolution (Hz)	0.005	0.001
-> Corresponding Stiffness resolution (N/m)	0.0031	0.0006
HNB rest stiffness estimated by FEM (N/m)	0.009	0.011
HNB measured rest stiffness (N/m)	NA	0.014
HNB highest measured stiffness (N/m)	0.297	0.378
HNB highest measured elongation (μm)	9.95	4.13
-> Breaking/Detaching force (μN)	2.95	1.56

In comparison to the previous experiment, a higher non-linearity can be noticed. This is mainly due to the non-constrained rotation of the end of the HNB in contact with the tuning fork. As a result, the HNB freely adjusts its number of turns

through elongation, avoiding damages and the loss of a helical shape. Furthermore, the estimated force of $1.56\mu N$ before releasing, corresponds to the addition of van der Waals and electrostatic forces. The results of the experiments are detailed in table 3.3.

3.3 Dynamic force measurement with moving tuning fork

In previous experiment, the tuning fork was fixed on top of the substrate and the manipulators were used to manipulate the nanostructure. The objective of this section is to show that the measurement can be done while the tuning fork is moving. For this, micromembranes are used, they are membranes typically used micro mirror applications and were provided by the LPN (Laboratoire de Photonique et de Nanostructures) and LKB (Laboratoire Kastler Brossel).

3.3.1 System configuration

The membranes are fixed to the substrate with two supports, in consequence all measures need to come from the top. Since there was no XYZ piezostage available

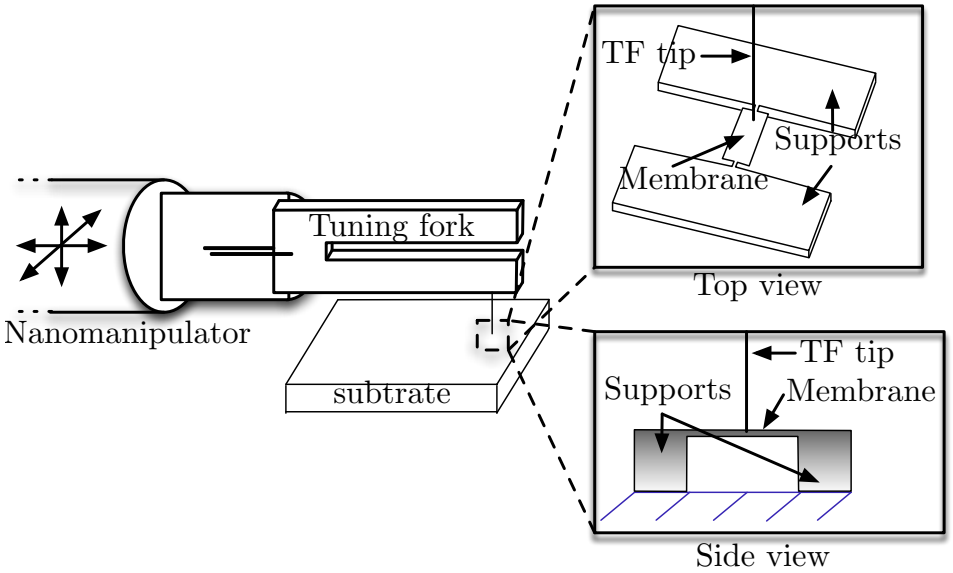

Figure 3.15 - *Systen configuration for membrane stiffness characterization*

inside our SEM, the tuning fork is attached to the end of one of the manipulators. The system configuration can be seen in Fig. 3.15. The nanomanipulator is used to move the tuning fork in order to scan the surface of the membrane. As the manipulator has no position feedback, the visual feedback of the SEM is used to estimate the position of the tip in X-Y-axis. The frequency shift is used to detect the contact of the tip with the surface of the membrane. The frequency shift is recorded for different contact points of the surface and Eq. 1.12 is used to generate a stiffness image of the surface of the membrane.

3.3.2 Surface mechanical characterization of membranes

Two different shapes of membranes were used. First, butterfly shaped membranes were used as seen in Fig. 3.16. No deflection was imposed to the membrane, in consequence, the obtained stiffness represent the rest stiffness. 35 positions equally distributed in the membrane were selected for the measurement. The estimated stiffness is plotted in function of the X-Y position in 3.17. Fig. 3.17 (a) represents raw data and Fig. 3.17 (b) is a cubic spline of 200x280.

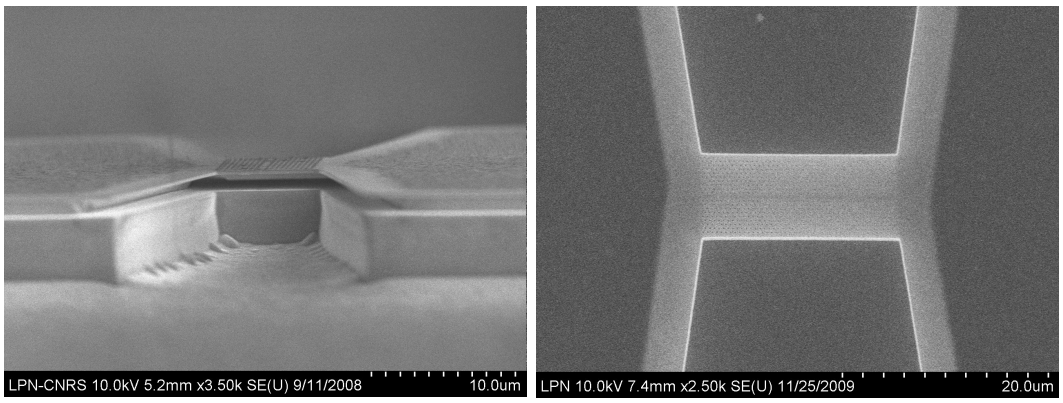

(a) **(b)**

Figure 3.16 - *Butterfly shaped membranes pictures under SEM (a) Top view, (b) Top view*

It is noticeable that the order of magnitude of the stiffness obtained is 10 times bigger than the one obtained for HNB even if it is the same tuning fork that was used for the second HNB. This shows the high range of the sensor. The obtained stiffness is expected due to the shape of the membrane. It is logical that the stiffness is higher near the support/membrane-end and lower far from it.

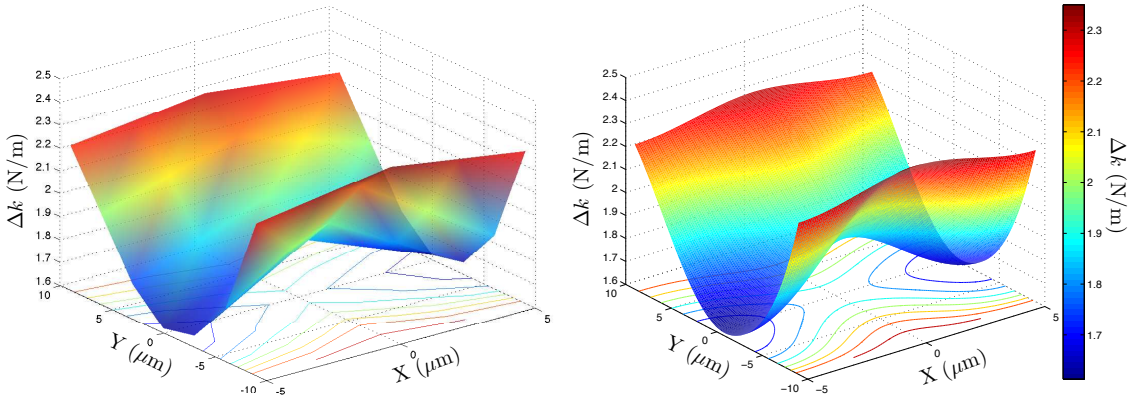

(a) **(b)**

Figure 3.17 - *Butterfly shaped membrane surface estimated stiffness. (a) raw data, (b) cubic spline*

The second type of membrane used is the bridge shaped. This membranes, as seen in Fig. 3.18 are only attached to the support by a small section.

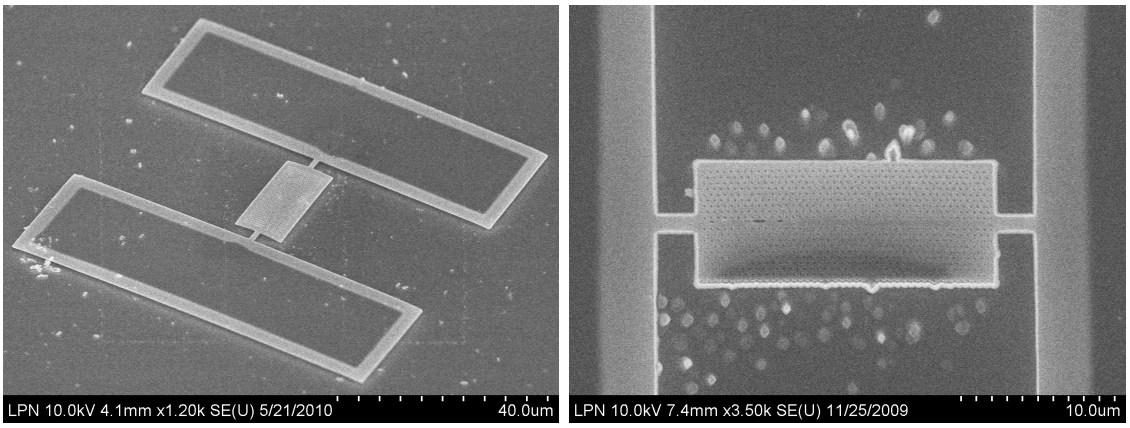

(a) **(b)**

Figure 3.18 - *Bridge shaped membranes pictures under SEM. (a) Large range top view with supports, (b) top view.*

The obtained Stiffness (Fig. 3.19) for the second membrane is also expected. The membrane stiffness in the short side, where it is attached, is not uniform in contrast with the first membrane. This is due to the small section attached to the support, in consequence the edged are more less blocked and more free to move. This results in a horse seat shaped stiffness curve were the highest stiffness is in the middle axe

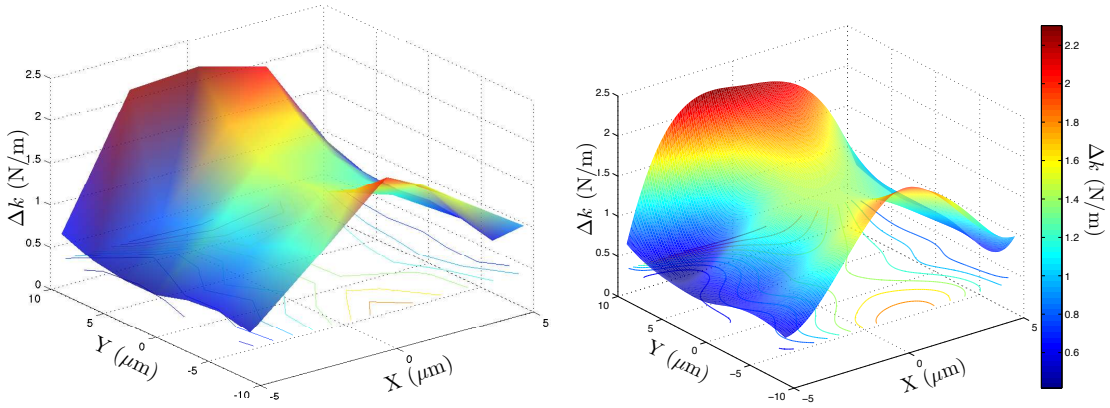

(a) (b)

Figure 3.19 - *Bridge shaped membrane surface estimated stiffness. (a) raw data, (b) cubic spline*

that passes trough both attachments were the movement of the membrane is more constrained.

The main source of error is the fact that the tip of the tuning fork was seen with a small angle form above and was a bit dirty in the sides. In consequence there was no visual feedback from the exact tip's end, making the positioning of the tip difficult and adding an error in X-Y axis.

3.4 Conclusions

In this chapter, a study of dynamic force sensors has been presented. The dynamic force sensor used is called tuning fork. One of the main challenges with this kind of sensor is the ability to estimate in a quantitative way the gradient of the force using frequency modulation, spatially when there is a tip attached. To address this issue, a two dimensional model of the sensor with a tip attached with an angle has been presented. This model shows the big influence of the tip angle on the measured stiffness and sets the conditions to take into account when a tip is added to the sensor for a particular application. The measured stiffness on normal axis is highly dependent on the lateral stiffness of the tip and the lateral stiffness constraint imposed to the tip by the substrate due to the interaction.

After, to prove the operation mode of the tuning fork, an in situ SEM robotic system for dynamic mechanical characterization of ultra flexible nanostructures with a tuning fork as force gradient sensor has been made. The system, composed of two nanomanipulators and a fixed tuning fork is used to mechanically characterize two helical nanobelts. A modified version where the tuning fork is mounted on one of the manipulators is used to mechanically characterize the surface of two membrane microresonators.

The first helical nanobelt is fixed between the tips of the tuning fork and a manipulator for full range characterization. For the second, electrostatic and van der Waals forces are used to maintain attached the nanobelt to the tip of the tuning fork, this way non destructive characterization can be done. The obtained stiffness of helical nanobelt ranges from 0.009 N/m to 0.297 N/m during full elongation and 0.011 N/m to 0.378 N/m for the non-destructive method. It was transformed with Hooke's law into forces as high as 2.95 μN for the first experiment and 1.56 μN for the second. The minimum steps of frequency shift measured are more than 5 times higher than noise levels, in consequence, the stiffness measurement resolution of the system with this specific tuning fork is around 0.0031 N/m for the first, and 0.0006 N/m for the second. The non-constant stiffness behavior of helical nanobelts during their controlled tensile elongation was clearly revealed in full range for the first time to the best of our knowledge. Furthermore, the revealed non-linear behavior of the stiffness with SEM visual feedback shows the capability of a robotic system with a dynamic force sensor to understand the mechanical properties of the nanostructure due to geometry deformation.

After, in order to show the capabilities of force gradient measurement of the tuning fork while it is moving, two different shapes of membranes were used as sample structure for mechanical characterization. The tuning fork was mounted on the manipulator for sensing. Obtained stiffness ranged from 1.6 N/m to 2.3 N/m for the butterfly shaped membrane and 0.7 N/m to 2.2 N/m for the bridge shaped membrane. The stiffness obtained expand the demonstrated range of the sensing device. Furthermore the dexterity of the system was proven.

The main limit of the system is the resolution of SEM visual analysis. Taking pictures and not videos from SEM to estimate with more accuracy the elongation of the helical nanobelt and obtain stiffness for smaller displacements can be done. However, for long scanning times, the helical nanobelts are too much exposed to e-beam thus will deposit to increase mass of HNB due to contaminants (mainly carbon) deposition. Furthermore, the nanomanipulator can be installed on top of

a close loop controlled xyz piezo nanostage to obtain the displacement with more accuracy and increase the dexterity and resolution of the system.

Dynamic mechanical characterization of other ultra flexible nanostructures like nanowires, nanotubes and graphene membranes for example are possible in the future with the proposed system. Furthermore, by incorporating environmental electron microscopes (ESEM) or fluorescence optics, flexible and elastic biological nanostructures such as DNA, proteins, cells, tissues are also in the scope of this new system.

In the following chapter, an integration of dynamic force sensing presented in this chapter, into the two tip AFM presented in chapter 2 is done.

Chapter 4

Dynamic force feedback with quartz oscillators for fast parallel imaging and 2D manipulation

Contents

In chapter 2, a 3D manipulation system has been presented based on an AFM. A nanotweezer has been build from two different AFM arms with protrudent tips. With this system, pick and place is now feasible in the air with force feedback. Two different applications of the system were presented. For the first, pick and place micromanipulation has been done where micropyramids were build with nylon microspheres of diameters of 3 μm to 4 μm (Fig. 4.1.(a)). In this case, the optical

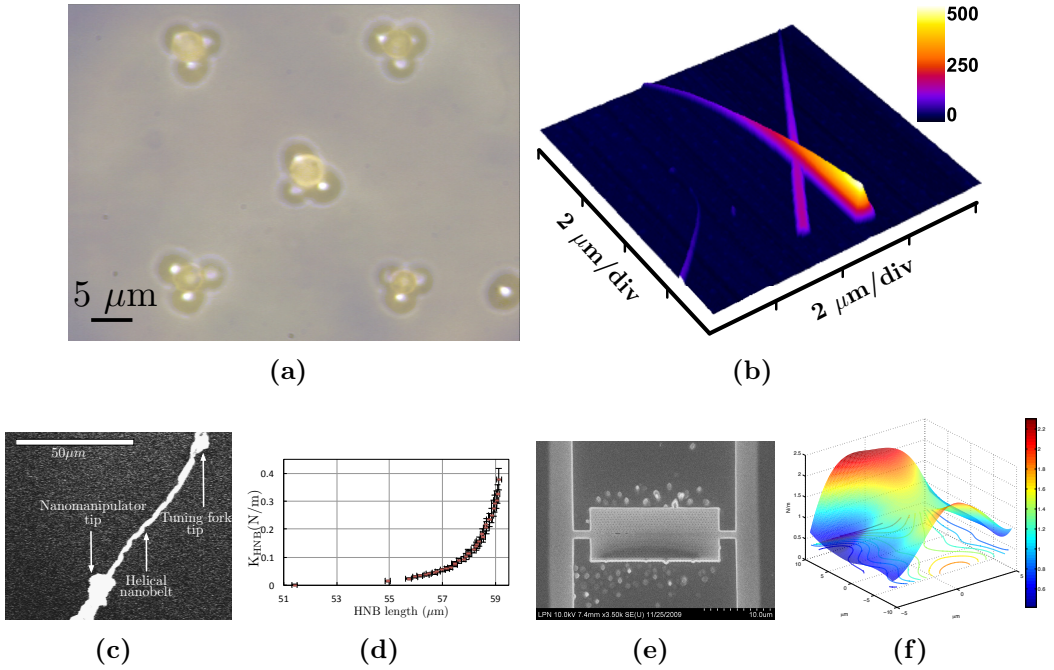

Figure 4.1 - *Results from chapter 2 and 3 Force feedback manipulation with two tip AFM: (a) 5 micro pyramids made of nylon microspheres, (b) nanocross made with silicon nanowires. Dynamic force sensing of quartz tuning fork: (c)-(d) HNB characterization with fixed tuning fork, (e)-(f) membrane surface characterization with a moving tuning fork.*

detection of the coarse position of the spheres and the AFM scanning of the grasping point location were combined for the pick and place of the microobject. Then, 3D pick and place manipulation was presented, for this, nanocrosses of silicon nanowires were made (Fig. 4.1.(b)). Due to the size of the objects, the nanomanipulation pick and place task rely only on the AFM imaging by one of the tips.

Two of the main drawbacks of the system are the speed of the sensors as well as the dexterity of the arms. The first is a mayor problem for AFM imaging acquisition times. A normal AFM image takes between 3-10 minutes. During that time, undesired effects like thermal drift or creep can cause a change in position of the objects to manipulate. This limits the application of the AFM for automation purposes. From this, the necessity of a fast force sensor. The second drawback, is the dexterity of the arm. It comes from the fact that sometimes the arm holding the cantilever is the one that moves and not the substrate. This cause a problem in calibration of the cantilever because the lasers and photodiodes of this system are fixed, and do not move with the cantilever. In consequence, force calibration will

only be valid for small displacements of the cantilever. Making the photodiode and laser mobiles with the nanostage might solve this issue, but it will add weight to the stage, reducing the reaction time. Another solution for this would be to change the cantilever with external optics with a sensor with selfsensing capabilities.

Chapter 3 aims to answer these questions. In that chapter, a study on dynamic force sensing with quartz oscillators is presented. In the first part, the quartz oscillator, which in this case was a tuning fork (Fig. 4.1.(c)-(d)), was fixed, and an HNB was used an example to demonstrate the capabilities of the sensor for dynamic force sensing. Then, in the last part, the tuning fork was mounted on the tip of a nanomanipulators and was used to scan the surface stiffness of a membrane (Fig. 4.1.(e)-(f)). This way, the dynamic force measurement was shown while the sensor was moving.

This chapter, represents an integration of the two previous chapter. It is here where a dynamic force sensor will be introduced into the two tip AFM improving the throughput of the entire system. In the first part of this chapter, a complete analysis of the system depicted in chapter 2 in terms of speed is made. After that, the different kinematical configurations of the system are compared followed by the proposed force sensor and software and hardware modifications. The sets of experiments to validate the system will be divided in three parts. First, imaging test are done with a known hard surface to validate the calibration and speed of the complete system. The second set of test consist in the image acquisition of a hard surface with loose objects like gold nanospheres with the objective of showing the non-invasive capabilities of the system. Finally, a manipulation task with two cooperative arms of the new system is done to show the potential application of the system with nanomanipulation.

4.1 Fast parallel imaging and manipulation system

4.1.1 Objectives

In order to understand the role of a fast imaging tool in the parallel imaging and manipulation task, the whole manipulation task time needs to be analyzed. The task time t_{task} of the parallel imaging/manipulation operation can be given by [XHR09]:

$$t_{task} = max(t_s, t_m) + t_s \tag{4.1}$$

where t_s is the scanning time of one image frame and t_m is the total manipulation time estimated from the sum of manipulation time of each single nano-object. For the normal-speed AFM, t_{task} is often equal to $2 \cdot t_s$ except for a complex manipulation task that cannot be fulfilled within one frame period, and so has task time of $t_m + t_s$. This scheme can save much time, as compared with the serial imaging/manipulation operation that has task time of $t_m + 2 \cdot t_s$. One disadvantage of this scheme is that environment-based motion planning is unavailable during the manipulation. However, the parallel imaging/manipulation can be perfectly performed by this scheme if a manipulation objective is defined before the operation. In contrast, for the second scheme, the task time with the high-speed AFM is approximately equal to t_m due to very high frame rate of image scan. The manipulation process in this scheme is monitored by the high-speed visual feedback as the manipulation performed in the SEM. The second scheme is undoubtedly more efficient than the former one.

Even if the time is reduced from $2 \cdot t_s$ to $t_m + t_s$, at the best, it can not be more than twice as fast as before. The big challenge will be to reduce t_s. The new system aims to achieve this, keeping the manipulation capabilities of the old system. For this, a series of objectives for the new system need to be accomplished:

- Have a two tip AFM system capable of imaging in both static and dynamic mode. Dynamic mode imaging should be possible with one of the two tips. Amplitude, phase and frequency modulation are in the scope. The true non-contact mode should avoid wear of tips as it is a non-invasive technique with the substrate.

- Increase the dexterity of the imaging tip. Self-sensing sensors are in the scope to avoid calibration issues during the movement of the arm holding it.

- Have force sensor with a low settling time τ for high speed AFM imaging. This will reduce the effect from thermal drift and increase the potential application of the current system for automation.

- Have a high speed imaging capable processing system. The system should be able to process data from the sensor at high speed for imaging control.

- And have a flexible 2 tip kinematical configuration allowing 2D manipulation and imaging.

To achieve this, first, an analysis of the different kinematical configurations of the two tip AFM need to be made to be able to select the one according to our needs.

4.1.2 Kinematical configurations of the system of the Two tip AFM

In chapter 2, a nanotweezer has been made with two protrudent atomic force microscope tips to make pick and place of micro and nanoobjects with force feedback. Two different kinematical configurations are used (Fig. 4.2).

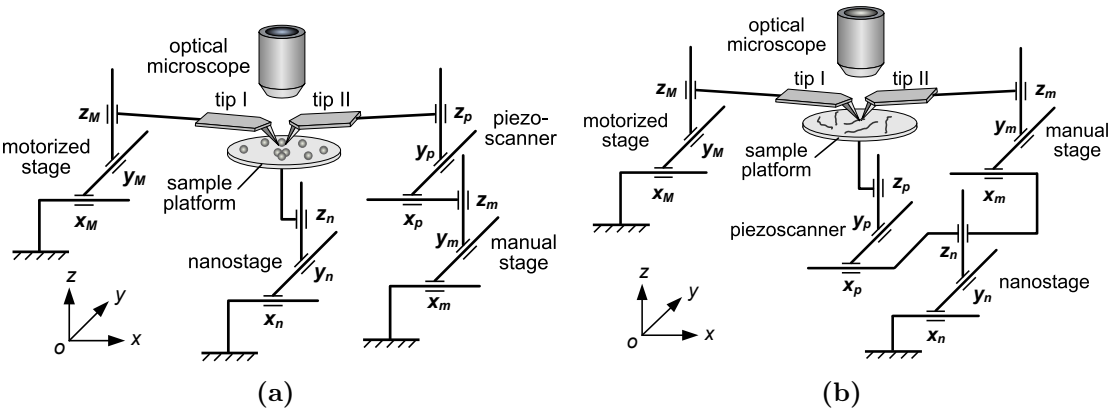

Figure 4.2 - *Different kinematical configurations of the AFM system for the manipulation task presented in chapter 2. (a) System configuration for 3D micromanipulation, (b) and nanocrosses fabrication*

To understand the differences between the two configurations, the differences between the two XYZ nano positioning devices must be identified:

	Nanostage	**Piezoscanner**
Type	Closed loop	Open loop
Range	40 μm XY and 12μm Z	10μm XYZ
Resonant frequency	400Hz XY, 1.5 kHz Z	29kHz

For both configurations, one stage is charged of controlling the distance between the two tips, and the other is charged of the pick and place task. For 3D micro manipulation, the open loop stage is used for the tip-tip distance and the wide range stage is used for the pick and place due to the distance separating the initial and final position of the microspheres. For the manipulation os SiNW, it is the opposite, any of the stages could be used for the pick and place due to the small displacement distances, however, only the closed loop can be used for controlling the distance between the two tips due to the stability of the stage compared to the open loop, even if creep and hysteresis are compensated.

Another difference between the two configuration is which of the scanner is used for AFM imaging without disturbing the distance between the non scanning tip and the substrate. For the micro configuration, it is the tip number II driven by the piezoscanner (open loop) that is able to scan the surface without changing the distance between Tip I and substrate. For nano configuration, it is the tip number I that scans with the movement of the nanostage (closed loop).

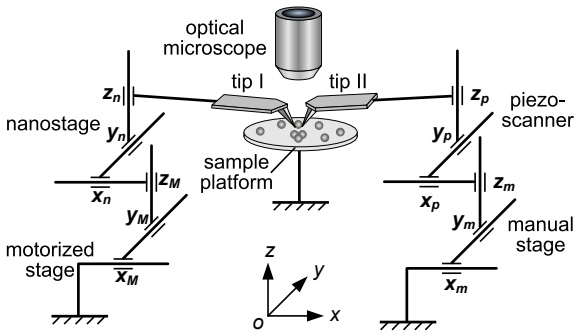

Figure 4.3 - *System configuration for parallel imaging/manipulation with two tip atomic force microscope.*

For a parallel imaging and nanomanipulating system [XHR09], a fast AFM scanner is needed and a precise and stable positioning stage for pushing and pulling objects. The piezoscanner is used for the the imaging of the substrate and the nanostage is used for the manipulation as seen in Fig. 4.3. With this configuration, the imaging with the tip number I and the piezoscanner will not change the distance between the tip number II and the substrate. Additionally, the manipulation with the nanostage won't affect the distance between the scanning tip and the substrate.

For manipulation, scanning range and flexibility, the configuration used for 3D micro manipulation is chosen. The system diagram of the new system is represented in Fig. 4.4. The quartz oscillator will replace the Tip II for true non-contact mode imaging. This imaging can be done with either the closed loop stage or the open loop. The last one has the advantage of avoiding movement of the substrate, thus keeping distance between Tip I and substrate constant. Closed loop nanostage and Tip I will be used for manipulation.

To achieve these objectives with the desired kinematical configuration depicted in Fig. 4.4, a series of modifications need to be made to the system. In the following

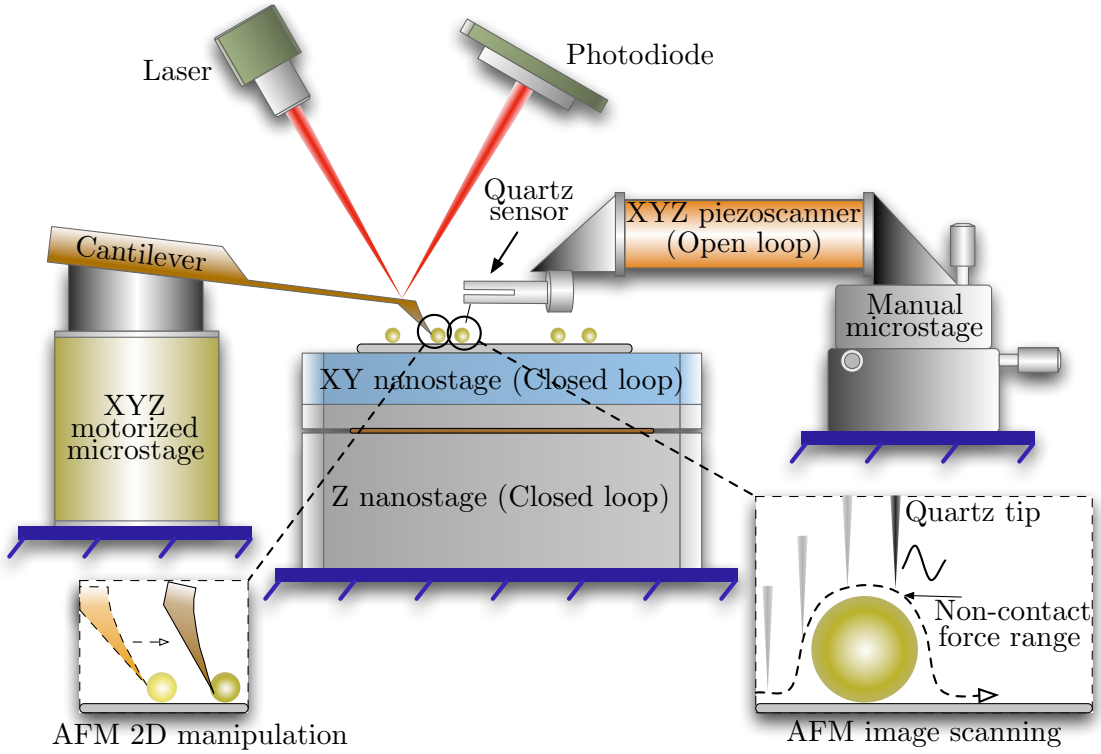

Figure 4.4 - *System diagram for new configuration of the two tip system. The quartz is integrated into the system for true non-contact mode imaging.*

sections those will be presented.

4.1.3 System modifications for high speed AFM

In order to modify the AFM system, an analysis need to be made of the data flow for the process of image acquisition. This way, the key blocks limiting the speed of the system are identified. The imaging process of an AFM can be represented by the diagram in Fig. 4.5.

In this diagram, three main blocks can be identified:

- **The Force acquisition block:** it is composed of the interacting force sensor with the substrate and the electronics need to to control sensor and obtain the force. In a typical AFM, the sensor would be a cantilever with tip, and the sensor electronics would be the photodiode with its electronics.

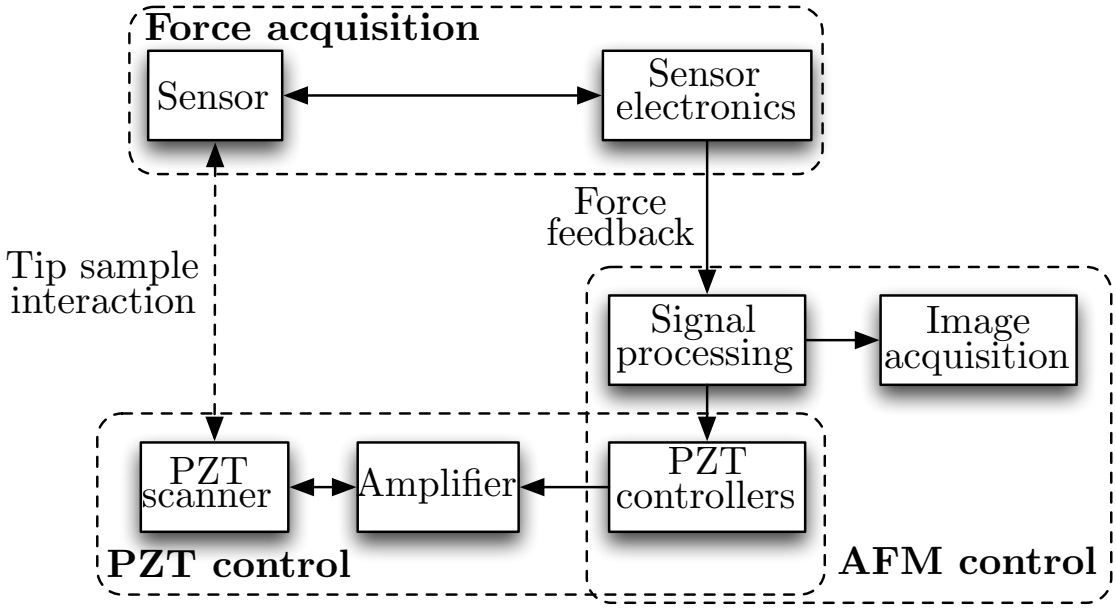

Figure 4.5 - *Control flow diagram for conventional AFM image acquisition. Three main blocks can be identified, the force acquisition block, the AFM control clock and the PZT control block.*

- **The AFM control block:** It is the main control block where the data from the sensor is treated for the piezo control in Z-axis to maintain the desired setpoint. It is also charge of controlling X and Y-axis to obtain the image. It is generally the mainframe computer and apart from imaging can be used for manual control of piezo, making approach retreat curves, plotting results, among others.

- **The PZT control block:** It is composed of the piezo actuators of the system with their amplifier and controllers. For an open loop piezo, the controller is software only. For a closed loop there are two controller. The first is included with the amplifier and is charged to maintain the desired position. The other controller is generally in the mainframe computer and its charged of changing the position setpoint.

The current setup is mainly limited by the two first blocks and their modification is treated in this work and will be presented in the following sections. The piezo control is not within the scope of this thesis and remains a challenge for future work.

4.1.4 High speed sensor

In chapter 1 and 3 dynamic force sensing was presented as an alternative for increasing the speed and the dexterity of the system. This technique has generally been used with quartz tuning forks. They are quartz oscillators and the typical resonant frequency is 32.768kHz. For high speed AFM, even using frequency modulation, these sensors remain slow due to their low resonant frequency. In consequence, in order to really take advantage of dynamic force sensing for AFM imaging, quartz oscillators with higher resonant frequency needs to be used. In the following, a quartz oscillator with frequencies of several MHz will be presented.

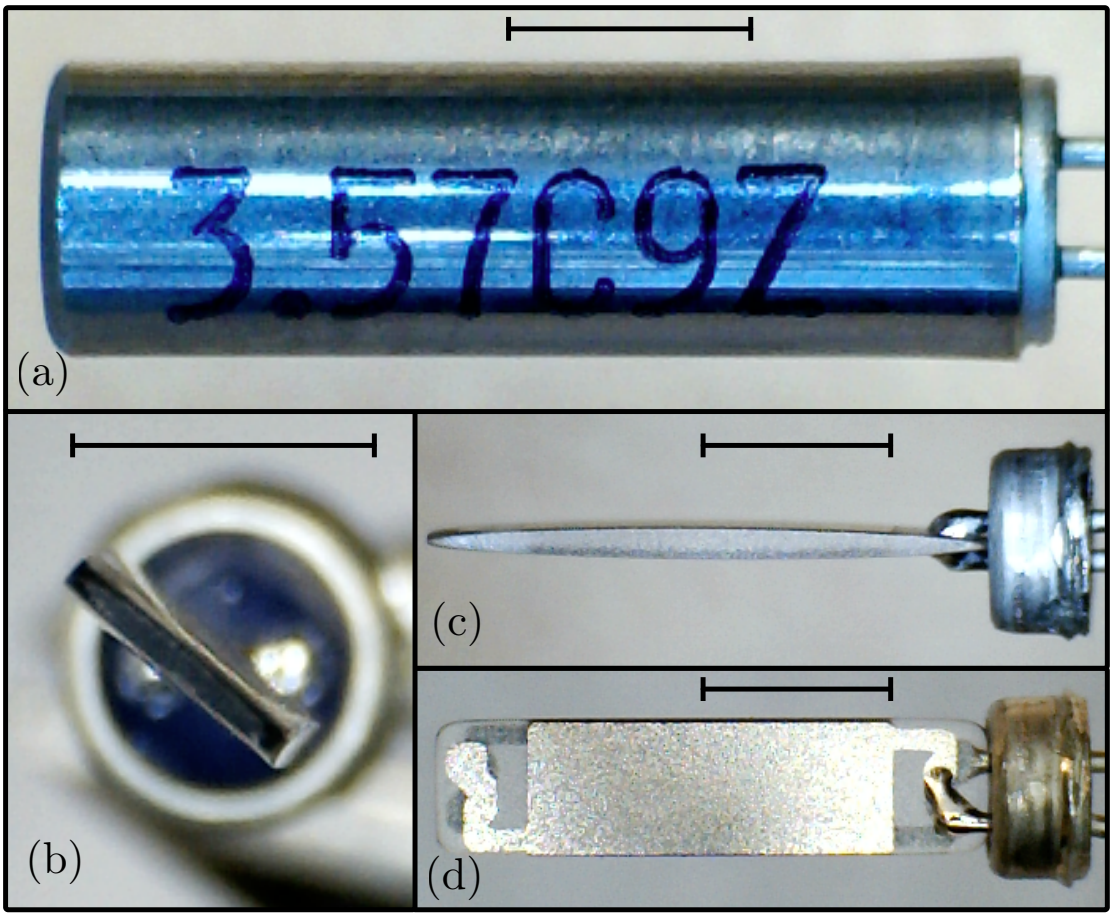

Figure 4.6 - *Different views of the quartz sensor. Scale bars correspond to 2.7 mm. (a) Original package of the quartz, (b) top view and (c)-(d)side views.*

The quartz oscillators used are made by CITIZEN AMERICA - CSA310 and have a resonant frequency of 3.579545 MHz according to fabricant. They can be found with resonant frequencies of several MHz and not longer are tuning forks.

The geometry is different, they only have one prong compared to the two prongs of the tuning forks. The are also larger (8.1mm for the quartz, 3.2 mm for the tuning fork used in chapter 3). In Fig. 4.6 the different views of the oscillator be seen. The original package (Fig. 4.6.(a)) is very similar to the tuning fork, the quartz is isolated with a semi-vacuum capsule. After the capsule is removed, the single prong sensor oscillator can be seen (Fig. 4.6.(b), (c) and (d)).

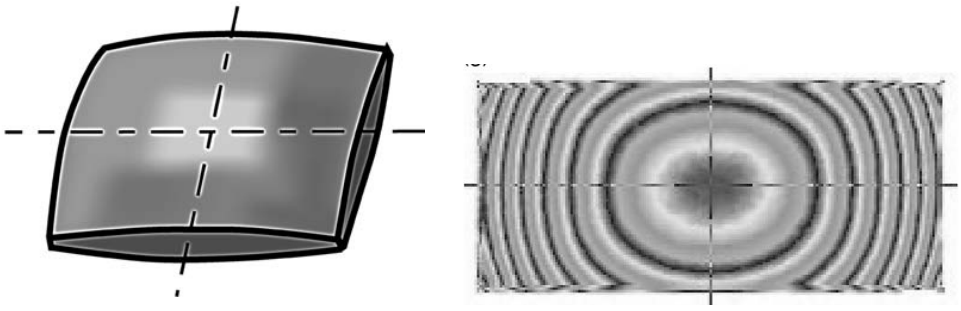

(a) **(b)**

Figure 4.7 - *Previous works on oscillation mode of quartz with similar shape [JAH04]. (a) Shape of the quartz analyzed. (b) interferometry of the resonator.*

The oscillation mode of the new sensor is not known with precision to the date. There are no works that directly address this issue. There is however one work that analyze the oscillation modes of quartz with similar shape [JAH04]. The shape of the quartz they used is depicted in Fig. 4.7.(a). Is not exactly the same shape, our quartz has the same concave shape in a longitudinal cut (Fig. 4.6.(c)) but in lateral cut is more a rectangle shape (Fig. 4.6.(d)). Still it is the closest analysis in the bibliography to the quartz used in this chapter.

According to them (Fig. 4.7.(b)), the quartz oscillation mode has a wave shape starting from the center. In consequence, there are oscillations normal to the surface. The amplitude of these oscillations decreases with the distance to the middle of the quartz. This has been validated experimentally with our quartz. In fact, the position of the added mass (tip+glue) is critical for the quality factor of the sensor. As the distance of attachment to the middle of the quartz increases, the higher the quality factor is and the lower the excitation amplitude. In the same time, bigger amplitudes of oscillation are observed in the middle area but with low quality factor. The same mode of oscillation is supposed at the other side of the sensor, still, mass compensation has not been attempted. In summary, the Tip Is attached somewhere between the middle of the quartz and the end. It is a compromise between the

quality factor and the sensibility. This position is obtained empirically and tends to be closer to the end than the middle of the sensor.

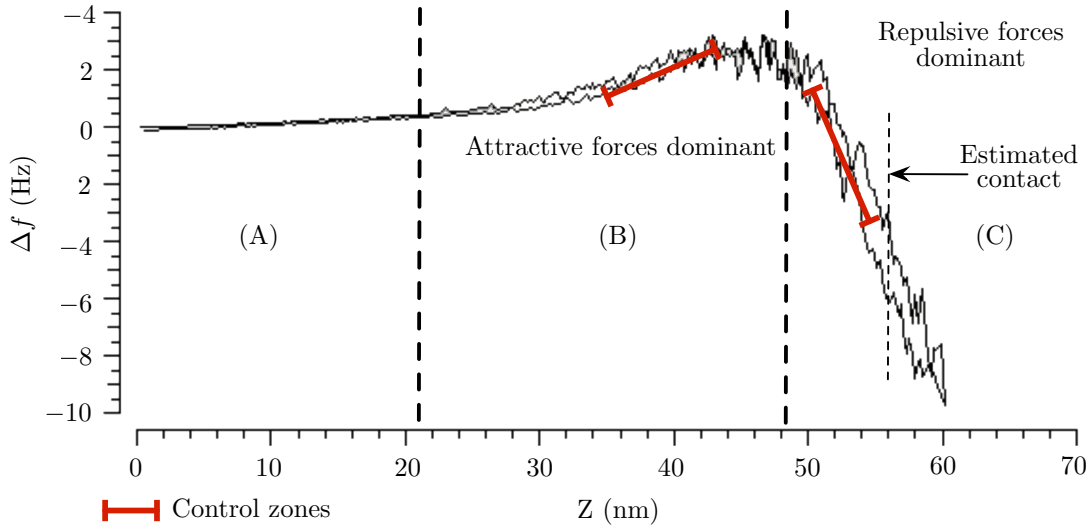

Figure 4.8 - *Approach retreat obtained with quartz in normal mode. (A) Before sensing any force. (B) Attractive forces are dominant compared to repulsive forces, thus positive Δf. (C) Repulsive forces are dominant. Contact is estimated a few nanometers after Δf decreases.*

Furthermore, the axis of oscillation at the attached tip of the sensor in not well known. In consequence it has to be experimentally verified with an approach retreat curve. When the quartz is oscillating in the axis of the tip (normal to the substrate), the obtained approach retreat curve is depicted in Fig. 4.8. It is called normal mode, and works with non contact forces. It was obtained with the tip attached perpendicular to the quartz surface. When the tip approaches the surface, first it senses the attractive forces, thus a positive frequency shift (Fig. 4.8.(B)). Then, the repulsive forces become dominant (Fig. 4.8.(C)). The contact between the tip and the surface occurs after a few nanometers of more movement. The range of these regions depend mainly on the geometry of the end of the tip. The diameter of the Tip Is near 100nm, thus the large range of the forces. With smaller tips, this range decreases. To control the quartz in this mode, both attractive or repulsive zones can be used (red bars in Fig. 4.8), the first being more stable due to the slope of the frequency shift and longer range. If repulsive forces are used, it is less stable but more sensitive, additionally, there is a risk of contact with the substrate.

When the Tip Is oscillating parallel to the quartz electrode, the oscillation of the

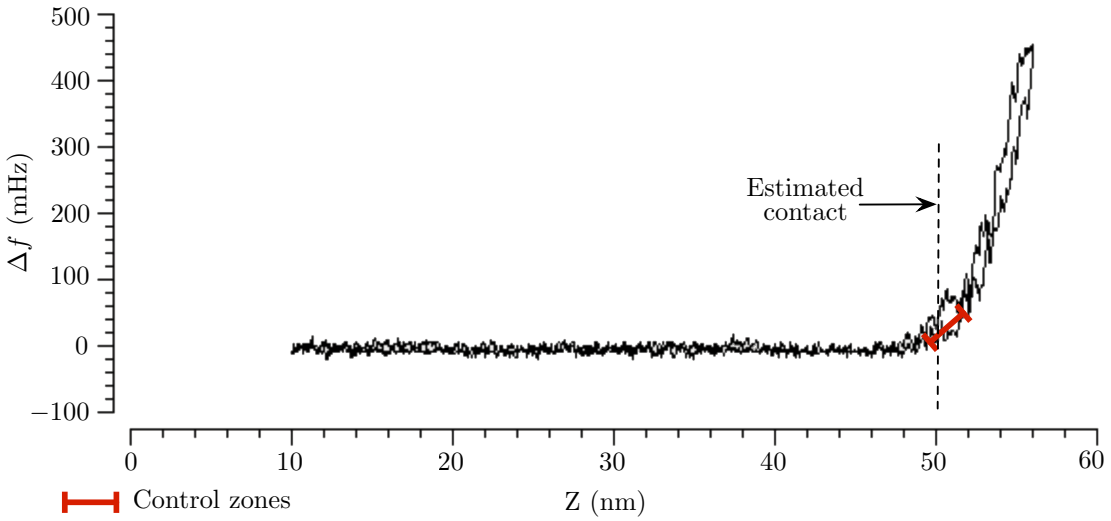

Figure 4.9 - *Approach retreat curve obtained with quartz in lateral/shear mode.*

Tip Is parallel to the substrate. It is called lateral force sensor [Gie03]. For this shear mode, it is the friction force gradient between the tip and the surface that is sensed. An approach retreat curve is depicted in Fig. 4.9. In this case, the frequency shift increase when friction due to the contact force increases. The set point should be as small as possible to avoid wear of the tip and modification of the substrate.

The normal mode has been observed only when the tip was attached with an angle of 90 degreed with the quartz surface (Fig. 4.10.(a)). However, shear mode

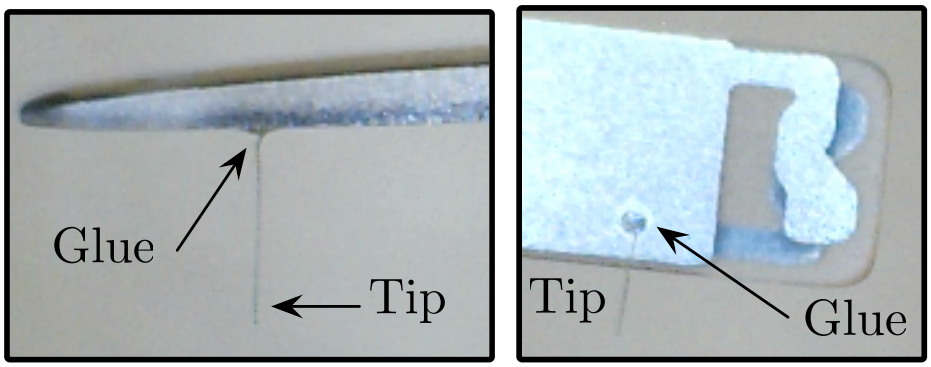

Figure 4.10 - *Quartz with tip Attached. (a) 90 degrees attachment for normal mode. (b) Parallel attachment for shear mode.*

was observed with the tip attached normal to the surface and parallel to the surface (Fig. 4.10.(b)). Our hypothesis is that the attachment point local oscillation depends on the position of the wave of the mode.

For this sensors, tungsten tips (T-4-10-1 mm, tip radius: 100 nm, GGB industries) are attached to the sensor using electrically conductive silver epoxy EPO-TEK H21D (Epoxy Technology). The SEM compatible preamplifier for this high speed oscillator, as well as the amplifier used in chapter in chapter 3, were provided and patented by Jérôme Polesel Maris of CEA SACLAY, DSM/IRAMIS/SPCSI [Jé]. An OC4-Station from SPECS-Nanonis is used for the oscillation control of the sensor.

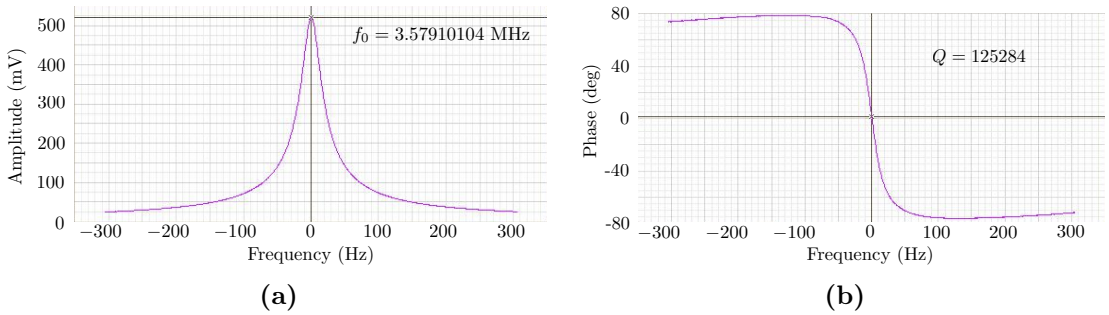

Figure 4.11 - *600 Hz frequency sweep around resonant frequency of a quartz oscillator with tip. (a) amplitude and (b) phase. The resonant frequency is estimated at* $f_0 = 3.57910104$ *MHz with 10 mHz precession with the OC4 controller and the quality factor* $Q = 125284$.

The quality factor of the sensor with Tip Is between 10000 and 200000 depending on the position of the tip and the weight added. An example of frequency sweep can be seen at Fig. 4.11. For this quartz with tip, the resonant frequency is estimated at $f_0 = 3.57910104$ MHz (with 10 mHz precession with the OC4 controller) and the quality factor is $Q = 125284$. One of the drawback is that as it is so stiff (Higher than 10 kN/m), that any contact with the substrate will result in a damaged tip or substrate.

This sensor has a resonant frequency around a hundred times higher than the cantilever with protrudent tip used. This, combined with the high quality factor and stiffness make this quartz a high speed, very sensitive sensor with amplitudes of oscillation in sub Ångström orders of magnitudes making them ideal for fast true non-contact mode imaging. In order to take advantage of the high speed of the sensor, the AFM controller needs to be remade.

4.1.5 AFM controller

To introduce the new sensor in the system, one of the previous tips with cantilever is removed. Additionally the PLL needs to be connected to the AFM controller which in this case is computer 2. A second data acquisition card, a NI-6259, was plugged to the system to be able to connect the PLL analog output. This DAQ is the fastest DAQ available from national instrument of penultimate generation. The modified system can be seen in Fig. 4.12.

One of the main limitations of previous system was the precision of the operating

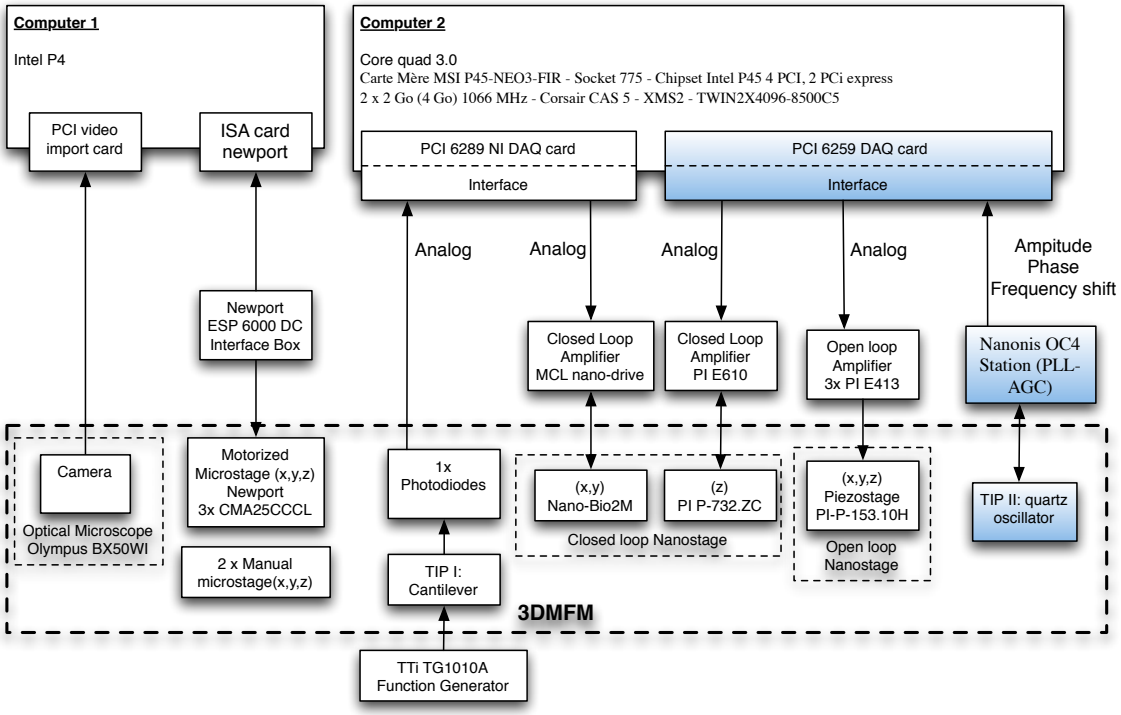

Figure 4.12 - *Hardware diagram of the two tip AFM setup after modifications.*

system used, around 1-10ms. A real time operating system is needed to improve it. Linux distribution Debian Squeeze was installed and the kernel was patched with RTAI for real time capabilities. The precision of the operating system decreased to less than 1 μs. A completely new software for AFM control has been developed in c/c++. With it, each of the piezo can be controlled individually and AFM images can be made in amplitude, frequency of phase modulation with either the cantilever or the quartz oscillator. The main program interface can be seen in Fig. 4.13. The obtained AFM image can be plotted in 2D (Fig. 4.13) or in 3D(Fig. 4.14).

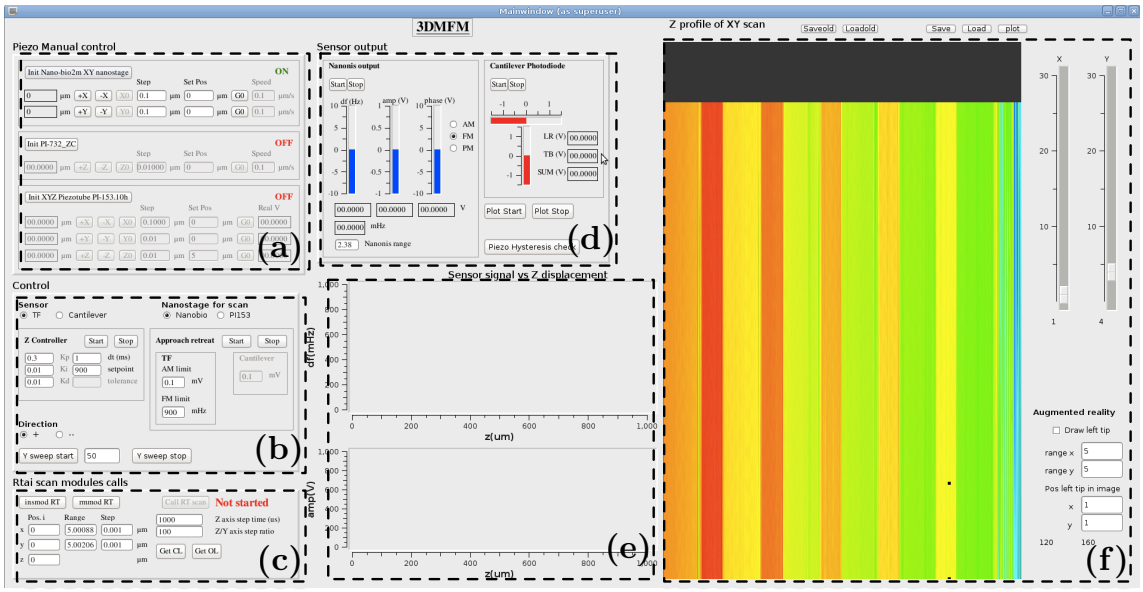

Figure 4.13 - *Main interface of the newly developed AFM controller. (a) Manual control of the piezoactuactors, (b) PID controller setup, (c) Real time configuration (d) output of photodiode and dynamic oscillator, (e) 2D plot area and (f) 2D AFM image plot area.*

After all the modifications depicted before are done, the new system has:

- An AFM with two tips. The first Tip Is a cantilever for manipulation and the second one is a quartz oscillator for AFM imaging.

- A new type of quartz oscillator for fast sensing and fast imaging. The typical resonant frequency of the sensor is 3.57 MHz. It is near 100 times faster than previous dynamic sensor, the tuning fork and the cantilever.

- A newly developed AFM controller with a precision between 1 and 10 μs (DAQ included). It is between 100-1000 times faster than previous system.

- A system with the ability of imaging in dynamic mode. This can be done with either, amplitude, phase or frequency modulation. For the first, the resonant frequency is fixed, and the amplitude of oscillation is used for control feedback. In the second mode, it is the phase that is used for control feedback. For frequency modulation, the amplitude and phase are fixed with an AGC and a PLL, the obtained frequency shift is used as the feedback of the controller.

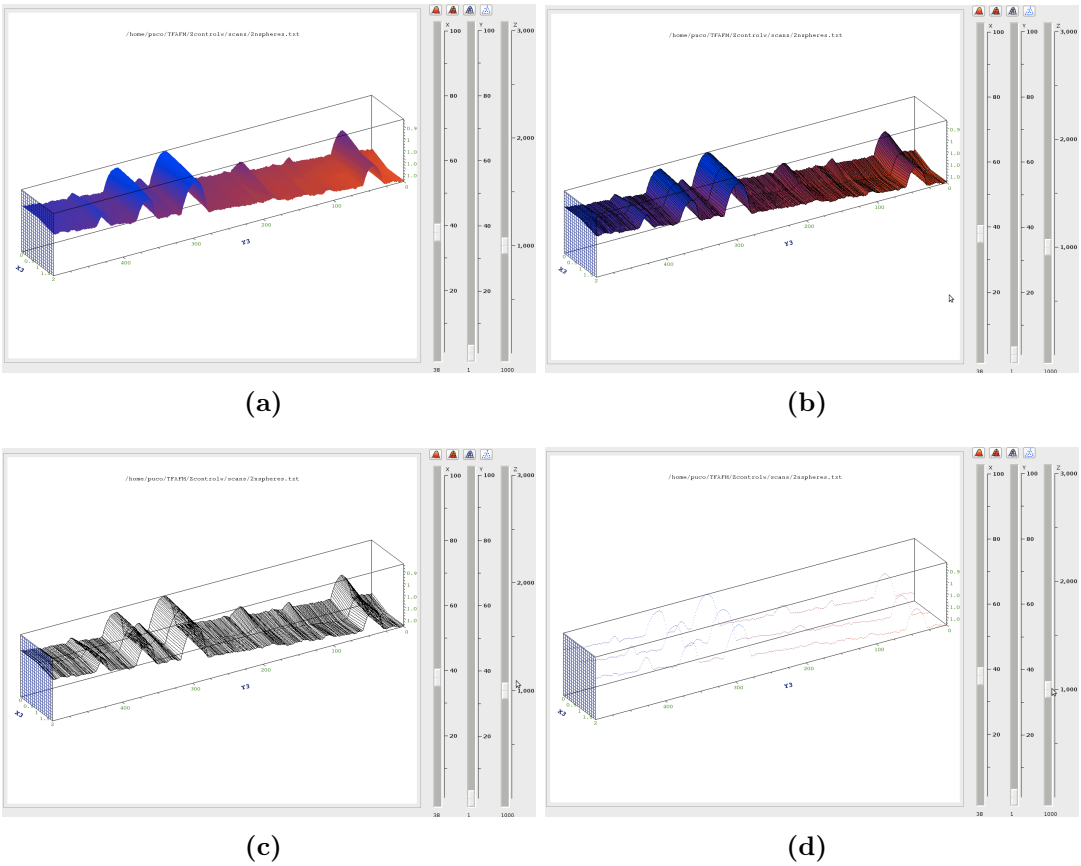

(a) **(b)**

(c) **(d)**

Figure 4.14 - *Developed AFM image 3D plot interface, (a) Normal spline visualization mode, (b) spline with wireframe mode, (c) wireframe mode and (d) dots mode.*

- A new sensor with self-sensing capabilities allowing the system Tip II to move freely without the need of recalibration.

In the following the experiments done in order to validate the functioning of the system with the dynamic force sensor are presented.

4.2 Experiments

The set of experiments done with the system are divided in three parts. In the first part a hard surface imaging is done in order to calibrate the open loop piezo and validate the speed of the system. Then imaging test are done on loose nano objects

on top of a hard surface in order to confirm the non invasive imaging. Finally, a nano manipulation task is done, in this case the two arms of the system are used, the quartz sensor for imaging and the cantilever for manipulation.

4.2.1 Hard surface scanning

In order to validate the speed of the system and calibrate the open loop piezo(Fig. 4.15), an AFM image of a calibration substrate has been done. For the example image of Fig. 4.15, due to the size of the pitch of the substrate (5 μm), the closed loop nano stage X-Y axis are used, for Z-axis, the open loop piezo is used. The height of the steps is 100nm. The size of the image is 20 μm and 5 μm in X and Y axis respectively. To avoid the dependency of Z-control on the image acquisition, the slope of the steps are aligned before the image with an optical microscope with the fast axis of the scanning (Y). The quartz used for this example was working in normal mode and is the same quartz from Fig. 4.10.(a). Attractive forces control zone was used for stability. The image acquisition time is manually set and in this case was 12.6 seconds. It is an important improvement compared to previous version of the system of mode than 50 times. The AFM controller was not set at full speed,

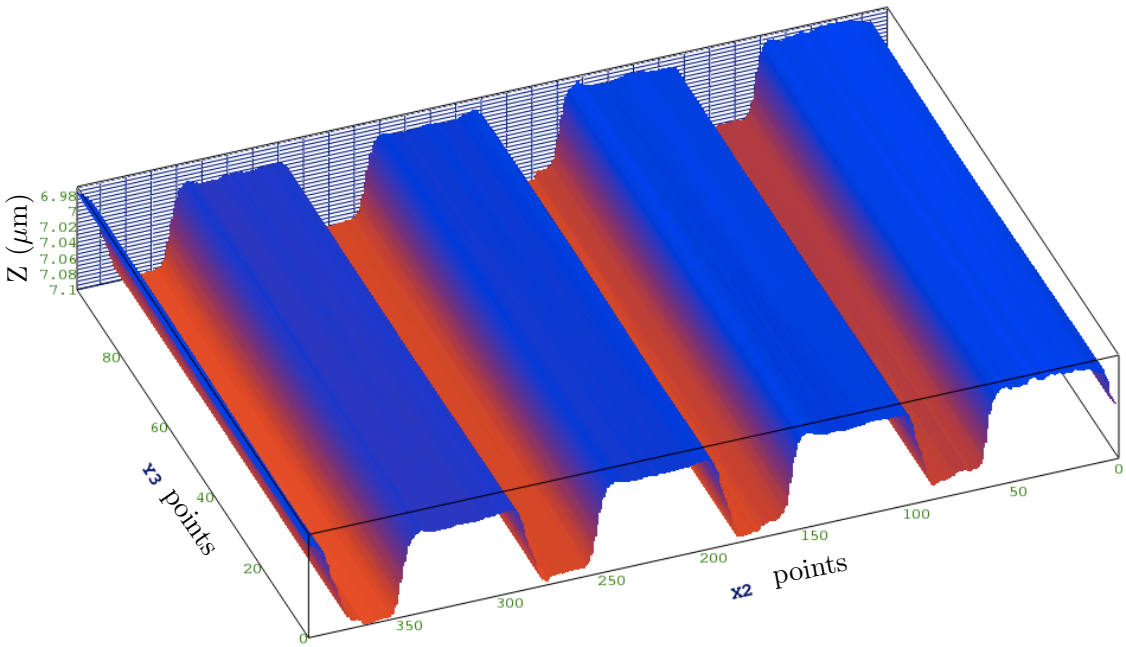

Figure 4.15 - *Raw data of a hard surface AFM imaging for calibration of open loop piezo with a calibration substrate (HS-100MG from Budget Sensors). 20µm in X-axis and 5 µm in Y-axis. Image acquisition time is 12.6 seconds.*

and the step time used is 20 times higher than the latency of the system. On the new system, the open loop piezo hysteresis was calibrated and compensated with the Prandtl-Ishlinskii operator [KK01] as with the previous version of the system.

4.2.2 Nanospheres imaging

After the experiments on hard surfaces have been done and the piezo has been calibrated, images of loose object have been done. For this, gold colloids of different sizes from Ted Pella, inc, were deposed on top of a silicon substrate using the method described in [LDK+07]. For this experiment, the sensor was working in shear mode and only the open loop piezo actuators were used. First, an image of 80nm diameter gold colloids has been done. Raw data of the image can be seen in Fig. 4.16. The first noticeable thing is the orientation of the plane of the image. This is due to the alignment between the open loop piezo and the substrate and not to thermal drift during the imaging. Another noticeable thing is the pyramidal shape of the spheres when near the substrate. This is mainly due to the diameter of the tip

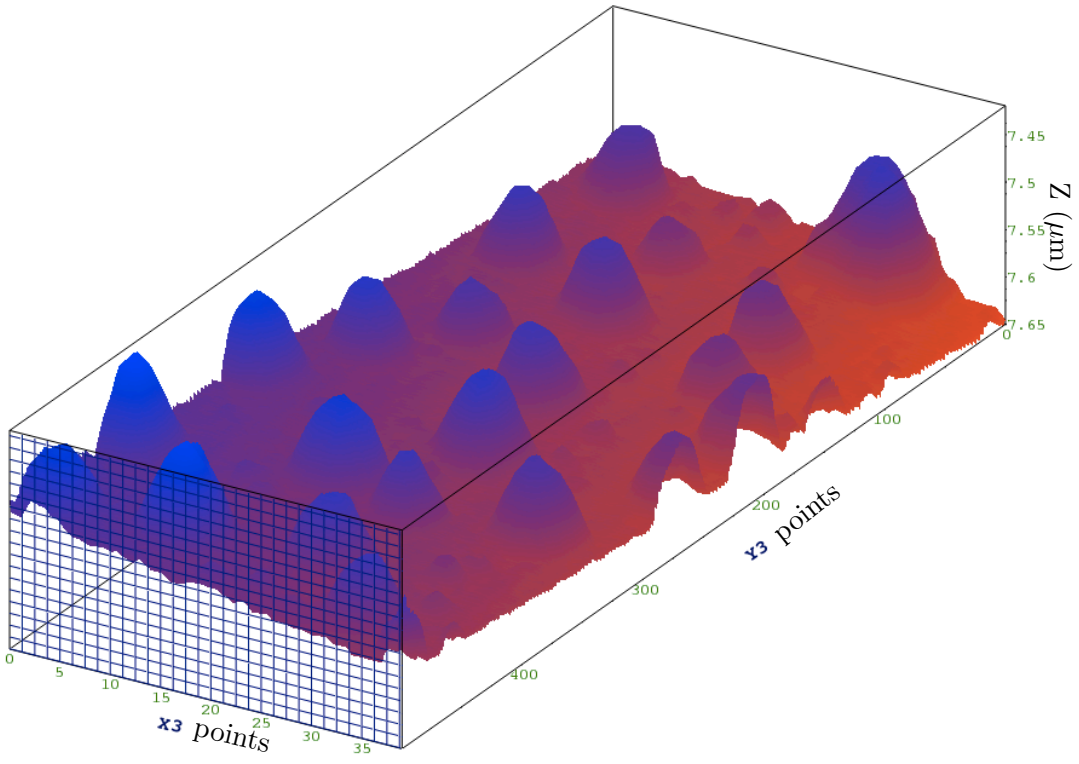

Figure 4.16 - *AFM image of Gold colloids of 80 nm diameter. The image size is 1 µm in X-axis and 2.5 µm in Y-axis. Image acquisition time is 72 seconds.*

of the quartz in addition to the slope of the tip. This image was repeated several times without modification of the positions of the nanospheres. For this experiment, fast imaging is not an objective. Image acquisition time was manually set a 72 seconds, mainly to avoid damage to the tip due the the contact imposed by shear mode.

A smaller image was done later on a single nano sphere of a diameter near 30 nm (Fig. 4.17). The diameter was estimated with the height of the sphere in the image. The diameter in the X-Y plane being theoretically the same, appears 2-3 times bigger in the image because the diameter of the Tip Is bigger by at lead 3 times the diameter of the nanosphere.

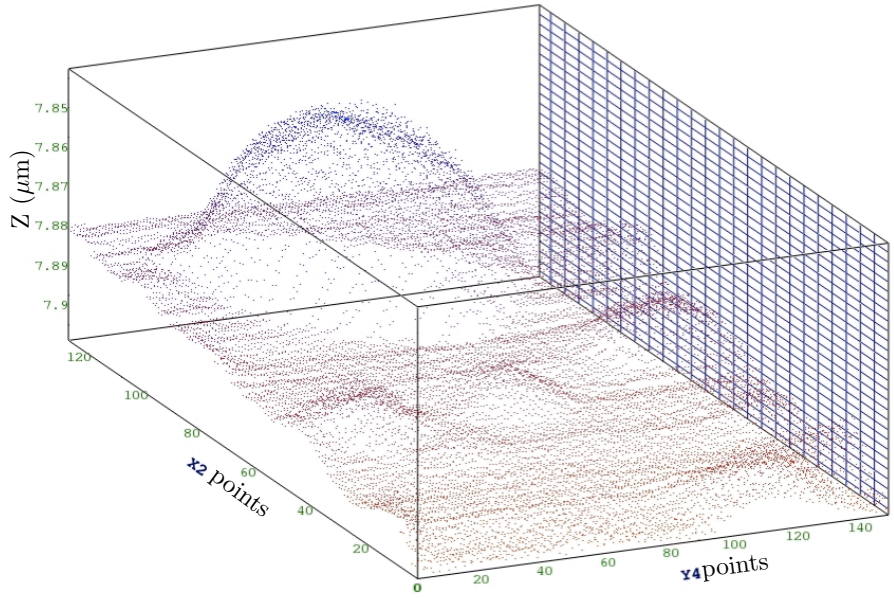

Figure 4.17 - *AFM Gold nanosphere image of 30 nm diameter. The image size is 240 nm in X-axis and 290 nm in Y-axis. Image acquisition time is 25 seconds.*

As a result of the tests from this and previous section, the new imaging arm of system is validated in term of speed for the electronics and data processing. Both normal and lateral modes have been experimentally validated. In the following, an application in nanomanipulation of the new version of the system is shown were on of the tip will be used for imaging and the other for manipulation.

4.2.3 Nanomanipulation

This is the manipulation task resulting from the new version of the system where one of the cantilevers has been replaced with a quartz oscillator. The task consist of 2D manipulation of gold colloids with the Tip I (Cantilever) and imaging with the Tip II (Quartz). In order to achieve this, a manipulation protocol is established for the cooperative manipulation task between the two tips of the new version of the system.

4.2.3.1 Manipulation protocol

1. The first thing to do is the initial approach of both tips to the substrate. For the Tip I, it is done with successive movement steps between the motorized micro stage and the closed loop nanostage in Z-axis till contact is in range of the nano stage. For the Tip II, the approach is done with the manual microstage and the open loop piezostage. Additionally, with the aid of the optical microscope the two tips are approached in X-Y plane till Tip I is within range of Tip II ($<$10 μm).

2. After the tips and substrate are within range of the piezo actuators, scans Y-axis are done with Tip II in order to find the Tip I.

3. Now that the position of the Tip I is known respect to the Tip II, an AFM image of substrate is done with Tip II. The Tip I end should appear in the image as well as the objects to manipulate, this way, the position of the object respect to the Tip I is known. The open loop piezo is used to maintain the distance between Tip I and the substrate fixed.

4. The next step is the 2D manipulation of nanoobjects on top of the substrate. The cantilever of Tip I is used in static mode. The force is monitored during the entire process to detect the contact between the Tip I and the object as well as the pushing. Closed loop nanostage is used to move the substrate.

5. Finally, the Tip II is used to rescan the surface to obtain an AFM image of the substrate with the new position of the objects.

In the following an application of this with the manipulation of gold colloid is presented.

4.2.3.2 Results

In this section, the result from a manipulation task of three gold colloids is presented following the protocol from previous section. After the two tips are within range according to the first step, the Tip I is found with the scanning Tip II as seen in Fig. 4.18. The triangular shape in the top of the scan in addition to the measured height allows the differentiation with a nanosphere. Afterwards, an AFM image is done with Tip II starting near Tip I and getting farther as shown in Fig. 4.20.(a). Once the position of the tip with respect the nanospheres is known, the nanospheres path planing is done. In this particular case, 3 nanospheres were pushed to form a big "V" shape in the substrate. The shape has been arbitrary chosen, the objective itself is to show the manipulation capabilities of the new system with two cooperative arms.

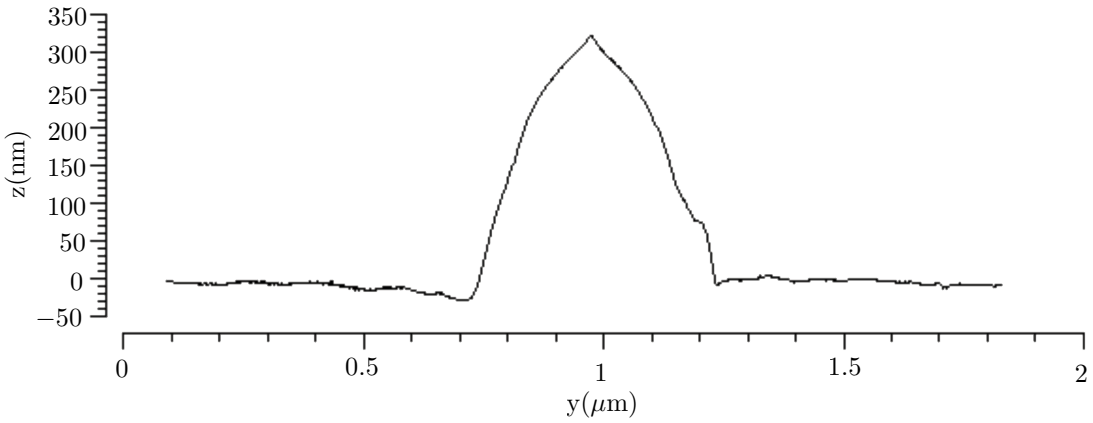

Figure 4.18 - *Scan in Y-axis with Tip II to find Tip I*

During the pushing of the nanospheres, the lateral and normal force are monitored, they were estimated with cantilever stiffness and the photodiode output. An example of the output of the photodiode for a diagonal pushing (Fig. 4.19.(e)) of gold colloid number 1 can be seen in Fig. 4.19. As a result of the diagonal pushing, forces in both X and Y-axis are felt. The pushing in X-axis makes the cantilever raise resulting in a positive voltage shift (Fig. 4.19.(b) and (d)). In Y-axis, the cantilever bends counter clock wise resulting in a negative voltage shift (Fig. 4.19.(a) and (d)). The behavior between the bending of the cantilever and the sign of the voltage shift is predefined with the geometrical configuration of the laser, cantilever

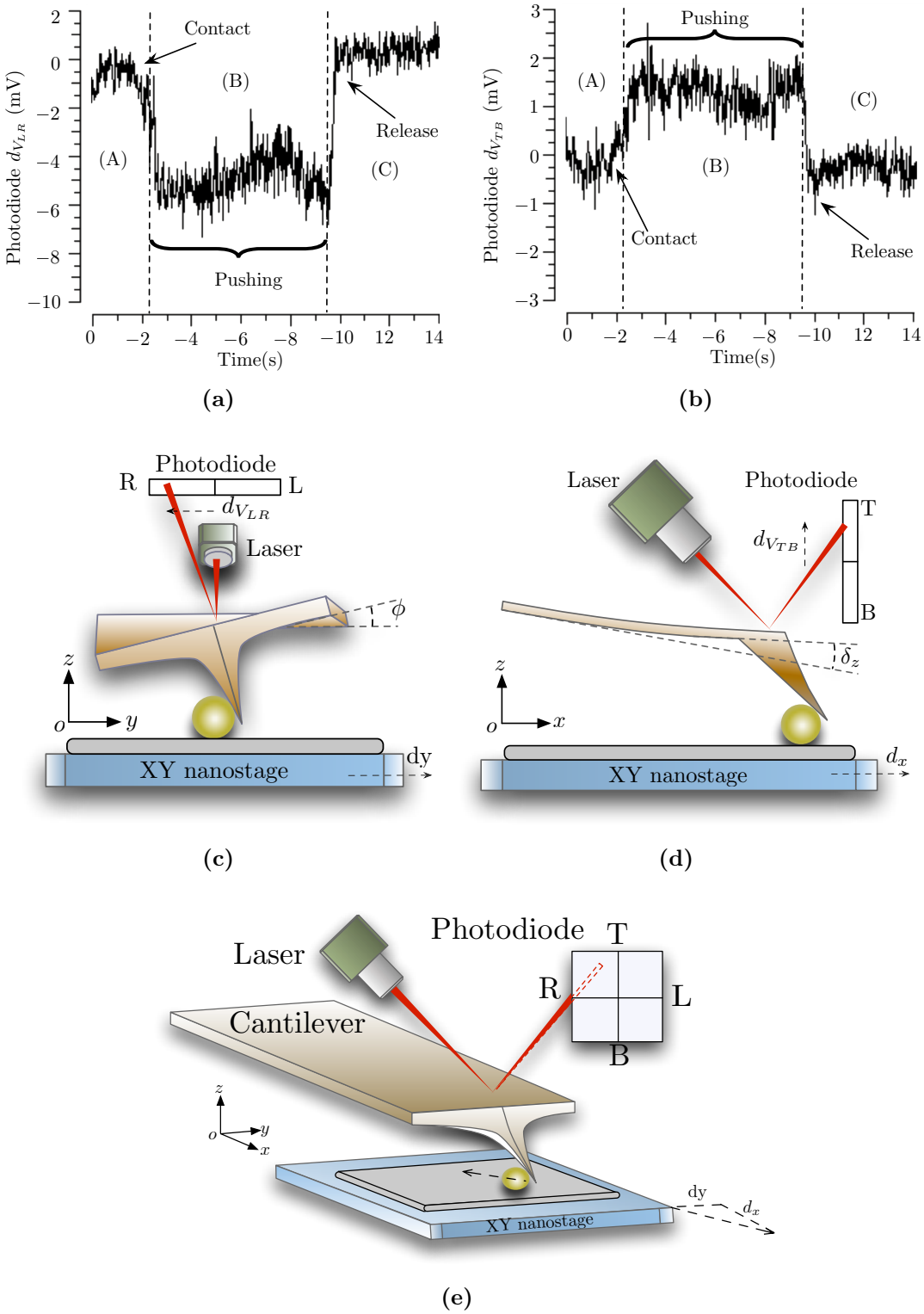

Figure 4.19 - *Diagonal pushing of nanosphere. (a) and (c) Left-Right photodiode voltage and diagram corresponding to cantilever lateral bending, (b) and (d) Top-bottom photodiode voltage and diagram corresponding to Z-axis bending. (e) Diagonal bending of the cantilever diagram.*

and photodiode.

The final manipulation result is depicted in Fig. 4.20.(b). The nanospheres 1, 2 and 3 with diameters of 120nm, 90nm and 150nm were successfully pushed with force feedback to the desired position. In this last image, the diameter of the colloids increased a little bit in X-Y-axis due to the wear of the tip, this is a consequence of the large diameter apex of the used tip combined with the shear mode. The image acquisition time for Fig. 4.20 was set at 108 seconds for the first image and 79 seconds for the second. Due to the slow response of the piezo combined with the big diameter of the nanospheres and the big apex of Tip I, they were set that high. High speed piezo control was not within the scope of this work. Those acquisition times are, however, at least four times smaller than previous system acquisition times. Additionally, they were done in shear mode. Doing them in normal mode will make those time decrease due to the range of the control zone as weal as the fact that is non-contact.

4.3 Conclusions

In this final chapter of the manuscript, a new version of the two tip AFM has been presented. One of the cantilevers has been replaced with a novel high speed dynamic force sensor. The AFM controller has been made from scratch on a real time operating system. Additionally all the electronics have been redesigned in order to support the high frequencies used by the quartz. The high speed of the system imaging has been proved. Compared to previous version of the system, it is at least 50 times faster for imaging. At the moment, the sensor is on experimental stage, and, so, it is challenging to predict the operation mode from tip attachment, still, independent of the mode, they were used successfully. The functioning of the new system in cooperation with a cantilever has been proved by pushing of gold colloid. Future works with this system include further modeling of the new sensor in order to do quantitative force measurement. High speed piezo control is also in the scope to reveal the true potential of the new system.

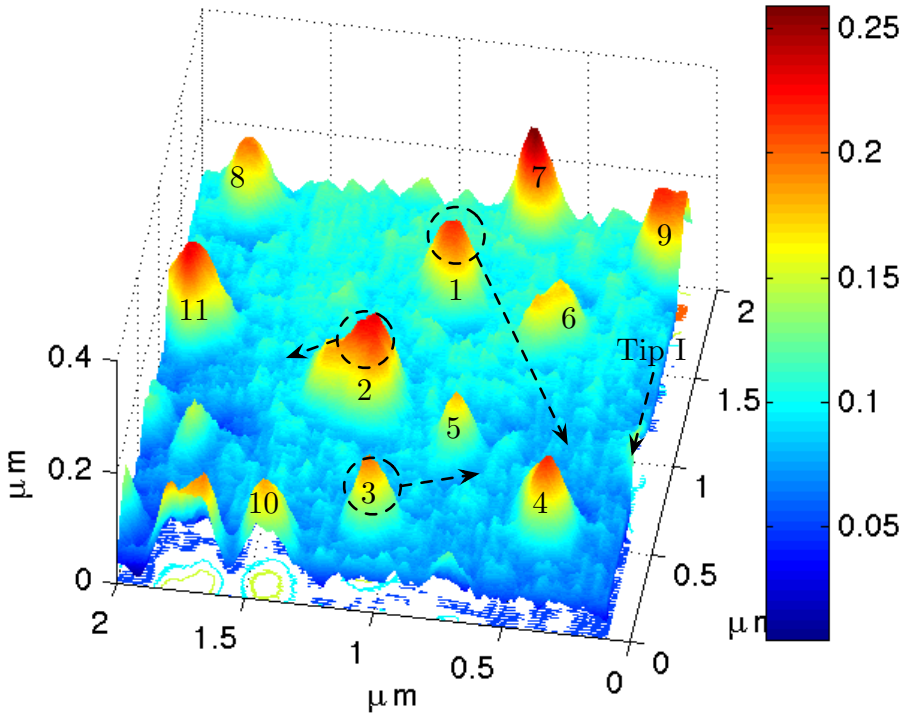

(a)

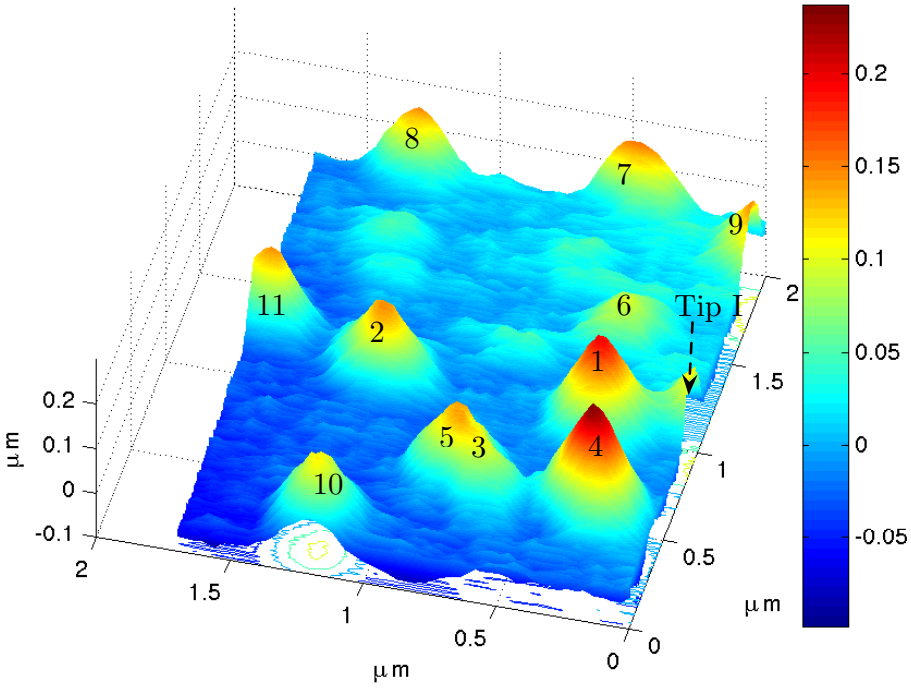

(b)

Figure 4.20 - *Manipulation results (a)Image with Tip II before manipulation, (b) Image with Tip II after manipulation. Image acquisition time for first image is 108 seconds. and 79 seconds for the second.*

Conclusion and perspectives

The difficulty of the manipulation in an interactive and repeatable way of nanoobjects is a scientific fundamental problem. It is a mayor barrier for applications on emerging devices like nanotransistors, the nanosystems or future nems, slowing in their experimental development. Toward solving those issues, the force feedback micro and nanomanipulation based on atomic force microscopy appears as a promising technique. Those systems however, are mainly limited to two diminutional manipulation, and do not have the speed required for automation. In order to improve the manipulation capabilities, several subjects have been treated in this thesis.

- 3D Micronamipulation in the air of objects of a few micrometers has been achieved by using a gripper built with two nano tips. The gripper has been made with two atomic force microscope cantilevers with protrudent tips independently actuated. A manipulation protocol allowed pick-and-place of microspheres with diameter of 3 μm $\sim$ 4 μm to a desired position. For the initial step of grasping, the cantilevers were working in tapping mode and the amplitude feedback was used to estimate the contact/grasping point on the spheres. Then pick, and place has been achieved with the cantilevers in static mode by monitoring in real time the force readout. At nano metric scale, classic AFM applications allow to manipulate nano particles, nano wires or nanotubes by pushing or pulling in the X-Y plane. Still, pick and place has been a challenge in the air. The proposed system presented for force feedback 3D micro manipulation has been modified to respond to this problem. The

size of visible objects being limited by the light wave length in addition to quality of the lens, makes the use optical microscope impossible for the visual feedback of the process. In consequence, one of the AFM tips has to be used for surface imaging and detection of the position of the other tip. With this method, SiNW manipulation has been exploited to form nanocrosses. With this system, the micro/nanomanipulation or micro/nanoassembly has become possible in 3D with force feedback in the air.

- Still, the system had two mayor problems. The first being the scanning speed and the second, the dexterity of the arm. To address these issues a study of dynamic force sensor has been made. For that, a robotic system inside the SEM has been developed using tuning forks as sensors for dynamics force feedback. The wide range capabilities has been proven by the mechanical characterization of HNBs. The non-linear stiffness behavior of the nano belts has been revealed for the first time. Additionally, the surface of membranes for optical mirror applications have been characterized in stiffness with a moving, sensor.

- Finally, the dynamic force sensing techniques have been used for parallel imaging and manipulation. One of the cantilevers of the AFM has been replaced with a dynamic force sensor. For this, a new type of dynamic force sensor has been introduced with resonant frequencies in the megahertz range. The represents a challenge because the wave mode is not known with precession. Even so, true non-contact mode imaging as well as shear/lateral mode imaging have been achieved. Profound changes in the system had to be done in order to support the speed associated with the new sensor. The system capabilities have been proven by a parallel imaging and manipulation task. Even if the system is limited by the response of the piezo actuators, the speed of the manipulation process has increased by at least five times. Individual images independent of Z-control show that the system can be even fifty times faster than previous system. Additionally, the displacement range of the arm has been increased without the need of recalibration. Furthermore, the true non-contact mode allows a non-invasive imaging of the substrate.

This work is the first step towards real time parallel imaging and manipulation. Several works are in the scope. Particularly, high speed imaging can attenuate undesired effects like thermal noise, increasing the repeatability of the manipulations.

The next step toward a faster imaging platform is the high speed control of the piezo actuators, specially in Z-axis for high speed control of the interaction between

the tip and the sample. This is a mayor step involving mechanical redesign for stable high speed motion of the piezo. Still, for the rest of the system it should be a straightforward transition with few modifications.

The same high speed sensor could also be used inside an SEM for dynamic mechanical characterization of flexible micro/nanostructures. As an example, the resonant mode of the membranes shown in chapter 3 could be obtained. For this, the structure should be placed under an SEM compatible closed loop piezoscanner. The will remove the dependency from SEM visual feedback for position estimation and allow faster control. The transition from tuning forks to the high speed quartz oscillators shown in chapter 4 should be straightforward as the amplifier is compatible with the high voltage of the electron beam of the SEM.

To go even further, a three tip AFM can be in the scope. Two of the three tips of the system can be used for 3D manipulation and the last one can exploit the non-invasive dynamic force feedback from a quartz oscillator to establish a real time mapping of the scene. Force spectroscopy coupled with position feedback can be an original solution for high resolution 3D manipulation of micro/nanoobjects.

Lastly, at long term, a multiprobe AFM based system for fully automated nanoassembly could be achieved. In order to do this, ideally, all the manual steps of the manipulation protocol should be removed. First, the initial approach of the tips should be fully automated by visual detection of the coarse position of the tips with an optical microscope combined with the force feedback monitoring for contact detection. Adding a new piezo actuator with longer range, and replacing the manual micro stages by motorized/piezo micro stages needs to be done. Estimation of objects position trough visual recognition from AFM images will be key for a manipulation loop without human intervention. The dynamic force sensing with the novel quartz sensor should provide the dynamic feedback required to close the loop of the real time manipulation task to fully automate the system. A fully automated multiprobe AFM system based on high speed dynamic force sensing becomes the key toward a the three diminutional high speed nanoassembly breakthrough.

Publications list

Acosta, J.C. et Hwang, G. et Polesel-Maris, J. et Régnier, S *A tuning fork based wide range mechanical characterization tool with nanorobotic manipulators inside a scanning electron microscope.*
Review of Scientific Instruments. Vol 82 No 3 2011.

Hwang, G. and Acosta, J.C. and Hashimoto, H. and Régnier, S
In situ Characterizations of Thin-film Nanostructures with Large Range Direct Force Sensing.
Signal Measurement and Estimation Techniques : Micro and Nanotechnology, Springer, publisher (2011)

Hwang, G. and Haliyo, S. and Acosta, J.C. and Régnier, S
Method For Generating A Potential Difference With The Aid Of A Thin Graphene Film, And Devices Using The Same.
WIPO Patent Application WO/2011/032726.

Acosta, J.C. and Hwang, G. and Thoyer, F. and Polesel-Maris, J. and Régnier, S
Tuning Fork based in situ SEM nanorobotic manipulation system for Wide Range mechanical characterization of ultra flexible nanostructures.
2010 IEEE/RSJ International Conference on Intelligent Robots and Systems. (IROS 2010)

Hwang, G. and Acosta, J.C. and Vela Saavedra, E. and Haliyo, S. and Régnier, S.
Graphene as Thin Film Infrared Optoelectronic Sensor..
IEEE ISOT 2009 International Symposium on Optomechatronic Technologies .

Xie, H. and Acosta, J.C. and Haliyo, S. and Régnier, S.
Pick-and-Place Nanomanipulation with Three-Dimensional Manipulation Force Microscopy.
The 2009 IEEE/RSJ International Conference on Intelligent Robots and Systems. (IROS 2009) **Best Application Paper Award.**

Xie, H. and Acosta, J.C. and Régnier, S.
Achieving Three-Dimensional Automated Micromanipulation at the Scale of Several Micrometers with a Nanotip Gripper.
The 2009 IEEE/RSJ International Conference on Intelligent Robots and Systems. (IROS 2009)

Bibliography

[AGHR91] T. R. Albrecht, P. Grutter, D. Horne, and D. Rugar. Frequency modulation detection using high-Q cantilevers for enhanced force microscope sensitivity. *Journal of Applied Physics*, 69(2):668–673, January 1991.

[AL07] Peter M Albrecht and Joseph W Lyding. Lateral manipulation of single-walled carbon nanotubes on h-passivated si(100) surfaces with an ultrahigh-vacuum scanning tunneling microscope. *Small Weinheim an der Bergstrasse Germany*, 3(1):146–152, 2007.

[AUF08] Toshio Ando, Takayuki Uchihashi, and Takeshi Fukuma. High-speed atomic force microscopy for nano-visualization of dynamic biomolecular processes. *Progress in Surface Science*, 83(7-9):337–437, November 2008.

[Avo95] Phaedon Avouris. Manipulation of matter at the atomic and molecular levels. *Accounts of Chemical Research*, 28(3):95–102, March 1995.

[BABO08] Lana Bosanac, Thomas Aabo, Poul M. Bendix, and Lene B. Oddershede. Efficient optical trapping and visualization of silver nanoparticles. *Nano Letters*, 8(5):1486–1491, May 2008.

[BAW10] K. A. Brown, J. A. Aguilar, and R. M. Westervelt. Coaxial atomic force microscope tweezers. *Applied Physics Letters*, 96(12):123109, 2010.

[BBK+98] C. Baur, A. Bugacov, Bruce E. Koel, A. Madhukar, N. Montoya, T. R. Ramachandran, A. A. G. Requicha, R. Resch, and P. Will. Nanoparticle manipulation by mechanical pushing: underlying phenomena and real-time monitoring. *Nanotechnology*, (4):360–364, 1998.

[BDN+06] Dominik J. Bell, Lixin Dong, Bradley J. Nelson, Matthias Golling, Li Zhang, and Detlev Grützmacher. Fabrication and characterization of Three-Dimensional InGaAs/GaAs nanosprings. *Nano Letters*, 6(4):725–729, April 2006.

[BMN09] Felix Beyeler, Simon Muntwyler, and Bradley J. Nelson. A Six-Axis MEMS Force-Torque sensor with Micro-Newton and Nano-Newtonmeter resolution. *Journal of Microelectromechanical Systems*, 18(2):433–441, April 2009.

[BQG86] G. Binnig, C. F. Quate, and Ch. Gerber. Atomic force microscope. *Physical Review Letters*, 56(9):930, March 1986.

[BRC+07] Michael Bordag, Aline Ribayrol, Gabriela Conache, Linus E Fröberg, Struan Gray, Lars Samuelson, Lars Montelius, and Hakan Pettersson. Shear stress measurements on InAs nanowires by AFM manipulation. *Small*, 3(8):1398–1401, August 2007.

[BSZ+06] D.J. Bell, Y. Sun, L. Zhang, L.X. Dong, B.J. Nelson, and D. Grützmacher. Three-dimensional nanosprings for electromechanical sensors. *Sensors and Actuators A: Physical*, 130-131:54–61, August 2006.

[CAR09] A Castellanos-Gomez, N Agraït, and G Rubio-Bollinger. Dynamics of quartz tuning fork force sensors used in scanning probe microscopy. *Nanotechnology*, 20(21):215502, May 2009.

[CGR+08] Gabriela Conache, Struan M. Gray, Aline Ribayrol, Linus E. Fröberg, Lars Samuelson, Hakan Pettersson, and Lars Montelius. Friction measurements of InAs nanowires on silicon nitride by AFM manipulation. *Small*, 5(2):203–207, December 2008.

[CL01] Yi Cui and Charles M. Lieber. Functional nanoscale electronic devices assembled using silicon nanowire building blocks. *Science*, 291(5505):851–853, February 2001.

[DAF02] Lixin Dong, Fumihito Arai, and Toshio Fukuda. Electron-beam-induced deposition with carbon nanotube emitters. *Applied Physics Letters*, 81(10):1919, 2002.

[DAF04] Lixin Dong, F. Arai, and T. Fukuda. Destructive constructions of nanostructures with carbon nanotubes through nanorobotic manipulation. *Mechatronics, IEEE/ASME Transactions on*, 9(2):350–357, 2004.

[DHR+96] Hongjie Dai, Jason H. Hafner, Andrew G. Rinzler, Daniel T. Colbert, and Richard E. Smalley. Nanotubes as nanoprobes in scanning probe microscopy. *Nature*, 384(6605):147–150, November 1996.

[DMJ+07] Dirk Dietzel, Tristan Mönninghoff, Lars Jansen, Harald Fuchs, Claudia Ritter, Udo D. Schwarz, and André Schirmeisen. Interfacial friction obtained by lateral manipulation of nanoparticles using atomic force microscopy techniques. *Journal of Applied Physics*, 102(8):084306, 2007.

[DVRB05] W Driesen, T Varidel, S Régnier, and J-M Breguet. Micro manipulation by adhesion with two collaborating mobile micro robots. *Journal of Micromechanics and Microengineering*, 15(10):S259–S267, October 2005.

[ES90] D. M. Eigler and E. K. Schweizer. Positioning single atoms with a scanning tunnelling microscope. *Nature*, 344(6266):524–526, April 1990.

[FAD03] T. Fukuda, F. Arai, and L. Dong. Assembly of nanodevices with carbon nanotubes through nanorobotic manipulations. *Proceedings of the IEEE*, 91(11):1803–1818, 2003.

[FTIH+99] M. R. Falvo, R. M. Taylor II, A. Helser, V. Chi, F. P. Brooks Jr, S. Washburn, and R. Superfine. Nanometre-scale rolling and sliding of carbon nanotubes. *Nature*, 397(6716):236–238, January 1999.

[GDM+05] Pu Xian Gao, Yong Ding, Wenjie Mai, William L. Hughes, Changshi Lao, and Zhong Lin Wang. Conversion of zinc oxide nanobelts into Superlattice-Structured nanohelices. *Science*, 309(5741):1700–1704, September 2005.

[Gie] Franz J. Giessibl. High-speed force sensor for force microscopy and profilometry utilizing a quartz tuning fork. *Applied Physics Letters*, 73(26):3956–3958.

[Gie97] Franz J. Giessibl. Forces and frequency shifts in atomic-resolution dynamic-force microscopy. *Physical Review B*, 56(24):16010, December 1997.

[Gie00] Franz J. Giessibl. Atomic resolution on si(111)-(7 x 7) by noncontact atomic force microscopy with a force sensor based on a quartz tuning fork. *Applied Physics Letters*, 76(11):1470–1472, March 2000.

[Gie03] Franz J. Giessibl. Advances in atomic force microscopy. *Reviews of Modern Physics*, 75(3):949, July 2003.

[GP02] Ricardo García and Rubén Pérez. Dynamic atomic force microscopy methods. *Surface Science Reports*, 47(6-8):197–301, September 2002.

[GRM+06] Leonhard Grill, Karl-Heinz Rieder, Francesca Moresco, Sladjana Stojkovic, André Gourdon, and Christian Joachim. Exploring the interatomic forces between tip and single molecules during STM manipulation. *Nano Letters*, 6(12):2685–2689, December 2006.

[HCOL01] Jason H. Hafner, Chin-Li Cheung, Tjerk H. Oosterkamp, and Charles M. Lieber. High-Yield assembly of individual Single-Walled carbon nanotube tips for scanning probe microscopies. *The Journal of Physical Chemistry B*, 105(4):743–746, February 2001.

[HH09] Gilgueng Hwang and Hideki Hashimoto. Piezoresistive InGaAs/GaAs nanosprings with metal connectors. *Nano Letters*, 9(2):554–561, February 2009.

[HMH05] A. D. L. Humphris, M. J. Miles, and J. K. Hobbs. A mechanical microscope: High-speed atomic force microscopy. *Applied Physics Letters*, 86(3):034106, 2005.

[HR08] Shuiqing Hu and Arvind Raman. Inverting amplitude and phase to reconstruct tip–sample interaction forces in tapping mode atomic force microscopy. *Nanotechnology*, 19(37), September 2008.

[Iij91] Sumio Iijima. Helical microtubules of graphitic carbon. *Nature*, 354(6348):56–58, November 1991.

[JAH04] Hee-Won Jeong, Tetsuya Aoki, and Takeshi Hatsuzawa. Frequency responses of spherically contoured rectangular at-cut quartz crystal resonators fabricated by fixed abrasive method. *International Journal of Machine Tools and Manufacture*, 44(11):1143 – 1149, 2004.

[JYSAK+07] Yong Ju Yun, Chil Seong Ah, Sanghun Kim, Wan Soo Yun, Byong Chon Park, and Dong Han Ha. Manipulation of freestanding au nanogears using an atomic force microscope. *Nanotechnology*, 18(50):505304, December 2007.

[Jé] Polesel Jérôme. Electronic control and amplification device for a piezoelectric local probe for measuring force beneath a particle beam, patents wo2011092225, fr2955938.

[KDZN10] B.E. Kratochvil, L.X. Dong, L. Zhang, and B.J. Nelson. Image-based 3D reconstruction using helical nanobelts for localized rotations. *Journal of Microscopy*, 237(2):122–135, 2010.

[KG95] Khaled Karrai and Robert D. Grober. Piezoelectric tip-sample distance control for near field optical microscopes. *Applied Physics Letters*, 66(14):1842–1844, April 1995.

[Kin] Kinovea. Video analysis software for sports. http://www.kinovea.org/en/.

[KK01] P. Krejci and K. Kuhnen. Inverse control of systems with hysteresis and creep. *Control Theory and Applications, IEE Proceedings -*, 148(3):185–192, 2001.

[KL99] Philip Kim and Charles M. Lieber. Nanotube nanotweezers. *Science*, 286(5447):2148–2150, December 1999.

[KOSF09] Florian Krohs, Cagdas Onal, Metin Sitti, and Sergej Fatikow. Towards automated nanoassembly with the atomic force microscope: A versatile drift compensation procedure. *Journal of Dynamic Systems, Measurement, and Control*, 131(6):061106–8, November 2009.

[KvEO09] Allard J Katan, Maarten H van Es, and Tjerk H Oosterkamp. Quantitative force versus distance measurements in amplitude modulation AFM: a novel force inversion technique. *Nanotechnology*, 20(16), April 2009.

[KW03] Xiang Yang Kong and Zhong Lin Wang. Spontaneous Polarization-Induced nanohelixes, nanosprings, and nanorings of piezoelectric nanobelts. *Nano Letters*, 3(12):1625–1631, December 2003.

[LCD99] Jun Li, Alan M. Cassell, and Hongjie Dai. Carbon nanotubes as AFM tips: measuring DNA molecules at the liquid/solid interface. *Surface and Interface Analysis*, 28(1):8–11, 1999.

[LDK+07] Kyumin Lee, M. Duchamp, G. Kulik, A. Magrez, Jin Won Seo, S. Jeney, A. J. Kulik, L. Forró, R. S. Sundaram, and J. Brugger. Uniformly dispersed deposition of colloidal nanoparticles and nanowires by boiling. *Applied Physics Letters*, 91:173112, 2007.

[LGMC03] Xiaodong Li, Hongsheng Gao, Catherine J. Murphy, and K. K. Caswell. Nanoindentation of silver nanowires. *Nano Letters*, 3(11):1495–1498, November 2003.

[LR06] Pierre Lambert and Stéphane Régnier. Surface and contact forces models within the framework of microassembly. *Journal of Micromechatronics*, 3:123–157, June 2006.

[LWS07] X Y Liu, W H Wang, and Y Sun. Dynamic evaluation of autofocusing for automated microscopic analysis of blood smear and pap smear. *Journal of Microscopy*, 227(Pt 1):15–23, July 2007. PMID: 17635655.

[MA88] Gerhard Meyer and Nabil M. Amer. Novel optical approach to atomic force microscopy. *Applied Physics Letters*, 53(12):1045, 1988.

[MBE99] Daniel J. Müller, Wolfgang Baumeister, and Andreas Engel. Controlled unzipping of a bacterial surface layer with atomic force microscopy. *Proceedings of the National Academy of Sciences of the United States of America*, 96(23):13170–13174, November 1999.

[MEID04] A. Menciassi, A. Eisinberg, I. Izzo, and P. Dario. From "macro" to "micro" manipulation: models and experiments. *Mechatronics, IEEE/ASME Transactions on*, 9(2):311–320, 2004.

[MGR+08] K. Mougin, E. Gnecco, A. Rao, M. T. Cuberes, S. Jayaraman, E. W. McFarland, H. Haidara, and E. Meyer. Manipulation of gold nanoparticles: Influence of surface chemistry, temperature, and environment (Vacuum versus ambient atmosphere)†. *Langmuir*, 24(4):1577–1581, February 2008.

[MKNI90] Seiji Motojima, Masayuki Kawaguchi, Koji Nozaki, and Hiroshi Iwanaga. Growth of regularly coiled carbon filaments by ni catalyzed pyrolysis of acetylene, and their morphology and extension characteristics. *Applied Physics Letters*, 56(4):321, 1990.

[MRH+98] M. Martin, L. Roschier, P. Hakonen, U. Parts, M. Paalanen, B. Schleicher, and E. I Kauppinen. Manipulation of ag nanoparticles utilizing noncontact atomic force microscopy. *Applied Physics Letters*, 73(11):1505–1507, September 1998.

[MWF10] U. Mick, M. Weigel-Jech, and S. Fatikow. Robotic workstation for AFM-based nanomanipulation inside an SEM. In *2010 IEEE/ASME International Conference on Advanced Intelligent Mechatronics (AIM)*, pages 854–859. IEEE, July 2010.

[MWKB06] Kristian Mølhave, Thomas Wich, Axel Kortschack, and Peter Bøggild. Pick-and-place nanomanipulation using microfabricated grippers. *Nanotechnology*, 17(10):2434–2441, May 2006.

[NL06] Hai Ni and Xiaodong Li. Young's modulus of ZnO nanobelts measured using atomic force microscopy and nanoindentation techniques. *Nanotechnology*, 17(14):3591–3597, July 2006.

[OS07] C.D. Onal and M. Sitti. Visual Servoing-Based autonomous 2-D manipulation of microparticles using a nanoprobe. *Control Systems Technology, IEEE Transactions on*, 15(5):842–852, 2007.

[PB08] Manuel Palacio and Bharat Bhushan. A nanoscale friction investigation during the manipulation of nanoparticles in controlled environments. *Nanotechnology*, 19(31):315710, August 2008.

[PBU+07] L M Picco, L Bozec, A Ulcinas, D J Engledew, M Antognozzi, M A Horton, and M J Miles. Breaking the speed limit with atomic force microscopy. *Nanotechnology*, 18(4):044030, January 2007.

[PGP07] Sung-Jin Park, Miriam B. Goodman, and Beth L. Pruitt. Analysis of nematode mechanics by piezoresistive displacement clamp. *Proceedings of the National Academy of Sciences*, 104(44):17376–17381, October 2007.

[Req03] A. A.G Requicha. Nanorobots, NEMS, and nanoassembly. *Proceedings of the IEEE*, 91(11):1922– 1933, November 2003.

[RLM+00] Resch, Lewis, Meltzer, Montoya, Koel, Madhukar, Requicha, and Will. Manipulation of gold nanoparticles in liquid environments using scanning force microscopy. *Ultramicroscopy*, 82(1-4):135–139, February 2000. PMID: 10741662.

[RRG99] Yves Rollot, Stéphane Régnier, and Jean-Claude Guinot. Simulation of micro-manipulations: Adhesion forces and specific dynamic models. *International Journal of Adhesion and Adhesives*, 19(1):35–48, February 1999.

[SH00] M. Sitti and H. Hashimoto. Controlled pushing of nanoparticles: modeling and experiments. *Mechatronics, IEEE/ASME Transactions on*, 5(2):199–211, 2000.

[SHA+00] T. Sulchek, R. Hsieh, J. D. Adams, G. G. Yaralioglu, S. C. Minne, C. F. Quate, J. P. Cleveland, A. Atalar, and D. M. Adderton. High-

speed tapping mode imaging with active q control for atomic force microscopy. *Applied Physics Letters*, 76(11):1473, 2000.

[Sit04] M. Sitti. Atomic force microscope probe based controlled pushing for nanotribological characterization. *Mechatronics, IEEE/ASME Transactions on*, 9(2):343–349, 2004.

[Sit07] M. Sitti. Microscale and nanoscale robotics systems [Grand challenges of robotics]. *Robotics & Automation Magazine, IEEE*, 14(1):53–60, 2007.

[SJ04] John E. Sader and Suzanne P. Jarvis. Accurate formulas for interaction force and energy in frequency modulation force spectroscopy. *Applied Physics Letters*, 84(10):1801–1803, March 2004.

[SJ08] Reza Saeidpourazar and Nader Jalili. Microcantilever-Based force tracking with applications to High-Resolution imaging and nanomanipulation. *IEEE Transactions on Industrial Electronics*, 55(11):3935–3943, November 2008.

[SN04] Y. U. Sun and B. J Nelson. MEMS for cellular force measurements and molecular detection. *Journal of Information Acquisition*, 1(1):23–32, 2004.

[SSRN09] Richard Smith, Douglas Sparks, Diane Riley, and Nader Najafi. A MEMS-Based coriolis mass flow sensor for industrial applications. *IEEE Transactions on Industrial Electronics*, 56(4), April 2009.

[TBCD07] E. Tranvouez, E. Boer-Duchemin, G. Comtet, and G. Dujardin. Active drift compensation applied to nanorod manipulation with an atomic force microscope. *Review of Scientific Instruments*, 78(11):115103–5, November 2007.

[TG10] J. Toset and G. Gomila. Three-dimensional manipulation of gold nanoparticles with electro-enhanced capillary forces. *Applied Physics Letters*, 96(4):043117, 2010.

[TS98] M. Todorovic and S. Schultz. Magnetic force microscopy using nonoptical piezoelectric quartz tuning fork detection design with applications to magnetic recording studies. *Journal of Applied Physics*, 83(11):6229, 1998.

[VEH03] M. Varenberg, I. Etsion, and G. Halperin. An improved wedge calibration method for lateral force in atomic force microscopy. *Review of Scientific Instruments*, 74(7):3362, 2003.

[VS06] Viola Vogel and Michael Sheetz. Local force and geometry sensing regulate cell functions. *Nat Rev Mol Cell Biol*, 7(4):265–275, April 2006.

[WHB05] Bin Wu, Andreas Heidelberg, and John J. Boland. Mechanical properties of ultrahigh-strength gold nanowires. *Nat Mater*, 4(7):525–529, July 2005.

[WMT+06] Jed D. Whittaker, Ethan D. Minot, David M. Tanenbaum, Paul L. McEuen, and Robert C. Davis. Measurement of the adhesion force between carbon nanotubes and a silicon dioxide substrate. *Nano Letters*, 6(5):953–957, May 2006.

[WSDC91] L. J. WHITMAN, JOSEPH A. STROSCIO, R. A. DRAGOSET, and R. J. CELOTTA. Manipulation of adsorbed atoms and creation of new structures on Room-Temperature surfaces with a scanning tunneling microscope. *Science*, 251(4998):1206–1210, March 1991.

[XHR09] H. Xie, D. S. Haliyo, and S. Régnier. Parallel imaging/manipulation force microscopy. *Applied Physics Letters*, 94:153106, 2009.

[XRS07] Hui Xie, Weibin Rong, and Lining Sun. Construction and evaluation of a wavelet-based focus measure for microscopy imaging. *Microscopy Research and Technique*, 70(11):987–995, November 2007. PMID: 17661388.

[XRSC06] Hui Xie, Weibin Rong, Lining Sun, and Wei Chen. Image fusion and 3-D surface reconstruction of microparts using complex valued wavelet transforms. In *Image Processing, 2006 IEEE International Conference on*, pages 2137–2140, 2006.

[XT03] Bingqian Xu and Nongjian J. Tao. Measurement of Single-Molecule resistance by repeated formation of molecular junctions. *Science*, 301(5637):1221 –1223, 2003.

[YCS04] Ting Yu, Fook-Chiong Cheong, and Chorng-Haur Sow. The manipulation and assembly of CuO nanorods with line optical tweezers. *Nanotechnology*, 15(12):1732–1736, December 2004.

[ZZB+94] X. B. Zhang, X. F. Zhang, D. Bernaerts, G. van Tendeloo, S. Amelinckx, J. van Landuyt, V. Ivanov, J. B. Nagy, Ph Lambin, and A. A. Lucas. The texture of catalytically grown Coil-Shaped carbon nanotubules. *EPL (Europhysics Letters)*, 27(2):141–146, 1994.

Appendix A

Nanostructure stiffness and force error estimation

The nanostructure stiffness and force error are obtained with error propagation method in Eq. 1.14 and Hooke's law.

$$\begin{aligned} & eK_{spring} \\ &= \left|\frac{\delta K_{spring}}{\delta K_{TF}}\right| \cdot eK_{TF} + \left|\frac{\delta K_{spring}}{\delta \Delta f}\right| \cdot e\Delta f + \left|\frac{\delta K_{spring}}{\delta f_0}\right| \cdot ef_0 \\ &= \frac{2}{f_0} \cdot \left(\Delta f \cdot eK_{TF} + K_{TF} \cdot e\Delta f + \frac{K_{TF} \cdot \Delta f \cdot ef_0}{f_0}\right) \end{aligned} \tag{A.1}$$

$$\begin{aligned} eF &= \left|\frac{\delta F}{\delta K_{spring}}\right| \cdot eK_{spring} + \left|\frac{\delta F}{\delta x}\right| \cdot ex \\ &= x \cdot eK_{spring} + K_{spring} \cdot ex \end{aligned} \tag{A.2}$$

where eK_{TF}, $e\Delta f$ and ef_0 are the estimation error of the tuning fork stiffness, the frequency shift and the resonant frequency. ex is the spring elongation estimation error with SEM visual feedback.